EFFECT OF DIRECT HOT PRESS FORMING ON THE ELECTROCHEMICAL PROPERTIES OF NEXT GENERATION ZN-COATED PRESS HARDENABLE STEELS

THE EFFECT OF DIRECT HOT PRESS FORMING ON THE ELECTROCHEMICAL

PROPERTIES OF NEXT GENERATION ZN-COATED PRESS HARDENABLE

STEELS

By

JAIME DORA LYN JEWER, B.Eng.Scty

A Thesis

Submitted to the School of Graduate Studies

In Partial Fulfilment of the Requirements

For the Degree

Master of Applied Science

McMaster University

McMaster University   Master of Applied Science (2021)

Hamilton, Ontario   (Materials Science and Engineering)

TITLE: The Effect of Direct Hot Press Forming on the

                            Electrochemical Properties of Next Generation Zn-Coated

                            Press Hardenable Steels

AUTHOR: Jaime Dora Lyn Jewer, B.Eng.Scty. (McMaster University)

SUPERVISOR: Dr. Joseph R. McDermid and Dr. Joseph R. Kish

NUMBER OF PAGES: xviii, 107

ABSTRACT

In recent years, the automotive industry has turned to press hardened steels (PHS) to improve passenger safety while enabling vehicle weight reduction. To form the complex shapes required for this purpose, they are often direct hot press formed. It is possible to provide corrosion resistance to these parts by galvanizing the PHS sheets prior to direct hot press forming (DHPF). However, the austenization of the galvanized steel causes the Zn-based coating to transform into two intermetallic phases. These are iron rich α-Fe(Zn) and zinc rich Γ-Fe$_3$Zn$_{10}$. The Γ-Fe$_3$Zn$_{10}$ is liquid during traditional DHPF, and the applied stress can result in liquid metal embrittlement (LME). Recently, two new grades of PHS have been developed, which allow for DHPF at 600-700°C, below the Fe-Zn peritectic temperature at 782°C, thus avoiding LME. These prototype PHS grades are designated 2%Mn (0.2C-2Mn-0.25Si-0.005B (wt%)) and 2.5%Mn (0.2C-2.5Mn-0.25Si-0.005B (wt%)). The objective of this work is to determine the effect of DHPF on the ability of a Zn-based coating to provide robust cathodic protection to the two prototype PHS.

Galvanized panels of both the 2%Mn and 2.5%Mn steel were DHPF with a U-shape die at 700°C. The surface and cross-section of the coating were examined to determine the effects of DHPF on the coating surface. Die friction during DHPF resulted in die wiping on the wall of the part, leading to removal of surface Γ-Fe$_3$Zn$_{10}$. In cross-section, coating cracks were present at the wall and corner of the U-shape part due to the deformation during DHPF. Potentiodynamic polarization scans were used to determine the corrosion potential of the coating, and this was used to calculate the driving force for

cathodic protection using the difference in corrosion potential between the coating phases and the substrate. It was found that only Γ-Fe_3Zn_{10} provided robust cathodic protection to both steel substrates, and the driving force for cathodic protection was lower for the coated DHPF 2.5%Mn steel. Galvanostatic scans were used to evaluate dissolution kinetics of coating phases. Robust cathodic protection was provided by the galvanized coating for austenization times of 30 - 120 s for the 2%Mn substrate and 30 - 60 s for the 2.5%Mn substrate. The duration that robust cathodic protection was provided was shortest at the wall of the U-shape part.

This result was attributed to die wiping caused by DHPF, where the surface is smoothed by die friction. When there is less Γ-Fe_3Zn_{10} in the coating, such as at longer austenization times, surface Γ-Fe_3Zn_{10} was removed and an increased amount of α-Fe(Zn) is exposed, which does not provide robust cathodic protection. In addition, coating cracks form along α-Fe(Zn) grain boundaries after austenization for 180 s on all examined regions of the U-shape part, allowing a greater surface area of the coating exposed to electrolyte, further increasing dissolution of the coating.

ACKNOWLEDGEMENTS

TABLE OF CONTENTS

TABLE OF FIGURES

TABLE OF TABLES

LIST OF ABBREVIATIONS

BSE   Backscatter Electron

CCT   Continuous Cooling Transformation

CGL   Continuous Galvanizing Line

CI   Confidence Interval

DHPF   Direct Hot Press Forming

DI   Deionised Water

ΔE Change in Electrochemical Potential

E_{corr} Corrosion Potential

EDS   Energy Dispersive X-Ray Spectroscopy

F   Faraday's Constant

FCC   Face Centered Cubic

ΔG Change in Gibb's Free Energy

HPF   Hot Press Forming

ICP-OES   Inductively Coupled Plasma – Optical Emission Spectroscopy

LME   Liquid Metal Embrittlement

n   Number of Electrons Exchanged

OCP   Open Circuit Potential

OPS   Active Oxide Polishing Suspension, Colloidal Silica

PAT   Peak Annealing Temperature

PHS   Press Hardened Steel

SCE   Saturated Calomel Electrode

SE	Secondary Electrode
SEM	Scanning Electron Microscopy
SHE	Standard Hydrogen Electrode
UTS	Ultimate Tensile Strength
Wt%	Weight Percent
Vol %	Volume Percent
XRD	X-Ray Diffraction

LIST OF SYMBOLS

Å	Angstrom
α - Fe(Zn)	Zinc Ferrite
cm	Centimetre
°C	Degree Celsius
°	Degree
e^-	Electron
E_{corr}	Corrosion Potential
E_{gc}	Corrosion Potential of Galvanic Couple
G	Gram
i_{gc}	Current Density of Galvanic Couple
K	Kelvin
kEv	Kiloelectron Volt
kN	Kilonewton
λ	Wavelength
MPa	Megapascal
m^2	Square Metre
μm	Micrometre
mA	Miliamp
mL	Mililitre
mm	Millimetre
mV	Milivolt

nm	Nanometre
pO_2	Partial Pressure of Oxygen
s	Second
§	Section
TM	Trademark
V	Volt
vol %	Volume Percent
Wt%	Weight Percent

1 INTRODUCTION

With the increasing concern for the environment, there is a need for the automotive industry to reduce vehicle weight, and increase fuel efficiency, while improving passenger safety. Manufacturers have turned to advanced and ultra high strength steels to help in meeting these goals. In particular, press hardened steels (PHS) are excellent candidates for use in anti-intrusion zones such as the A and B pillar around the front passenger door. Figure 1.1 is the front frame of the 2018 RAM 1500, which is made of over 1/3 PHS [1].
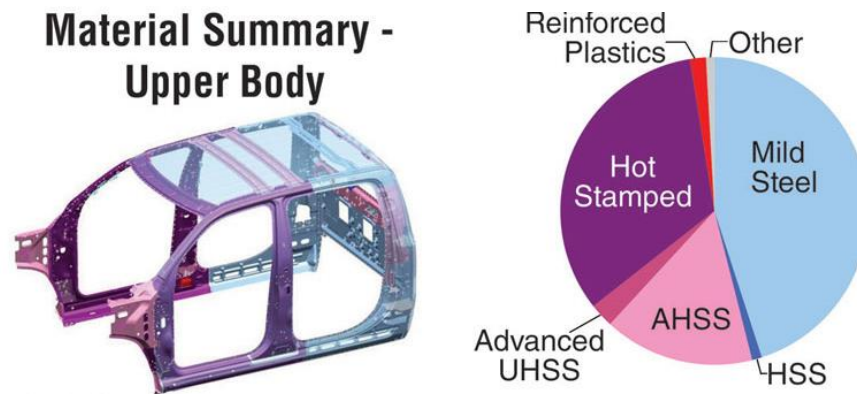
Figure 1.1: Body in white of a vehicle highlighting the use of steel [1].

In addition to possessing strong mechanical properties, it is also desirable to make these parts corrosion resistant. The continuous galvanizing process is a cost-effective method of providing the desired corrosion resistance to steel.

Galvanized coatings provide corrosion resistance by two methods: barrier protection and cathodic protection. The coating creates a physical barrier to prevent oxygen or water from reaching the surface of steel, thus preventing corrosion as the process is dependant on surface reactions [2]. For a coating to provide effective barrier protection the coating must be a solid, continuous layer and be free of defects.

In cathodic protection, one element (Zn) must be more electrochemically active and act as an anode in the galvanic cell and preferentially corrodes compared to the steel. A benefit of cathodic protection is that a full coverage of the part is not required. There is a small distance where cathodic protection still exists, which would protect the steel substrate if there was a small scratch or cut edge. Figure 1.2 shows how this is possible. While the Zn is corroding, electrons travel to the cathode region, where the scratch is located to prevent the exposed steel from losing its metallic ions. For this to occur, there must be significant amount of coating surrounding the exposed substrate for cathodic protection to occur and be effective [3].
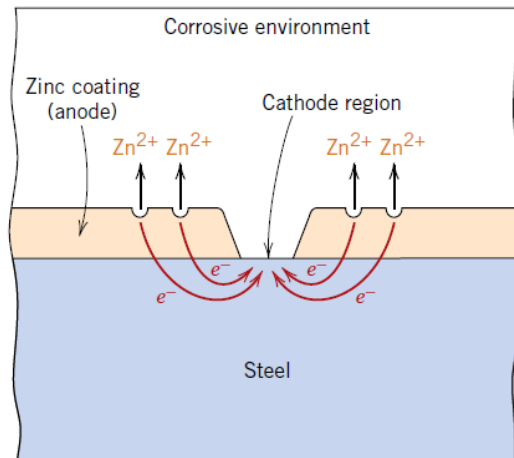
Figure 1.2: A schematic diagram of cathodic protection over a gap in the coating [3].

This work focuses on the ability of a galvanized coating to provide robust cathodic protection after deformation and direct hot press forming (DHPF). Two new PHS grades have been developed that would avoid liquid metal embrittlement (LME), while meeting target mechanical properties [4]. These will act as the substrate of the galvanized DHPF parts.

This thesis consists of seven chapters. Chapter 2 comprises an extensive literature review, detailing the current state of knowledge of DHPF Zn-coated parts, as well as concerns with the

ability of these parts to provide corrosion resistance. Chapters 3 and 4 consists of the research

objectives and a detailed description of the experimental methods, respectively. Chapter 5 will

share the experimental results, which is discussed in Chapter 6. Conclusions from the research

were drawn and recommendations for future work made in Chapter 7.

2 LITERATURE REVIEW

2.1 PRESS HARDENED STEEL

PHS have been used for automotive applications since the 1990s [5]. They are typically

used for anti-intrusion areas in the body-in-white (Figure 1.1). Therefore, it is desired for these

steels to have a tensile strength of at least 1500 MPa and a fully martensitic microstructure to

provide passenger safety [5]. These targets are often achieved by altering the chemical

composition of PHS. The chemical composition of several PHS are shown in Table 2.1. Of

these, the most commonly used grade is 22MnB5 [5].

Table 2.1: Composition of common boron steels used for HPF.

Steel	C	Mn	Si	Cr	B	Al	Ti	Fe
20MnB5 [6]	0.16	1.05	0.40	0.23	0.001	0.04	0.034	Bal.
22MnB5 [7]	0.22	1.17	0.25	0.18	0.0025	0.038	0.028	Bal.
27MnCrB5 [6]	0.25	1.24	0.21	0.34	0.002	0.03	0.042	Bal.
37MnB4 [6]	0.33	0.81	0.31	0.19	0.001	0.03	0.046	Bal.

The main alloying elements in PHS are C, Mn, B and Si. The addition of C, Mn and B

slows the formation of ferrite and bainite during austenite decomposition. This decreases the

cooling rate necessary to achieve a fully martensitic microstructure [8]. C and Mn also decreases

the martensite start temperature [9–11]. However, large quantities of Mn (> 2 wt%) can cause

cracking after quenching [10]. Of the alloying elements discussed, B provides the greatest

improvement to hardenability [10]. It has been cited by Naderi that only a steel that contains B is

able to produce a fully martensitic microstructure after quenching with water cooled dies [6]. Si

acts as a deoxidising agent in steelmaking and for solid solution strengthening, which further

increases the hardenability of the steel [10].

During hot stamping (§ 2.2), austenization is carried out in an open-air atmosphere,

causing the formation of oxides on the bare steel. These are usually removed by shot blasting,

which can be difficult and costly on complex shapes. To prevent steel surface damage and

oxidation, the steel can be metallic coated prior to DHPF.

The most widely used coating for this purpose is an Al-Si alloy (typical composition 7-11

wt% Si, bal. Al) and is widely used under the trade name of Usibor™ [5, 7, 12]. The typical

coating thickness is 25-30 µm. These coatings are also able to decrease the friction coefficient

with the die with increasing temperature, reducing wear on the die and damage to the coating

surface [5, 13]. Si is added to the aluminized coating to create a τ_5-Fe_2SiAl_7 inhibition layer,

which prevents the highly exothermic formation of Fe-Al intermetallic phases. However, due to

the high temperatures in HPF (over 900°C), the inhibition layer breaks down and a series of

intermetallic phases form [14–16]. The cross-section of the Al-Si coating after austenization at

930°C and an isothermal holding time of 5 minutes is shown in Figure 2.3. The microstructure

consists of alternating layers of $FeAl_2$ and Fe_2SiAl_2 [16]. In addition, during the high

temperature annealing, voids form in the coating (seen in the white rectangle in Figure 2.3).

Intermetallic phase transformation and void formation results in higher surface roughness [7].

This can result in adherence to the die surface during hot stamping, potentially causing damage to both the coating and the die.
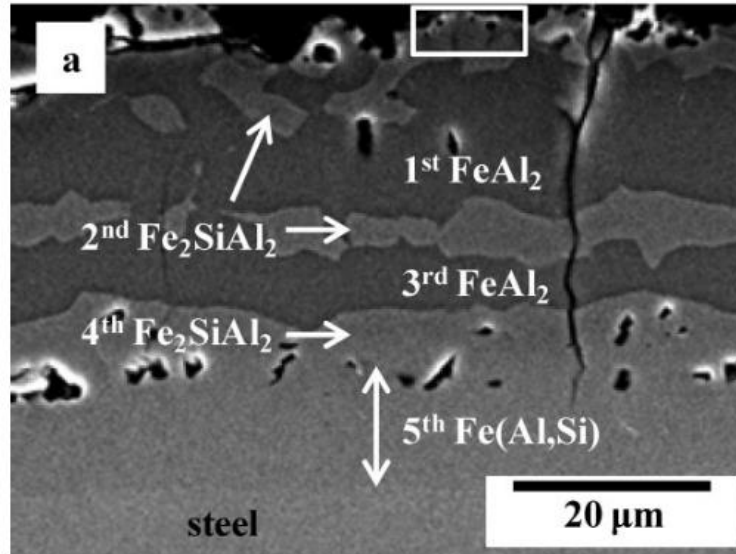
Figure 2.1: Cross-section SEM image of the Al-Si coating after heating in air for 5 minutes at 930°C [7].

However, Al-Si coatings are only able to provide barrier corrosion protection, and do not provide significant cathodic protection to the substrate [5, 17, 18]. Thus, Zn-based coatings are being investigated for this purpose, discussed in § 2.4.

2.2 HOT PRESS FORMING

The use of hot press forming (HPF) for automotive applications began in the 1990s as a way to create high strength parts with complex geometries [5, 7, 13, 19, 20]. This process is often referred to as hot stamping or press hardening as the martensitic transformation occurs during press forming.

There are two methods of HPF, a direct method (Figure 2.2 (a)) an indirect method (Figure 2.2 (b)). Both methods involve an austenitization and quenching stage to ensure the HPF part has the desired microstructure, which will lead to the desired mechanical properties in the finished part. In indirect hot press forming (Figure 2.2 (b)), the part is cold pre-formed prior to austenitization. The die is primarily used for calibration of the part and quenching. In direct hot press forming (DHPF) (Figure 2.2 (a)), forming and quenching are done simultaneously. As the extra step of pre-forming is not required, this process is preferred by the industry and is the method focused on in this work.

The steel blanks used for direct hot press forming (DHPF) typically have a ferrite-pearlite starting microstructure [5, 10]. The steel is first austenitized in a roller hearth furnace (Figure 2.2 (a)) at a temperature between 850-950 °C to create a fully austenitic microstructure. The exact temperature and time for austenitization are dependant on the composition of the steel that is being press hardened. This is usually determined using dilatometry to find the Ac_1 and Ac_3 temperatures when austenization begins and ends. For the most commonly used hot stamping grade, 22MnB5 (composition listed in Table 2.1), it has been found that a minimum annealing time of 3 minutes at 950°C is required to create a fully austenitic microstructure depending on sheet thickness [5, 21]. Austenite at 850-950°C is a much softer and more ductile microstructure than ferrite-pearlite. This greatly improves the formability of the steel and reduces springback, which ensures more accurate forming [5, 20].
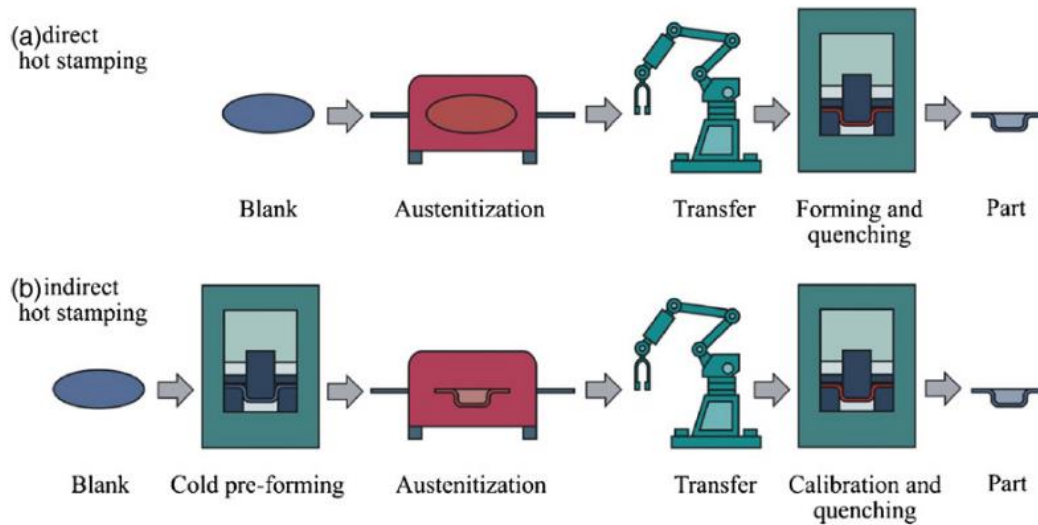
Figure 2.2: Schematic of the (a) direct hot stamping process and the (b) indirect hot stamping process [5].

After austenitization, the steel blank is transferred to water cooled dies (Figure 2.2 (a)), which simultaneously form the part into the desired shape, while rapidly cooling to create a martensitic microstructure. The cooling rate in the dies must be high enough to ensure that the final microstructure of the part is fully martensitic and will have a tensile strength over 1500 MPa. Based on CCT diagrams [9, 22], a cooling rate of –50°C/s should be used to obtain a full martensitic microstructure. However, it has been cited in literature that the minimum critical cooling rate of –27°C/s is required for 22MnB5 [5, 13, 19, 20, 23]. This can be achieved using water-cooled dies.

It is possible to tailor this microstructure of the DHPF part by using different fluids in the die to alter the cooling rate in some areas, creating mixed microstructure parts. For instance, Figure 2.3 (a) shows cooling channels filled with water (for a faster cooling rate) and warm oil (to temper the steel). The resulting part microstructure determined by finite element analysis (Figure 2.3 (b)) shows a mixed martensitic and bainitic microstructure in certain regions [13, 19].

This improves part toughness and may be desirable to increase the part crashworthiness [19]. The steel is then cooled in the dies until the martensitic transformation is complete [11].
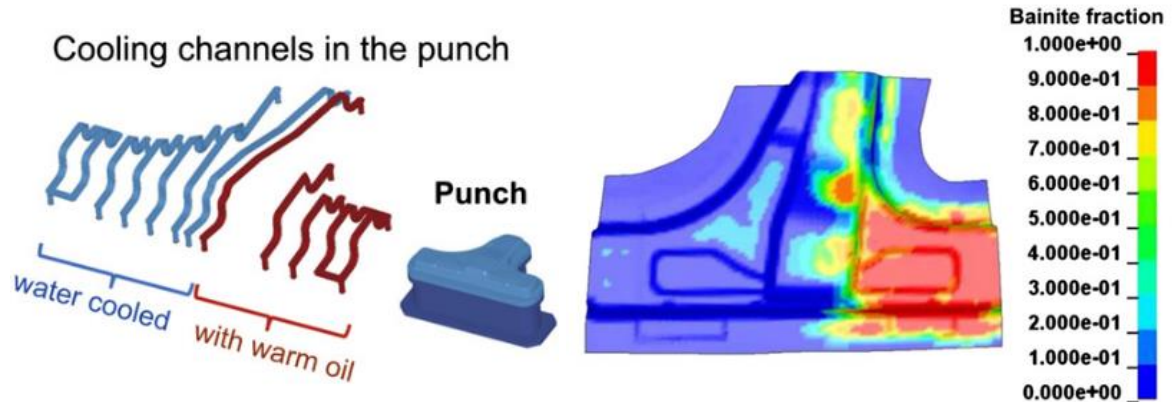
Figure 2.3: Bainite distribution in a hot stamped part created by using different cooling fluids in the die [13].

2.3   THE CONTINUOUS GALVANIZING LINE

The continuous galvanized line (CGL) allows for the cost-efficient galvanizing of steel strip. Figure 2.4 illustrates the commonly used Sendzimir-type hot process continuous coating line.

A detailed explanation of this process has been shared in a review by Marder [2]. Before the steel enters the CGL it is cleaned using a hot (70 – 85°C) 2% NaOH alkali solution, as well as electrolytic methods to remove oils and other surface contaminants. The strip is then dried with pressurized air to remove any moisture. Once strip cleaning is complete, the steel enters a radiant tube heating zone (temperature 500 - 820°C) with a controlled N_2/5-20% H_2 (vol%) atmosphere. The purpose of this process step is to reduce surface FeO $\rightarrow$ Fe, which is done by controlling the process atmosphere dew point, which in turn controls the process atmosphere oxygen partial pressure (pO_2). It is important to control the atmosphere to reduce the presence of

surface oxides, this improving the adhesion of the Zn coating to the steel surface. A secondary purpose of this furnace is to recrystallize or intercritically anneal the steel prior to dipping so that it can have the desired final microstructure when cooled. The steel is then cooled with a gas jet of either N_2-H_2 gas or N_2 with a cooling rate of –20 °C/s - –50°C/s to approximately the bath temperature [24]. The Zn bath for galvanizing is typically kept at approximately 460°C, depending on the composition of the bath and the desired coating. Typical dipping times are between 4-8 s depending on the line speed [2, 25].
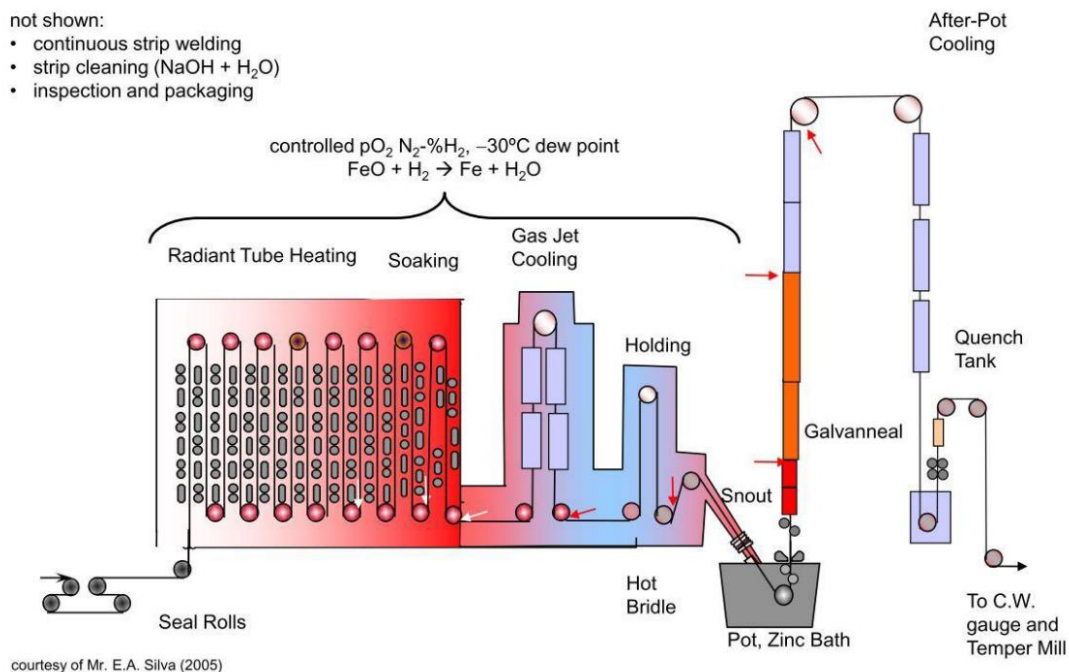
Figure 2.4: Schematic of a Sendzimir-type continuous galvanizing line [26].

In addition to the liquid Zn, the galvanizing bath also contains a small addition of Al (0.12 – 0.25 wt%) and is super-saturated with Fe dissolved from the steel strip [25]. The purpose of the Al addition is to form a continuous $Fe_2Al_5Zn_x$ layer, often referred to as the inhibition layer. This is a very thin layer (50-250 nm) that forms very rapidly once the steel is in contact with the bath [25, 27, 28]. The inhibition layer prevents the interdiffusion of substrate Fe and coating Zn in the

galvanized coating and delays or "inhibits" the formation of brittle Fe-Zn intermetallics, providing better coating adhesion and a highly formable coating [25].

After dipping, excess Zn is removed by air or N_2 gas-jet wiping dies. X-ray or γ-ray measuring techniques are often used to control the coating thickness and ensure even coating coverage [2]. The galvanized steel is then cooled, and final processing or finishing steps can be completed. The cooling tower may also be used as an additional holding furnace to form galvannealed coatings [2]. Galvannealing promotes the formation of Fe-Zn intermetallic phases, as discussed in the following section.

2.4   ZN-BASED COATINGS FOR PHS

2.4.1   Microstructural Evolution

As the galvanized coating is exposed to high temperatures, the $Fe_2Al_5Zn_X$ inhibition layer breaks down and the interdiffusion of Fe from the substrate and Zn from the coating begins. There are several Fe-Zn intermetallic phases found in the Zn-rich region of the binary phase diagram below the peritectic temperature of 782°C (Figure 2.5 (a)). By increasing Fe content these are η-Zn (< 0.03 wt% Fe), ζ-$FeZn_{13}$ (5-6.2 wt% Fe), δ-$FeZn_{10}$ (7-11.5 wt% Fe), and Γ-Fe_3Zn_{10} (23.5-28 wt% Fe) [29]. In addition, a Zn-containing ferrite phase (α-Fe(Zn)) also forms with increasing solubility of Zn, reaching a maximum of approximately 46 wt% Zn at the nominal peritectic temperature of 782°C (Figure 2.5 (a)) [29].
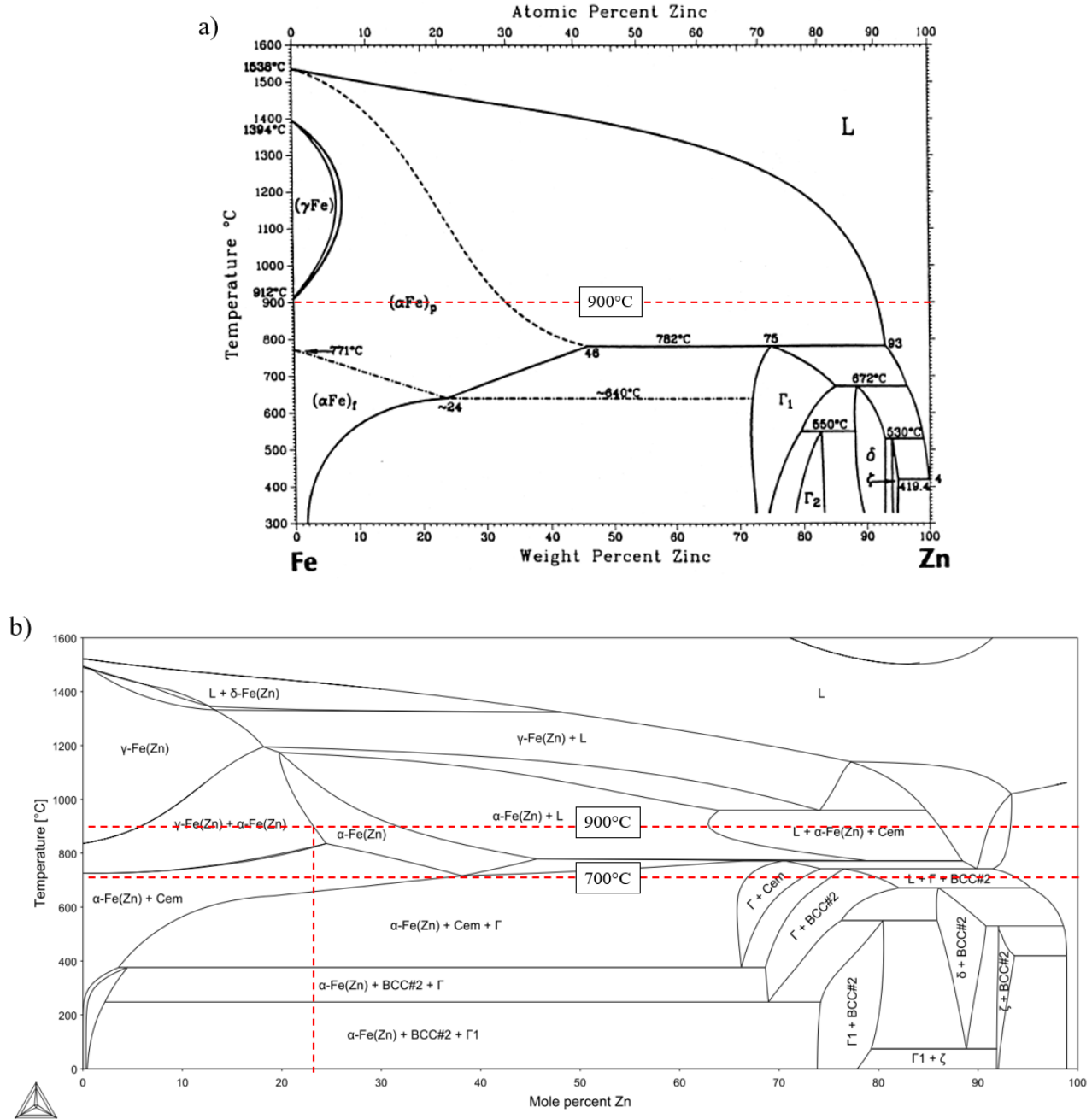
Figure 2.5: a) Binary Fe-Zn phase diagram [30]. b) Fe-Zn-0.2C phase diagram created using ThermoCalc TCFE10 database [31]. The dashed red lines indicate the annealing temperature common for DHPF (900°C), as well as the temperature used for hot stamping in this work (700°C).

Figure 2.5 (a) shows a phase diagram of the binary Fe-Zn system, and Figure 2.5 (b) shows the phase diagram of the Fe-Zn-0.2 C system, which is more applicable to the Zn-based coating on the common hot stamping grade 22MnB5 (full composition listed in Table 2.1). The most noticeable difference between the two phase diagrams is the increase in maximum solubility of Zn in austenite at 900°C from 0 wt% to approximately 23 wt% Zn. In addition, Fe containing less than 5 wt% Zn becomes a Zn-austenite phase, which can be transformed to Zn-martensite upon quenching at the appropriate cooling rate.

Analysis of microstructural evolution by increasing annealing temperature has been completed by several authors [32 – 34]. Cross-sectional images of the coating (Figure 2.6) show concentrations of Fe measured by XRD analysis at increasing annealing temperatures [32].

The melting point of pure Zn is 419.4°C (Figure 2.5 (a)). When the coating is heated above this temperature, it liquifies and there is a breakdown of the $Fe_2Al_5Zn_x$ inhibition layer. Interdiffusion begins between the solid Fe from the steel and liquid Zn in the coating. This causes the formation of ζ-$FeZn_{13}$, followed by δ-$FeZn_{10}$. This can be seen in Figure 2.6 when the coating is heated to 500°C and consists entirely of δ-$FeZn_{10}$ [35]. In addition, due to the complete phase transformation to δ-$FeZn_{10}$, which is thermodynamically stable at a higher temperature, there is no liquid present in the coating.
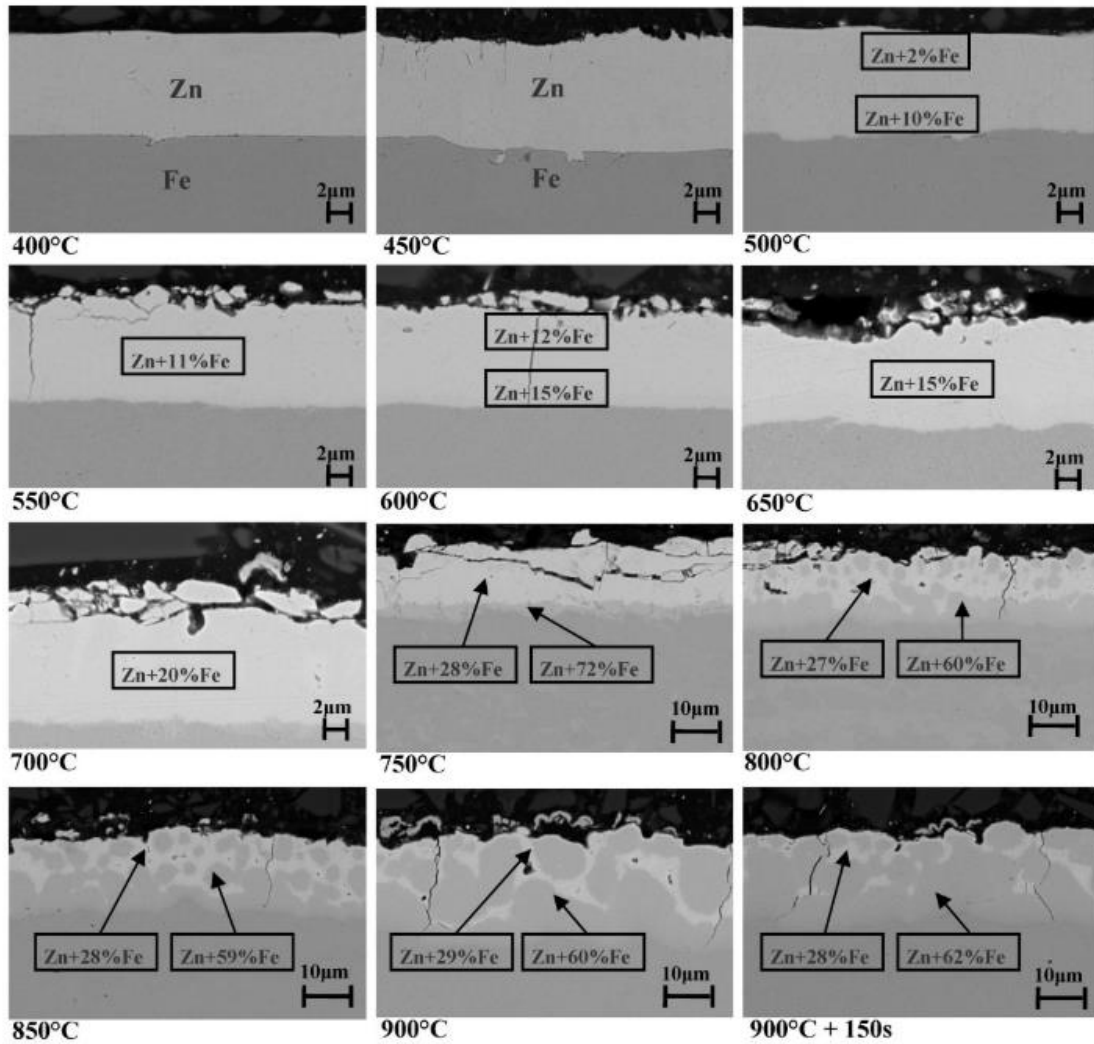
Figure 2.6: Galvanized coating microstructure as a function of annealing temperature. Element concentration in wt% [32].

δ-FeZn$_{10}$ remains as the dominant phase in the Zn-based coating, until the temperature reaches 665°C. At this temperature, the δ-FeZn$_{10}$ is transformed into Γ-Fe$_3$Zn$_{10}$. This can be seen by the increase in Fe content in the coating in Figure 2.6 between 650°C and 700°C. The dominance of Γ-Fe$_3$Zn$_{10}$ in the coating at 700°C is consistent with findings of Dever, who stated that after annealing a similar galvanized steel at 700°C, the coating consisted of only Γ-Fe$_3$Zn$_{10}$ [36].

Above the peritectic temperature of 782°C, Γ-Fe_3Zn_{10} becomes a liquid Zn-Fe alloy. When the steel is rapidly cooled, the liquid Zn solidifies into back into Γ-Fe_3Zn_{10} [7, 33]. However, Autengruber et al. have found that some Γ-Fe_3Zn_{10} remains in the liquified coating at 900°C as the heating rate is too fast for thermodynamic equilibrium to be realized [32]. Γ-Fe_3Zn_{10} is still present in the quenched coating after holding at 900°C, as confirmed by coating phase fractions, determined by XRD analysis is Figure 2.7 [36].
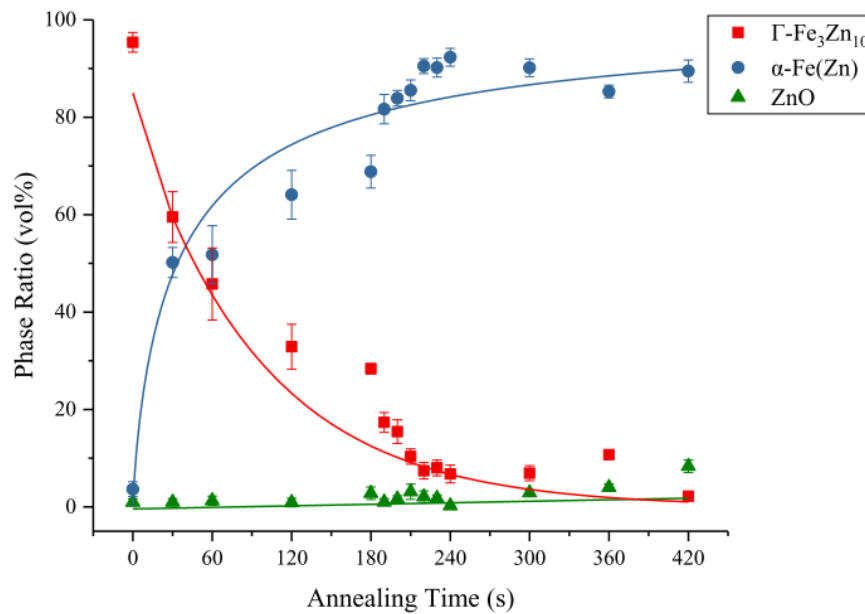
Figure 2.7: Phase ratio of coating phases as a function of annealing time at 900°C in the Zn-based coating on 22MnB5 with an initial coating weight of 70 g/m^2/side [36].

At the same time, α-Fe(Zn) begins to form as a thin layer at the coating/steel interface due to the diffusion of Zn into the steel. This causes interface becomes more wavy due to the increased interdiffusion coefficient at higher temperatures [34].

With additional holding time at 900°C, α-Fe(Zn) becomes the dominant solid phase and continues to grow into the substrate, causing the coating thickness to increase [32].

Consequently, the phase fraction of Γ-Fe$_3$Zn$_{10}$ decreases parabolically with the increasing austenization time, as seen in Figure 2.7 [36]. Conversely, the phase ratio of α-Fe(Zn) increases. At long annealing times, there is adequate time to reach thermodynamic equilibrium. Wang et al. found coating consisted only of α-Fe(Zn) after 300 s in the furnace at 900°C by examining the coating microstructure, but Dever et al. reported Γ-Fe$_3$Zn$_{10}$ by XRD analysis until annealing for 420 s at 900°C [34 – 37]. In addition, the concentration of Zn in α-Fe(Zn) decreases with increasing annealing time, which has an impact the ability of this phase to provide cathodic protection to the substrate [36 – 38].

2.4.2   Surface Oxidation

Ambient air furnaces, usually used for austenization in HPF, allow for the formation of a thin oxide layer on the coating surface. Elements with a high oxygen affinity are often added to steel to allow for hot stamping at temperatures up to 950°C. As the oxide layer that forms is continuous and compact, the evaporation of Zn is prevented when annealing above the boiling point of 907°C [34, 35]. However, the ability of the oxide layer to prevent the evaporation of Zn decreases with increasing annealing temperature as ZnO sublimation begins above the boiling point [7].

A mechanism for the formation of the oxide layer is shown in Figure 2.8, as described by Gaderbaur et al. [39]. Stage I is the galvanized coating prior to annealing. Alloying elements Mn, Cr and Si can all be found in the substrate steel. As the inhibition layer breaks down when the coating liquifies in Stage II, these alloying elements (Cr, Si, Mn) enter the coating [39]. Stage III occurs at 655°C when the coating is entirely Γ-Fe$_3$Zn$_{10}$.

At Stage IV, a layer of Al$_2$O$_3$ and Cr$_2$O$_3$ layer act as a filter, only allowing Zn and Mn to the surface. The final oxide layer consists mainly of ZnO, but Al$_2$O$_3$, and MnO oxides were

found on the surface, as confirmed by several sources [4, 32, 34, 36, 40]. Mn also forms oxides as a mixed spinel $(Mn, Zn)Mn_2O_4$ [39]. Wang et al. found that the surface oxides appeared in clusters when annealed at 885°C, and only became a compact continuous layer after holding for 300 s [34]. As expected, the oxide layer thickness increased slightly with the increasing holding time from 2.02 μm at 300 s to 2.47 μm at 600 s [34].
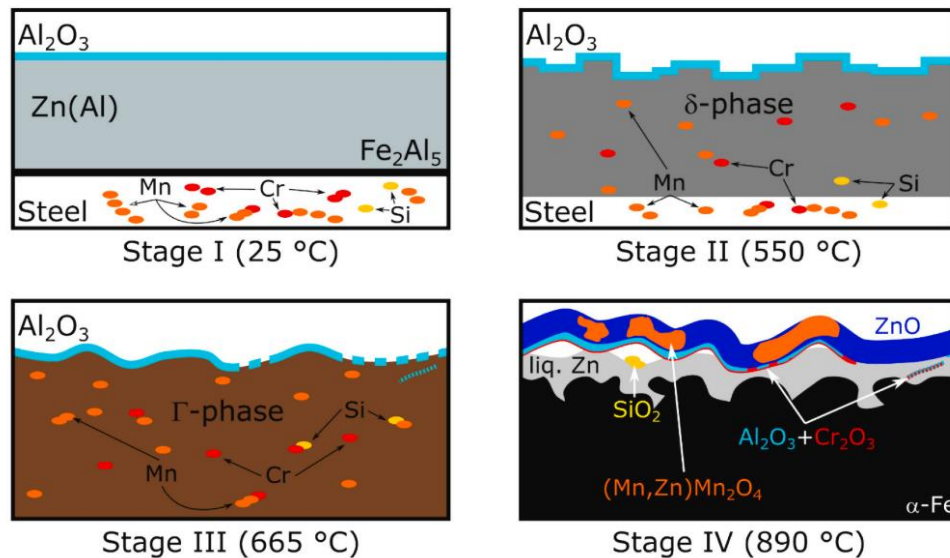
Figure 2.8: Formation of oxide layer in DHPF galvanized steel [39].

Another benefit of the oxide layer is that it prevents liquid Zn from adhering to die and if thin enough (> 2 μm), the presence of this layer does not affect the weldability of the galvanized steel [7]. However, ZnO is typically removed from the surface by methods such as sand blasting to improve paint adhesion and corrosion resistance if the oxide layer is too thick [7, 41].

2.5 LIQUID METAL EMBRITTLEMENT

Liquid metal embrittlement (LME) is a form of environmentally assisted cracking, which can cause sudden and catastrophic part failure. Two central conditions must be met for the

occurrence of LME. There must be a liquid metallic embrittling phase in direct contact with a solid base metal, and the application of a tensile stress [42]. The metal pairings involved tend to be very specific. Usually, the solubility of the liquid metal is very low in the base metal and the embrittling metals often have low melting points compared to the base metal [43, 44]. It has also been cited that LME is also more common if the base metal is FCC [43]. Several systems in which LME have been observed include Al-Ga, Ni-Bi and Cu-Hg [44 – 46]. Typically, until fracture, the stress/strain behaviour is the same as the unwetted material [45].

Currently, there is no universally agreed upon mechanism for LME. A summary of the major proposed mechanisms is shown in Figure 2.9. Several prominent theories are discussed below:

One of the most widely accepted theories is the brittle fracture theory developed by Stoloff, Johnson, Westwood and Kamdar (also referred to as SJWK theory). The embrittling metal would reduce surface energy (or cohesive bond energy) of the solid metal. The application of tensile stress would then break the bonds, which would propagate cracks [45, 47].

A dissolution condensation mechanism was developed by Robertson and Glickman. Robertson proposed the dissolution of base metal atoms into the liquid. When the system was stressed, these dissolved atoms move to the crack tip, and cause crack propagation [48]. Glickman expanded on this, adding that the dissolved atoms are re-deposited onto the crack wall [49].

This model was further extended into a second model: grooving accelerated by local plasticity [50]. Cracks are initiated at grain boundary grooves. The redeposited metal then created a blunt tip, which rapidly propagates the crack.

Lynch proposed a ductile fracture model. The strength of the interatomic bonds at crack tips was weakened by the adsorption of the liquid embrittling metal. An amalgamation of dislocations and micro-voids at the crack tip allowed the crack to propagate until failure [51]. Popovich has proposed a similar model where the absorbed liquid moves the dislocations to the surface, which collect at grain boundaries, resulting in work hardening and crack propagation [46].

A grain boundary model was proposed by Gordon [52]. Liquid embrittling atoms would be absorbed into the solid, and then penetrate into the grain boundaries by stress aided diffusion [52]. This lowers the crack resistance in the grain boundaries, which leads to crack nucleation.
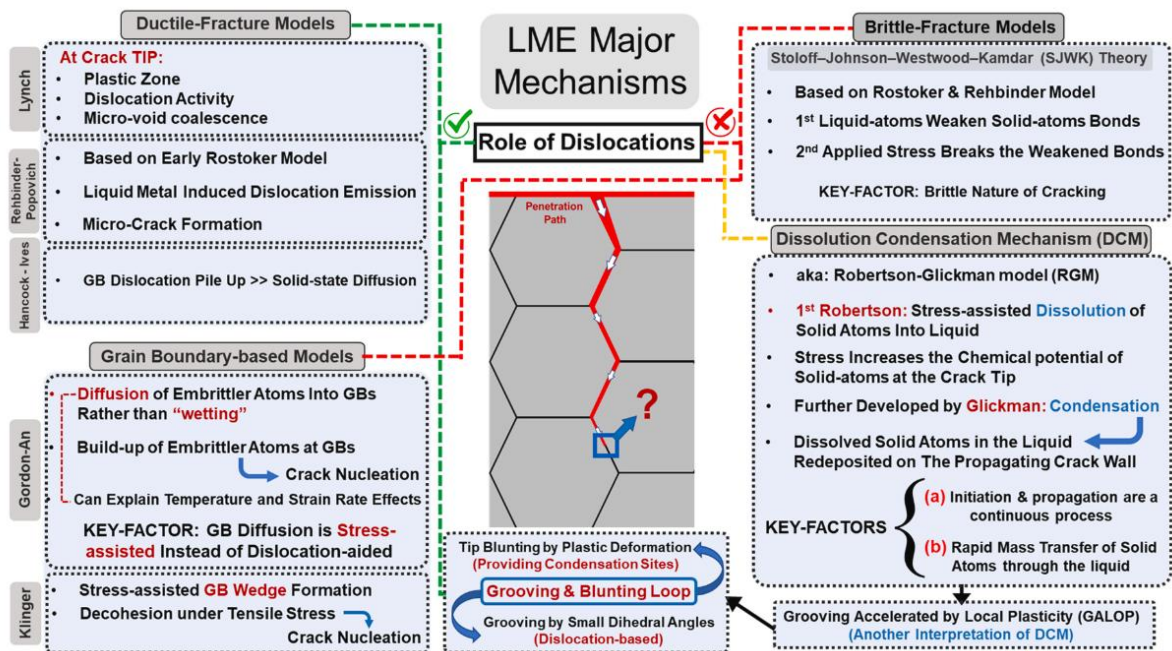
Figure 2.9: Summary of major LME mechanisms [43].

2.5.1   LME in Zn-Coated PHS

LME is a significant issue in the case of Zn-coated PHS during DHPF due to the presence of liquid Fe-Zn and Zn-Fe intermetallic phases being present during the application of forming

stresses to the part [21, 53, 54]. It has been hypothesized that LME is a particular problem on steel, which has a fully austenitic microstructure (such as PHS after austenization in DHPF) [54]. Thus, LME has been a significant impediment in the adoption of Zn-coated PHS in the DHPF process.

Generally, the elastic and plastic behaviour of steel is not altered until premature failure, which makes the fracture very sudden [55]. Stress strain curves by Lee et al. [35] in Figure 2.10 show that LME occurs on galvanized steels deformed at 850°C, typical of DHPF conditions. This specimen had a very small elongation, only 8% compared to the 40% measured on the specimen where LME did not occur.
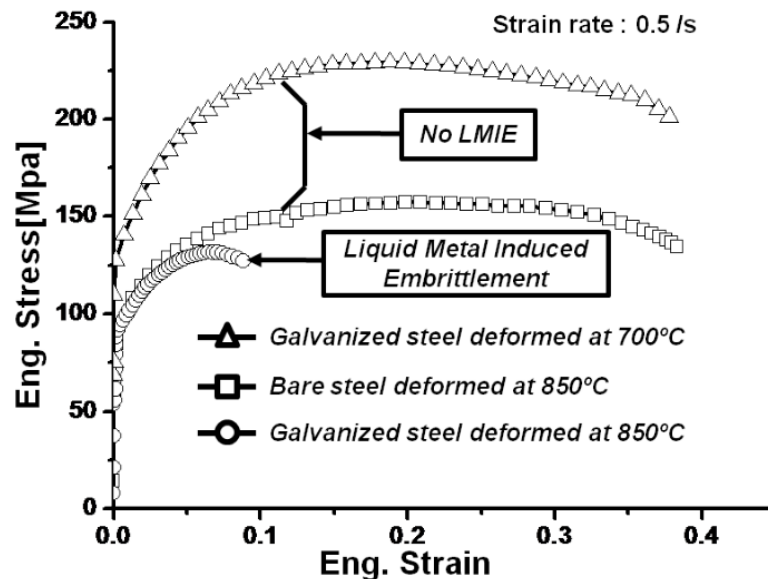
Figure 2.10: Stress-strain curves for steel where LME did and did not occur [35].

A mechanism for LME of Zn-coated 22MnB5 PHS by grain boundary diffusion, proposed by Cho et al. [56], is shown in Figure 2.11. Initial cracks are introduced in α-Fe(Zn) grain boundaries during high temperature deformation. Liquid Zn diffuses through this crack,

and along austenite grain boundaries due to the faster diffusion kinetics of zinc in the grain boundaries. This transforms the grain boundaries into brittle α-Fe(Zn). By capillary flow and the action of the applied stress (arrows in Figure 2.11), liquid Zn continues to enter the α-Fe(Zn) grain boundary, creating more α-Fe(Zn), which allows further propagation of the crack . During rapid quenching, the liquid Zn becomes Γ-Fe$_3$Zn$_{10}$ and the austenite transforms to martensite as shown in the final panel of Figure 2.11. This is consistent with the SJWK theory of LME, where the embrittling metal reduces cohesive bond energy (in this case, by creating brittle α-Fe(Zn) at the crack tip) leading to the propagation of tensile cracks when tensile stress is applied [45, 47].
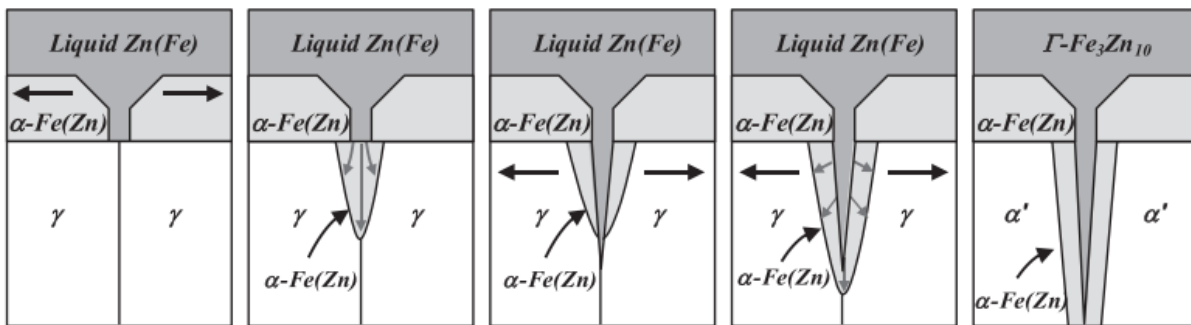
Figure 2.11: Mechanism of LME by grain boundary diffusion [56].

Similarly, Razmpoosh et al. [48] proposed that the grain boundary opening preceded Zn flow. They determined the Zn propagation path is determined by grain boundary energy and misorientation angles, and that higher misorientations angles between grains in the steel require less stress for Zn penetration [48].

2.5.2   Proposed Methods to Avoid LME

Several sources have stated that LME only occurs if there is liquid Zn in direct contact with the steel surface [42, 57 – 59]. In addition, there is an increased sensitivity to LME when there is an increased amount of liquid zinc in contact with the base metal at the deformation

temperature [42]. Therefore, it would be beneficial to reduce the amount of liquid in the coating prior to deformation.

A novel way to avoid LME is to introduce a pre-cooling step into the DHPF process (Figure 2.12) [60]. During the transfer, the steel is cooled only by radiation, which is not a sufficient cooling rate for the solidification of liquid Zn to Γ-Fe$_3$Zn$_{10}$. After the steel leaves the furnace, it is transferred to a pre-cooling unit, which rapidly cools the galvanized steel at a minimum rate of –50 K/s to a temperature just above the martensite start. During this cooling stage, the liquid Zn-Fe alloy in the coating is transformed to solid Γ-Fe$_3$Zn$_{10}$. As there is no longer liquid in the coating, and the piece has not yet been deformed, LME can be avoided. Additionally, the steel is still fully austenitic as it remains above the martensite start temperature, ensuring that a fully martensitic microstructure and desired mechanical properties can still be achieved by die quenching. By pre-cooling the steel, lower holding times in the die may be required.
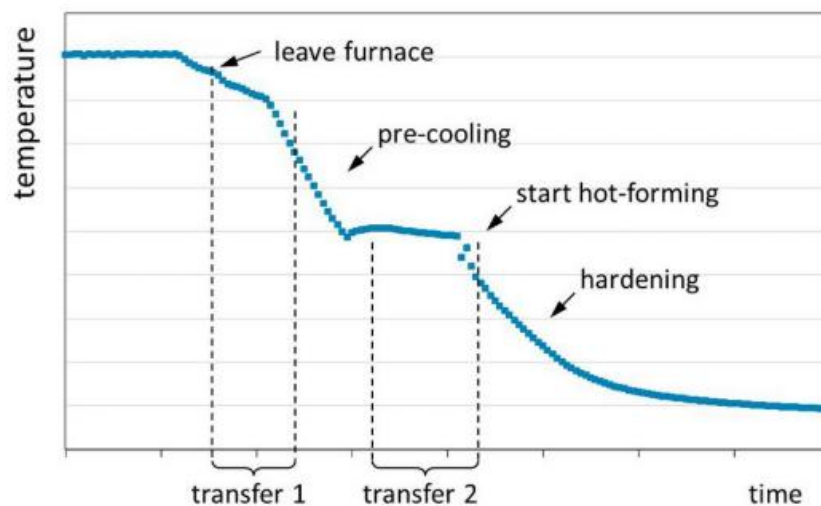
Figure 2.12: Time-temperature diagram with proposed pre-cooling step [60] Note: Times, temperatures and cooling rate were not provided by the authors.

This was tested using a 22MnB5 substrate to create a top hat shaped HPF part illustrated in Figure 2.13 (a). Figure 2.13 (b) shows cross-sectional images of the part at various locations after traditional DHPF. There are cracks going into the substrate at the inner wall and particularly deep cracks near the top of the part. Figure 2.13 (c) shows the part after the pre-cooling step has been used. There are no cracks in the substrate for this case, showing that LME had been successfully avoided.

(a)   (b)   (c)
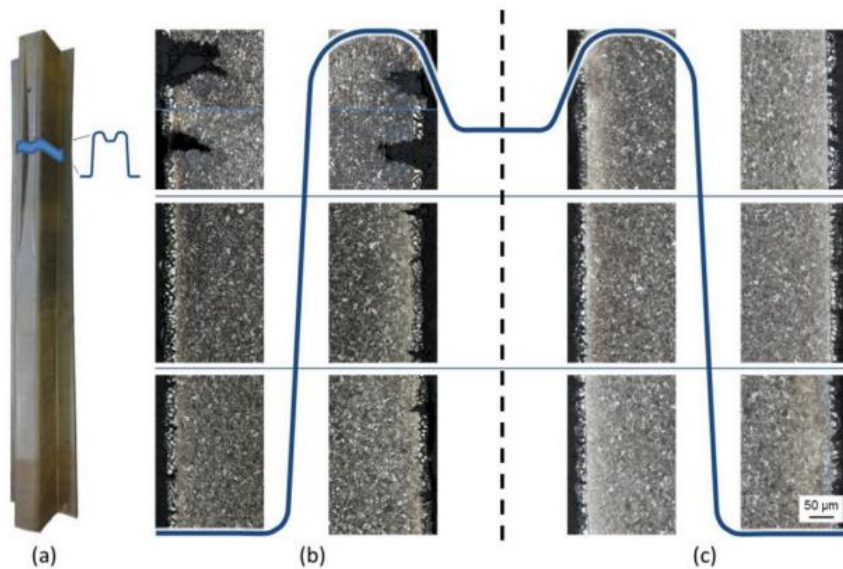
Figure 2.13:Microcracks in a top hat shaped part without (b) and with (c) a pre-cooling step [60].

Recently, two experimental grades of steel have been developed for DHPF at temperatures below the Fe-Zn peritectic (Figure 2.5) to avoid liquid metal embrittlement. These alloys, based on 22MnB5, have an increased amount of Mn, thus shifting the ferrite and bainite nose on the CCT diagrams to the right (Figure 2.14) [4]. These alloys are named based on their Mn content as 2%Mn and 2.5%Mn. Dilatometry on these steels found that the critical continuous cooling rate for the 2%Mn and 2.5%Mn were approximately –10°C/s and –5°C/s, respectively.

This is much lower than the critical cooling rate of –25°C/s required to form a fully martensitic 22MnB5.
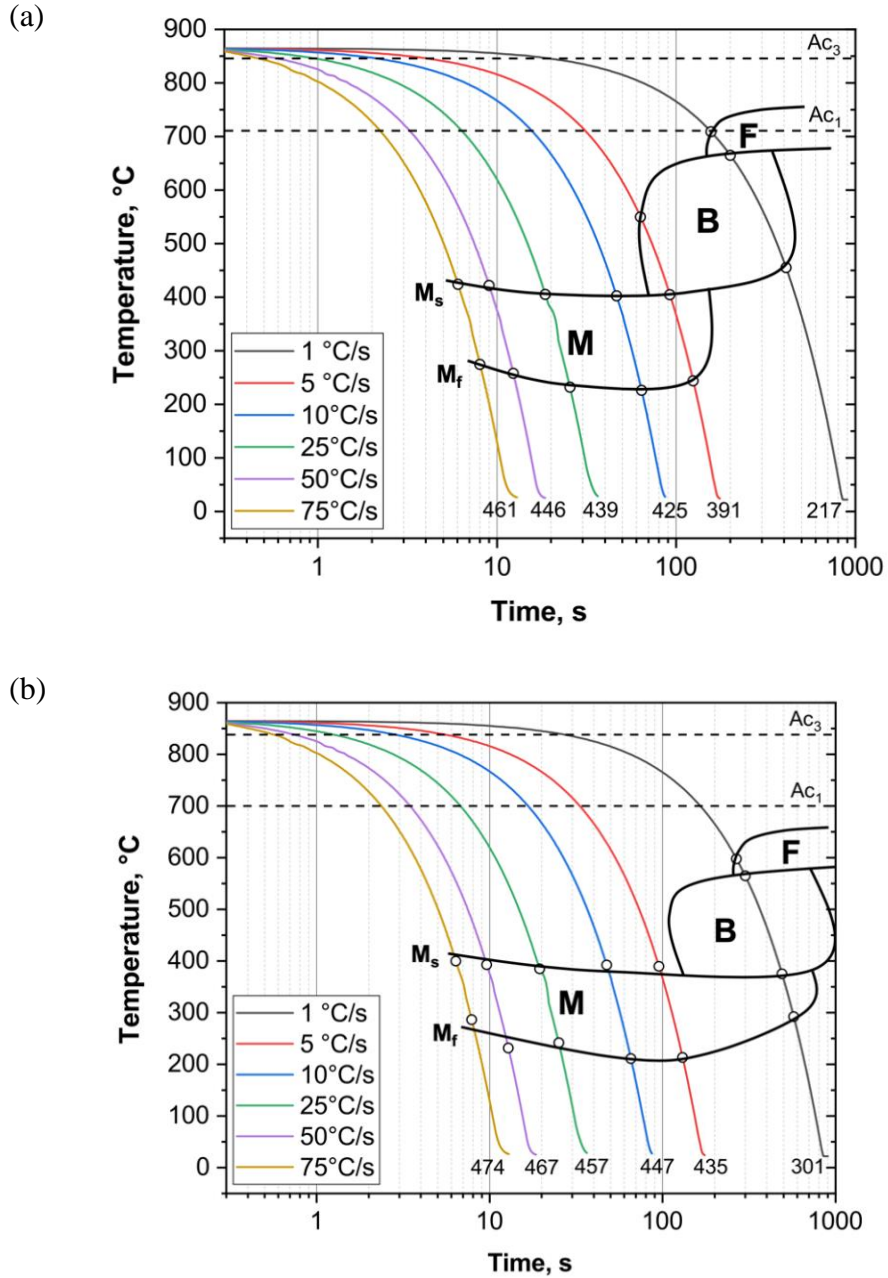
Figure 2.14: CCT diagrams of (a) 2%Mn and (b) 2.5%Mn steel [4].

However, Thomsen also determined that straining the steel caused reduced hardenability and decreased the M_s and M_f temperatures [4]. This agrees with Drillet et al. who determined

23

that the deformation caused by DHPF, particularly in the wall of a U-shape part, causes the CCT curves to be shifted to longer times, and the critical cooling rate needed to be increased to account for this [14]. Samples were austenitized at 890°C and a fully martensitic microstructure was obtained after 120 s for the 2%Mn steel and 60 s for the 2.5%Mn steel [4]. In addition, stamping at higher temperature resulted in more ferrite in the microstructure due to a decrease in time spent at high temperatures required for full austenization [4]. Somani et al. suggested deformation temperatures should be kept above 800°C to avoid a reduction in strength as plastic strain increases the ferrite fraction [61].

Despite this, the target ultimate tensile strength of 1500 MPa and yield strength of 1100 MPa was met on austenization times over 60 s on the 2%Mn steel and over 30 s on the 2.5%Mn steel [4]. Furthermore, the mechanical properties of the top and the wall the U-shape part were found to have similar properties. Lee et al. had also made this comparison and found the same result on 22MnB5 steel. It can be concluded that through U-shape DHPF, the mechanical properties of different areas in the part remain the same [4, 57].

A summary of the mechanical properties is shown in Figure 2.15 for the 2.5%Mn steel austenitized at 890°C and DHPF at 700°C. Thomsen also concluded that there was no significant dependence of stamping temperature between 600-700°C on the mechanical properties and LME has been successfully avoided in all cases [4].
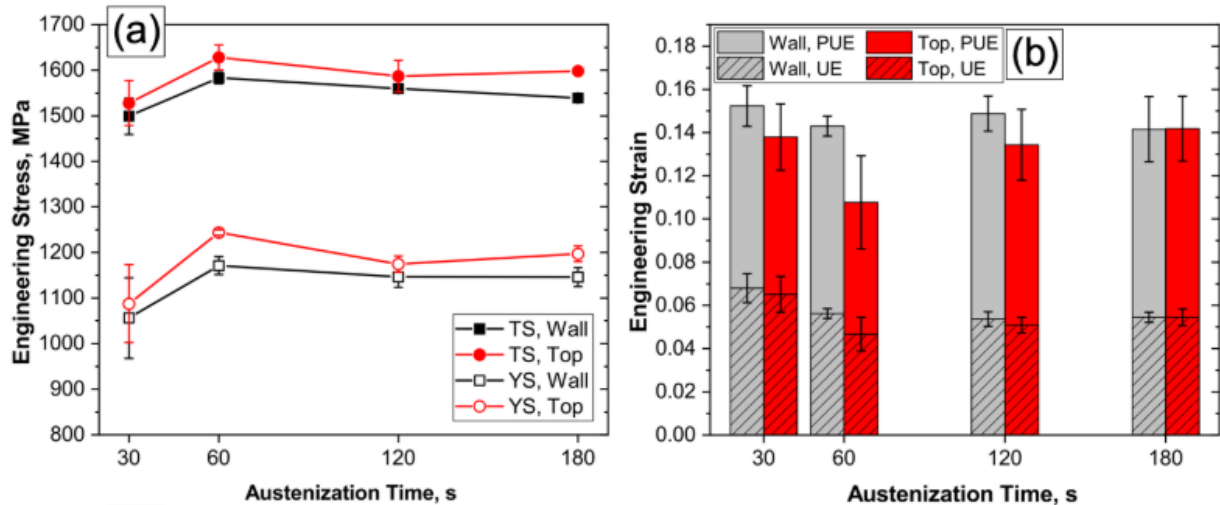
Figure 2.15: Mechanical properties of the 2.5% Mn steel austenitized at 890°C and DHPF at 700°C [4].

The coating phases present on the 2%Mn substrate after hot stamping from 600 – 700°C were also examined by Thomsen (Figure 2.16). Similar to results from Dever on galvanized 22MnB5 annealed at 900°C (Figure 2.7), as well as work by Autengruber et al., the coating consisted of Γ-Fe_3Zn_{10}, α-Fe(Zn) and ZnO [32, 36]. When stamped at 600°C, 650°C and 700°C, the phase fraction of Γ-Fe_3Zn_{10} decreased with the increasing austenization time, while that of α-Fe(Zn) and ZnO increase. In all cases, the target of $\geq$ 15 vol% Γ-Fe_3Zn_{10} that has been required to provide robust cathodic protection, according to Dever, has been met for all austenization times [36]. Therefore, Thomsen has concluded that robust cathodic protection has been provided on the 2%Mn substrate with a Zn-based coating for austenization times of 30 – 180 s when hot stamped from 600 – 700°C [4]. It was also hypothesized that this is true on the coated 2.5%Mn substrate, however full analysis of this was unable to be completed.
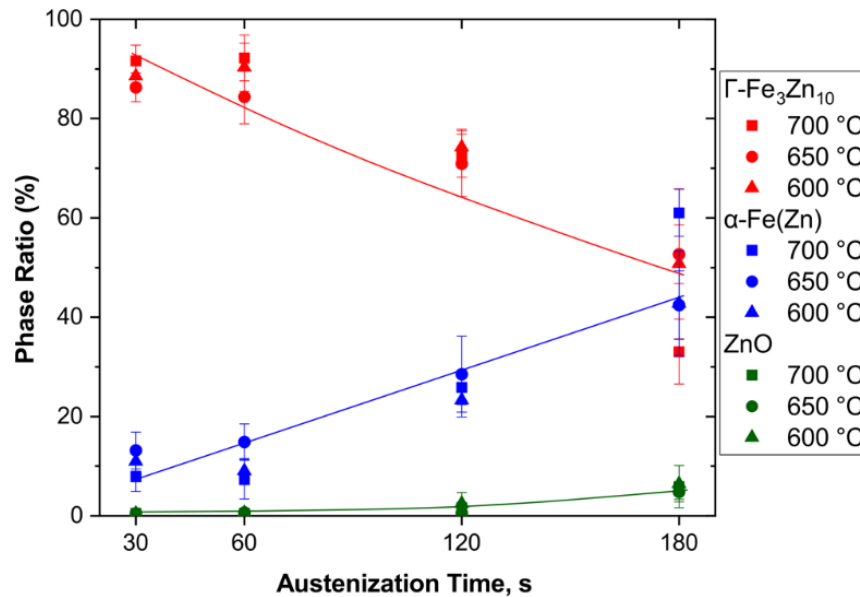
Figure 2.16: XRD analysis of the Zn-based coating on the 2%Mn substrate after austenization at 890°C and hot stamping from 600 - 700°C [4].

2.6 MICROCRACKING

A solid-state diffusion based model for microcrack formation was proposed by Maleki [40]. A schematic of this mechanism is shown in Figure 2.17. During austenization at 900°C, Zn diffused into the iron substrate, as discussed in § 2.4. Fe with a Zn content above 20 wt% became α-Fe(Zn), and that with a Zn below 5 wt% became Zn-austenite (per the phase diagram in Figure 2.5). As the coating α-Fe(Zn) grew into the substrate, a Zn-enriched austenite layer was created with many high angle coincident grain boundaries between the α-Fe(Zn) coating and this layer. Zn diffused along these grain boundaries, causing Zn enrichment, which lead to the formation of α-Fe(Zn). This phase is notably brittle and, therefore, weakened the grain boundaries. This enrichment continued into the austenite grain boundaries, and the substrate austenite grain boundaries, as seen in 2.17.
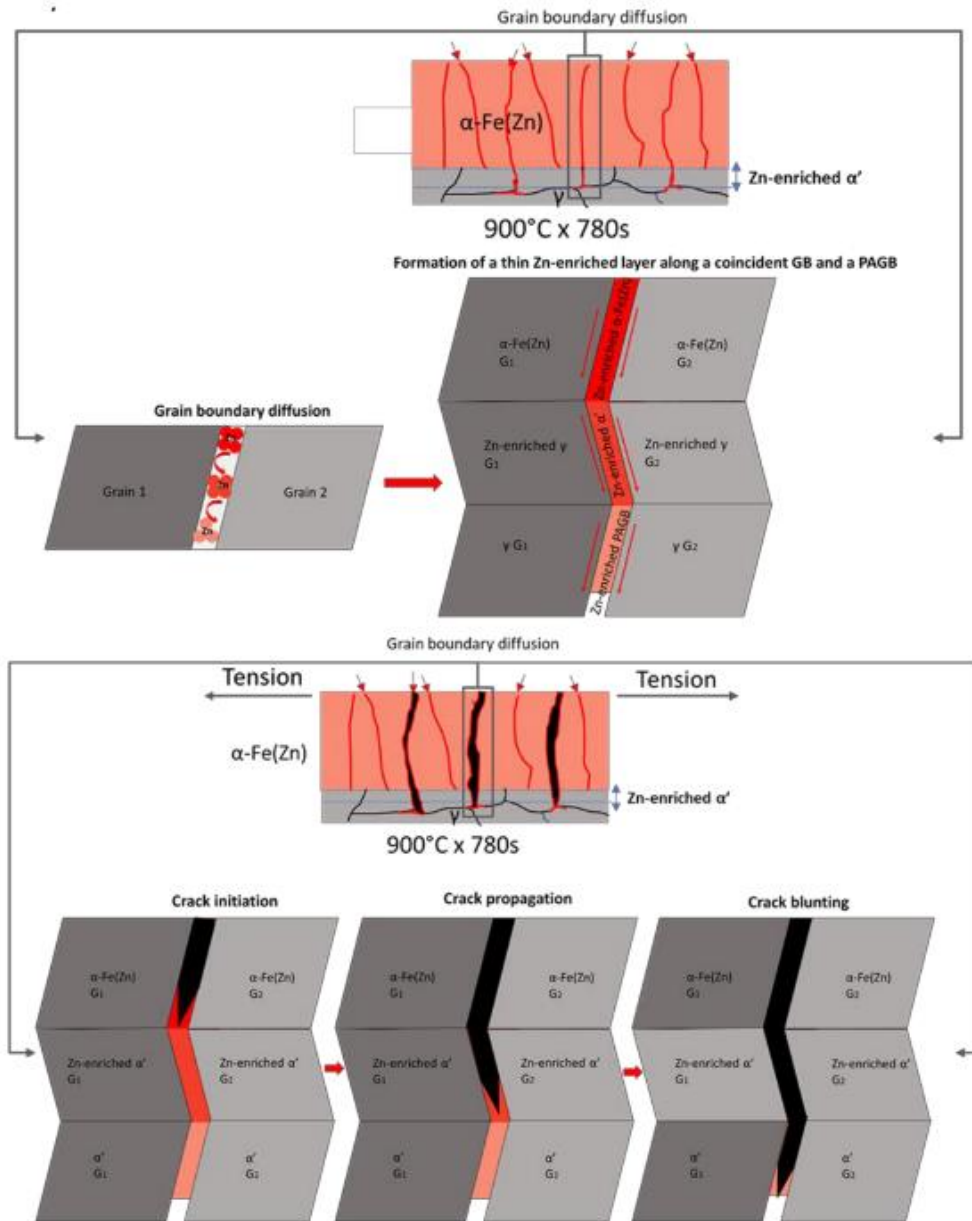
Figure 2.17: Maleki model of the Zn-coated steel microcracking mechanism with coincident zinc ferrite and prior austenite grain boundaries [62].

Due to rapid cooling, the Zn austenite was transformed into Zn martensite in the transition layer, while the grain boundaries were still α-Fe(Zn). When tension was applied, intergranular cracks in the coating were crated along the α-Fe(Zn) grain boundaries. These

continued to propagate along the coincident grain boundaries in the transition layer and the substrate as can be seen in Figure 2.17 and was only stopped when the Zn enrichment was exhausted and the crack tip became blunted.

2.7   COATING DAMAGE CAUSED BY DIRECT HOT PRESS FORMING

As the coating is still liquid on the surface after austenization, the die comes in direct contact with the coating and is able to cause damage. Kang et al. have found that annealing and deformation at 500°C-900°C, such as during DHPF, always results in coating cracks along grain boundaries of α-Fe(Zn) [40, 63]. There are four types of strain that occur in a typical U-channel part during DHPF, strain without contact, pressing, sliding and bending [64]. The type of damage done to the coating depends on which strain mode is active in that region, a diagram of these regions is shown in Figure 2.18 and described below [57].

Region 1 is located at the top of the part. There is little strain or deformation in this area. Here, no visible cracks were found by Lee et al. [57] or Drillet et al. [65] in cross sectional images (Figure 2.18). Thomsen also found no coating cracks at the top of the part on galvanized and similarly DHPF parts of galvanized experimental grades discussed in §2.5 [4]. However, Janik et al. [37] found coating cracks in the top region after annealing for 240 s, but concluded that these cracks must come from quenching as the die does not make direct contact with the coating in this region.
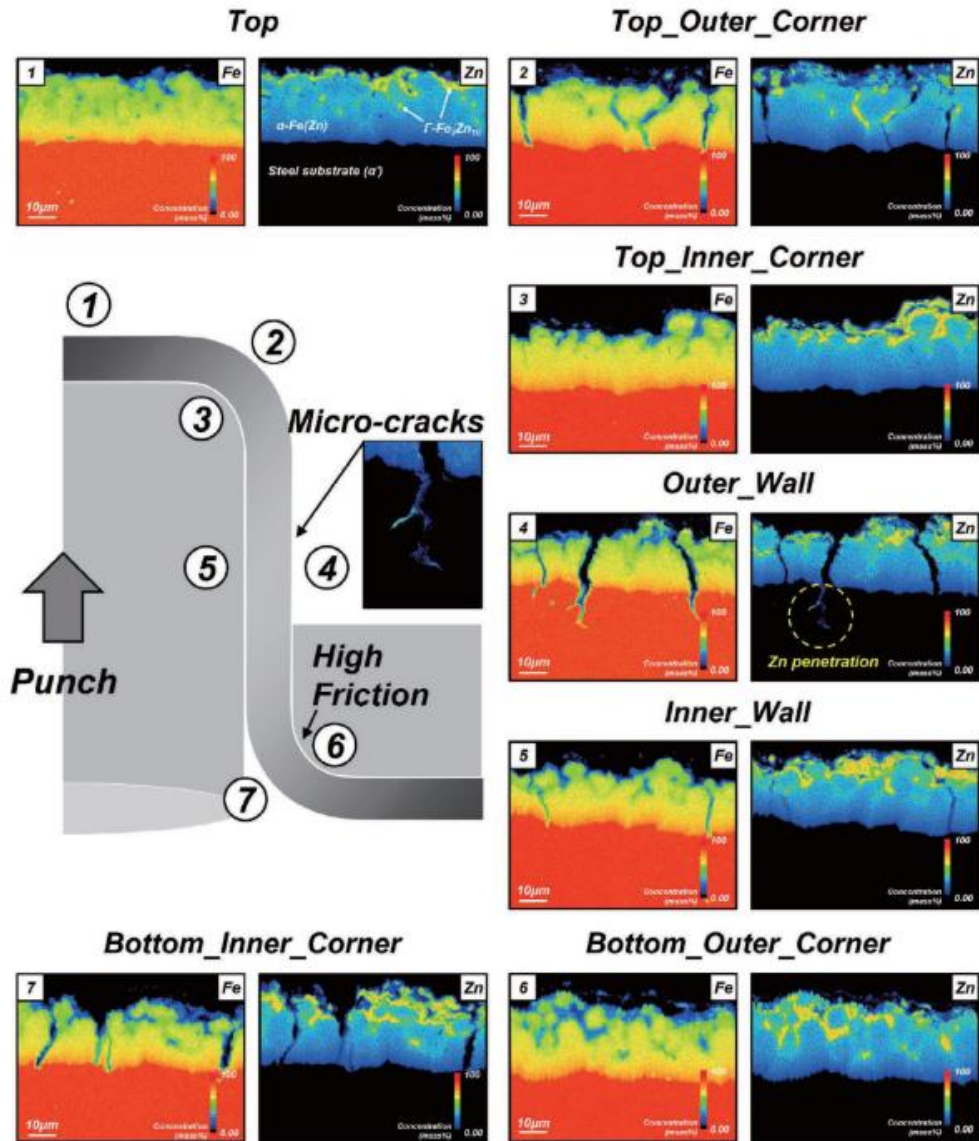
Figure 2.18: Regions of a Top-Hat or U-Channel DHPF part and coating microstructure [57].

At the outer corner of the part (Figure 2.18, region 2 and 7), intergranular cracks are present due the tensile deformation in these areas. The cracks run through the coating – likely along α-Fe(Zn) grain boundaries – but are largely arrested at the coating/substrate interface, although some micro-crack propagation into the substrate was observed. At the inner corners (Figure 2.18, regions 3 and 6), the part was placed in compression. Although there is significant

strain due to the deformation, only minor cracks are present. These cracks, similar to those in the tensile corner, end at the coating/substrate interface.

At the part wall, there is significant friction as the die slides across the coating. This friction plays an important role in coating crack formation in DHPF [63]. At high temperatures (above 800°C) the coating behaves like a viscous fluid, and can easily be deformed and liquid Zn can penetrate into cracks [59, 66]. In this area, the galvanized part is deformed first in compression, then in tension while unbending, before being strained [57]. Cracks form as the die friction presses the coating surface, but the steel substrate (which is not in contact with the die) does not experience die friction. The friction between the die and the coating wipes the surface and presses the Zn further into cracks, resulting in the possibility of liquid metal induced embrittlement. After quenching, Γ-Fe_3Zn_{10} becomes brittle phase which fractures easily and can lead to coating powdering during DHPF [7, 67 – 70]. α-Fe(Zn) is also a brittle phase, and these cracks often occur at α-Fe(Zn) grain boundaries. In addition, at longer austenization times, where there is more α-Fe(Zn) and less liquid, the more likely the coating is to powder with strong friction due to the increased Fe content in this phase .

The sliding friction also causes a decrease in surface roughness. By increasing the sliding speed, the friction between the steel and the die can be lowered, potentially mitigating these effects and reducing crack appearance [64, 66]. Lee et al. has also found that rapid heating will create a smoother surface again, decreasing die friction during HPF [71].

As a result, the tensile bending performance of the samples taken from this region was found to be inferior to those taken from the top [57]. This is particularly noticeable in the direction parallel to the motion of the die, where the wiping occurs.

2.8   CORROSION OF ZN-BASED PHS

2.8.1   Effect of Annealing on Corrosion Behaviour

As discussed in § 2.4, the PHS galvanized coating after DHPF consists of the Γ-Fe_3Zn_{10} intermetallic phase and α-Fe(Zn) with varying Zn content per the appropriate Fe-Zn phase diagram (Figure 2.5) and the Γ-Fe_3Zn_{10} intermetallic phase. Therefore, the coating has different electrochemical behaviour than an undeformed pure Zn (i.e. galvanized) coated steel.

Potentiodynamic polarizations of galvanized PHS annealed for various times at 900°C (Fig 2.19) indicate the coating E_{corr} increases with increasing annealing time [38]. Four groups of curves can be seen. The GI70 steel with a pure Zn coating has the lowest E_{corr} (approx. –1.05 V_{SCE}). The second group has an average E_{corr} = –0.85 V_{SCE}. Based on XRD by the same author (Figure 2.7), the increasing annealing time corresponds to a lower phase fraction of coating Γ-Fe_3Zn_{10}, thus the increased mixed potential. The third group has an average E_{corr} = –0.72 V_{SCE}, and this area corresponds to a coating that consists of α-Fe(Zn) only. The reason for this increase in E_{corr} for the intermetallic phases is the the inclusion of Fe makes the potential more noble. The final curve is the uncoated 22MnB5 steel, which, as expected, has the highest E_{corr}.
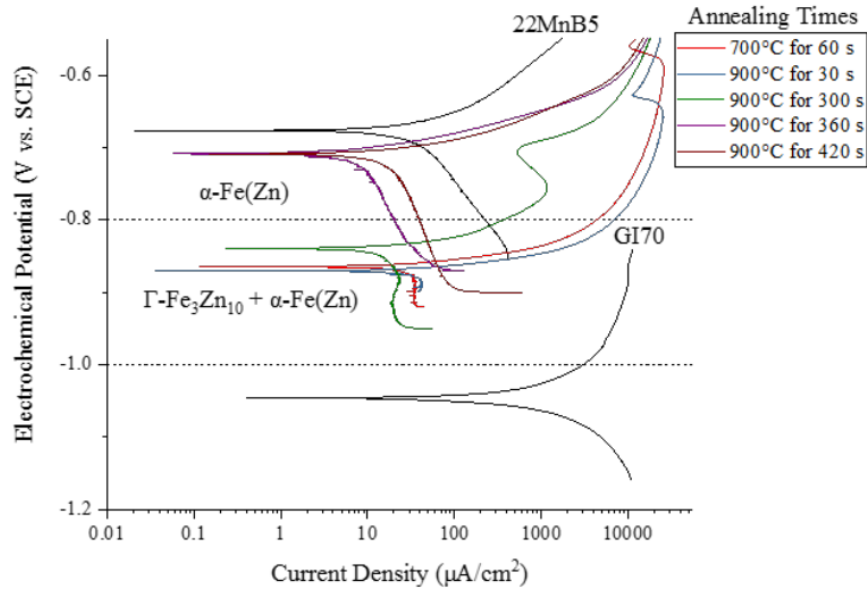
Figure 2.19: Potentiodynamic polarizations of galvanized PHS for various annealing time. Electrolyte composition: 100 g $ZnSO_4 \cdot 7H_2O$, 200 g NaCl, 1000 mL DI water. The scan rate used was 0.167 mA/cm^2 [36].

The driving force for cathodic protection is the difference in E_{corr} between the substrate and the coating phases, as determined by the difference in E_{corr}. This is much smaller for the coatings with only α-Fe(Zn), with $\Delta E_{corr} \cong -0.033$ V_{SCE} whereas it is significantly higher in the mixed Γ-Fe_3Zn_{10} + α-Fe(Zn) coatings with $\Delta E_{corr} \cong -0.176$ V_{SCE}. Dever determined that a minimum of 15 vol% Γ-Fe_3Zn_{10} in the coating was required to provide robust cathodic protection, which was only achieved at annealing times below 240 s [36]. This is supported by Faderl et al. [72], who found there needs to be 70-90 wt% Zn in the coating phase for cathodic corrosion protectioin, a range which include intermetallic Γ-Fe_3Zn_{10}. α-Fe(Zn) only has 17 - 44 wt% Zn, significantly lower than required and, therefore, does not provide robust cathodic protection [7].

Dever also determined that coatings that contained Γ-Fe$_3$Zn$_{10}$ + α-Fe(Zn) would provide cathodic protection for a longer time than those that only contained α-Fe(Zn) [36]. Figure 2.20 shows the galvanic coupling of the mixed phase coating (annealed for 30 s) and that of a coating only containing α-Fe(Zn) (annealed for 360 s) with the 22MnB5 substrate. It can be seen that the anodic current density for the mixed phase coating is smaller than that of the coating comprised of α-Fe(Zn), and, therefore, its dissolution will be a slower rate, providing a longer duration of cathodic protection [36].
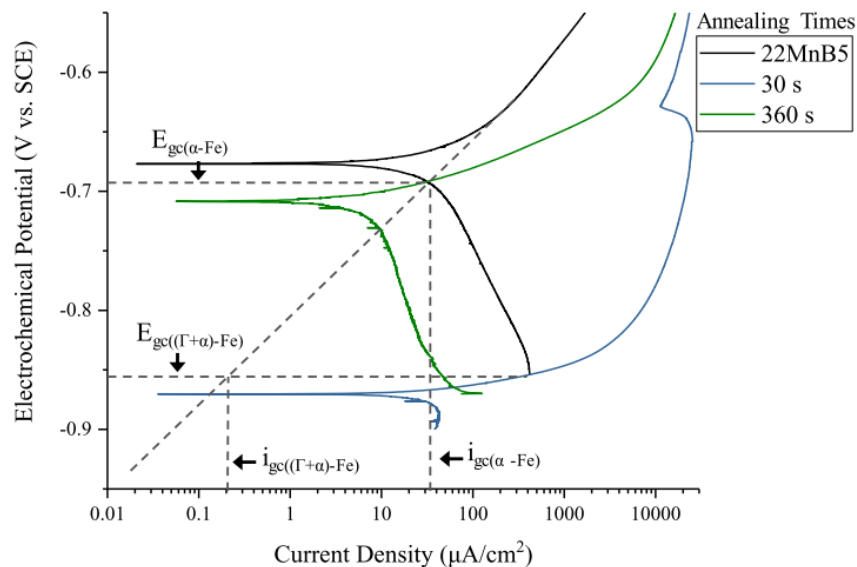
Figure 2.20: Galvanic coupling effects of the coating layer as a function of annealing time at 900°C [36]. Electrolyte solution: 100 g ZnSO$_4$•7H$_2$O, 200 g NaCl, 1000 mL DI water.

Galvanostatic scans preformed by Autengruber et al. (Figure 2.21) have determined that the complete dissolution of a galvanized press hardened coating (annealed for 6 minutes at 910°C) is twice as long as that of an as-coated or "unhardened" galvanized coating. Both the press hardened coating and unhardened coating had an initial weight of 70 g/m^2/side, but the annealing caused the coating to grow from a thickness of 10 μm to 20 μm (as discussed in § 2.4).

The unhardened coating only has two voltage plateaus, one with a potential for the Zn coating and one for the bare steel, which is reached at approximately 30 minutes. This diagram shows a three-plateau structure for the hardened galvanized steel. The first plateau is very short and is the dissolution of Γ-Fe$_3$Zn$_{10}$, which is complete after 5 minutes. The second plateau is the dissolution of α-Fe(Zn), which lasts until 75 minutes. The length of this plateau is increased as the coating becomes thicker, as there is increased coating mass to dissolve. Finally, there is the dissolution of the bare steel. This potential is higher for the hardened galvanized steel than the unhardened galvanized steel as the C content in the martensite is higher than the unhardened galvanized steel with a ferritic microstructure [73].
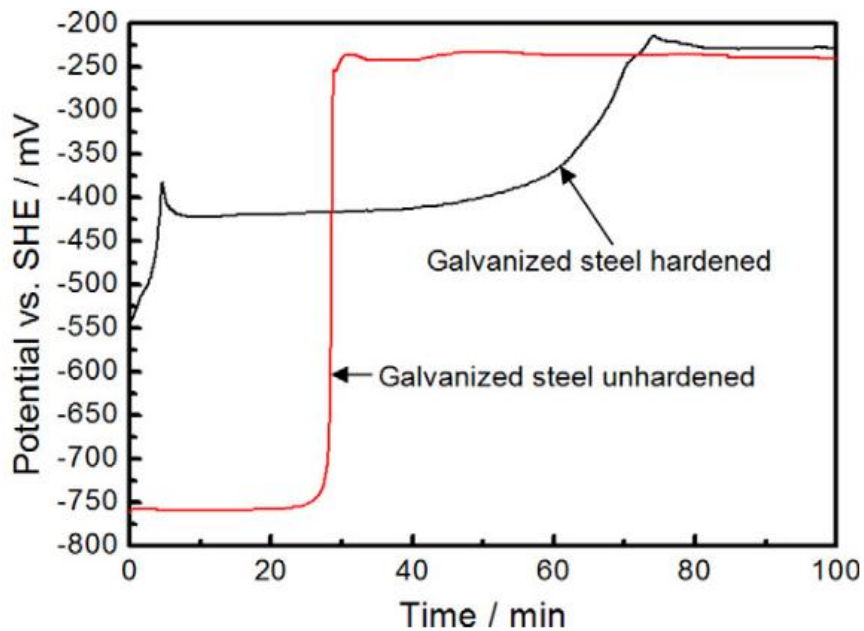
Figure 2.21: Galvanostatic scan of galvanized steel in hardened and unhardened conditions.

Electrolyte: 100 g ZnSO$_4$•7H$_2$O, 200 g NaCl, 1000 mL DI water. Current density 11.76 mA/cm^2

[73].

However, galvanostatic scans completed by Dever showed that this potential increased slightly with increasing dissolution time as the concentration of Zn in the coating decreases over time [38]. In both cases, the galvanized steels that have been press hardened showed higher corrosion resistance, as the dissolution of bare steel began much sooner on the unhardened steel.

In a 10-week salt spray test conduced by Autengruber et al. (VDA 621-415 [EN ISO 11997-1 Cycle B]), it was found that the press hardened galvanized steel coating lasted five times as long than the unhardened galvanized coating [73]. There was no base steel corrosion for the hardened galvanized steel. The increased corrosion resistance observed in the salt spray experiment is attributed to the formation of a dense layer of corrosion products, which provides further barrier protection to the steel [74]. The general trend of corrosion is the active dissolution of Zn followed by blockage from corrosion products [75]. Surface images of the galvanized steel for each week of the test are shown in Figure 2.22.

After one week, the surface of both the hardened and unhardened galvanized steels had been completely covered by corrosion products. On the hardened galvanized steel, this is a light orange colour. Through Ramen spectroscopy and microscopic analysis, this was found to be simonkolleite ($Zn_5(OH)_8Cl_2 \cdot H_2O$). This is very dense corrosion product, and acts as an oxygen barrier, further protecting the substrate [73]. The white corrosion product seen on the surface of the unhardened galvanized steel and in the run-off traces of the salt solution is hydrozincite ($Zn_5(CO_3)_2(OH)_6$) [73]. It is the dominant corrosion product on the unhardened galvanized steel until week 4 of the test, as can be seen in Figure 2.22.
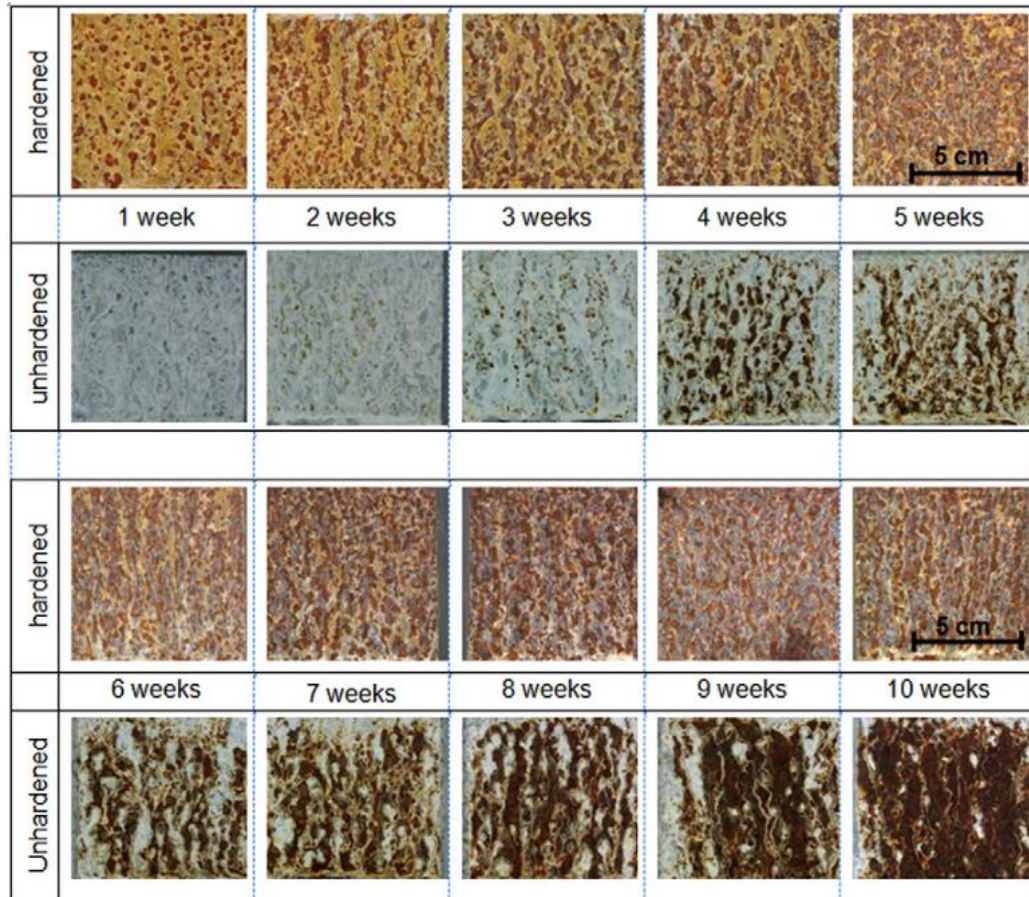
Figure 2.22: Surface images of hardened and unhardened galvanized steel over a 10-week VDA 621-415 [EN ISO 11997-1 Cycle B] salt spray test. The electrolyte consisted of a 5 wt% NaCl solution at 35°C [73].

The dark red corrosion product has been found to be akageneite (β-FeOOH) [74]. Although the presence of akaganeite seems like evidence of the dissolution of the substrate, the Fe in this phase comes from the Fe-Zn intermetallic phases in the coating, in particular α-Fe(Zn) as it is an Fe-rich phase . Corrosion of α-Fe(Zn) only occurs after the complete dissolution of Γ-Fe_3Zn_{10}, which is why this corrosion product only appears on the steel after long exposures to the salt solution [60]. Dever found that when the volume fraction of Γ-Fe_3Zn_{10} in the coating decreased due to annealing, the volume fraction of akaganeite would increase [36].

This was attributed to the change from Zn-based corrosion to Fe-based corrosion. Akageneite also has the ability to create a dense layer on the surface of the steel and provide further barrier protection to resist corrosion [74, 76].

2.8.2   Effect of Deformation on Corrosion Behaviour

As discussed previously, DHPF can cause surface coating damage, as well as create cracks in the coating that expose the substrate directly to the external environment. Galvanized coatings are able to provide protection over surface defects, as Zn is a significantly more electrochemically active element than Fe [77, 78]. In a salt spray test (VDA 621-415), Dosdat et al. found that galvanized and galvannealed coatings are more resistant to corrosion along cut-edges and scribe than AlSi coatings after DHPF [17]. Lee et al., in another salt fog test (ASTM B117), found that after 240 hours of exposure, the galvannealed steel had the lowest scribe creepage compared to a hot dip or electrogalvanized coating, despite the coating being much thinner than the hot dipped galvanized coating [77].

Strain and deformation also effect the electrochemical properties of galvanized coating. Raja et al. deformed a galvannealed coating in four different strain modes, biaxial strain, plane strain, uniaxial strain and tensile strain [76]. Potentiodynamic polarization curves of the galvannealed steel deformed at various strains are shown in Figure 2.23. In all strain modes, the E_{corr} of the galvannealed steel decreases with increasing strain. At higher strains, the coating corroded at an increased rate when compared to the undeformed steel. This creates more corrosion products on the coating, which as discussed previously can provide barrier protection to the substrate. However, at the higher strains, the coating is no longer able to remain intact and the substrate is exposed. This effect is more pronounced on the galvannealed coating that has been biaxially strained. Biaxial deformation lead to the formation of coating cracks, and an

increased cathodic current density as more of the coating was exposed [76]. Because of this, biaxial stress had the greatest impact on the corrosion of the coating [79]. Sacco et al. conducted a similar experiment, but found that the E_{corr} did not follow a trend, but the E_{corr} varied by ± 30 mV compared to undeformed galvanized coatings [75].
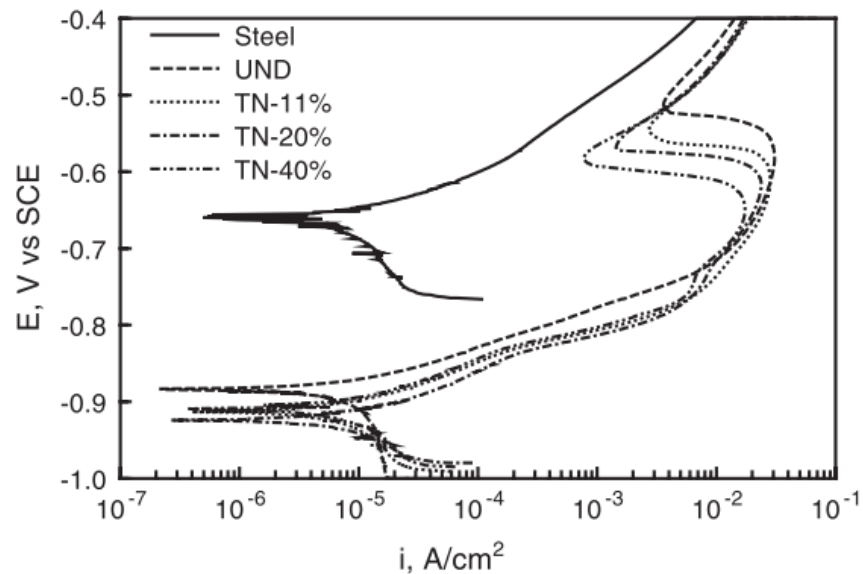
Figure 2.23: Potentiodynamic polarization curves of a galvannealed steel which has been deformed in tension [76].

Furthermore, a salt spray experiment (DIN EN ISO 9227) determined that the low surface roughness and low deformation have a negligible effect on corrosion rate, but that the presence of simonkolleite was greater on the undeformed sample [80]. As simonkolleite has the ability to provide barrier corrosion resistance, a decreased amount of this corrosion product could lead to greater substrate attack after the complete dissolution of the coating [73, 80].

Although these works have been concerned with galvannealed steels, which contain different coating phases than DHPF coatings, which are annealed at a higher temperature

(900°C), they can give some insight into the effects of deformation on the corrosion behaviour of a Zn-based coating.

3   RESEARCH OBJECTIVES

In previous work [4], two novel grades of galvanized steel have been developed that allow for direct hot press forming (DHPF) below the Fe-Zn peritectic temperature, thus avoiding liquid metal embrittlement and catastrophic part failure. It was determined that these galvanized steels could achieve a fully martensitic microstructure with an ultimate tensile strength (UTS) $\geq$ 1500 MPa for austenization times of 60-180 s for the 2%Mn steel and 30-180 s for the 2.5%Mn steel [4]. However, the ability of the coating to provide robust cathodic protection to the DHPF parts created of these steels has not yet been investigated.

The objective of this research is to determine the electrochemical properties of these two new grades of direct hot-pressed galvanized steels, and to further determine the ability of the Zn-based coating to provide robust cathodic protection after DHPF.

By varying the austenization time, the phase fraction of intermetallic coating phases, Γ-Fe_3Zn_{10} and α-Fe(Zn), were altered. Previous work has shown that the coating of both grades contains the minimum required 15 vol % Γ-Fe_3Zn_{10} for robust cathodic protection on flat stamped pieces when stamped at 700°C. However, as discussed in § 2.7, DHPF damages the coating surface, particularly on the part wall and corners, where die friction causes changes in surface texture and intergranular coating cracks. There is concern about the surface Γ-Fe_3Zn_{10}, the intermetallic phase that provides robust cathodic protection to the substrate and is usually located at the coating surface, which is in direct contact with the die. The removal of this phase

may weaken the electrochemical properties of the steel and its ability to provide cathodic protection.

Coating phase fractions, surface and cross-sectional microstructure and electrochemical properties of the coating after DHPF were determined on both the 2%Mn and 2.5%Mn substrate. The effect of DHPF, as well as a comparison between the coating behaviour on each steel were discussed. An updated processing window was determined for these two alloys that would allow for desired mechanical properties (determined in previous work [4]), as well as robust cathodic protection provided by the Zn-based coating.

4 EXPERIMENTAL METHODS

4.1 STEEL

Two steel alloys, developed in previous work, were used as the steel substrates in this project. The composition of the alloys are shown Table 1, determined using ICP. They are referred to based on their Mn content, 2%Mn and 2.5%Mn. The composition of the prototype steels is based on the commonly used hot stamping grade 22MnB5, with an addition of Mn to allow for DHPF below the peritectic temperature of 782°C (Figure 2.5) to avoid LME. Sheets were produced at U.S. Steel R&D Munhall, Pennsylvania. Sheets had an initial thickness of 1.2 mm.

Table 4.1: Composition of Alloys used in this Project (wt%) [4].

Alloy Designation	C	Mn	Si	Cr	P	S	B	Al	Ti	Fe
2% Mn	0.2	2.01	0.26	0.036	0.008	0.0028	0.0046	0.037	0.011	Bal.
2.5% Mn	0.19	2.48	0.26	0.032	0.008	0.0023	0.0049	0.035	0.01	Bal.

Samples were galvanized using the McMaster Galvanizing Simulator at a peak annealing temperature of 710 °C for 120 s using a 95% N_2-5% H_2 process atmosphere with a –30 °C dew point. They were dipped in a Zn bath containing 0.2 wt% Al (dissolved) at 460 °C for 4 s before being cooled to room temperature at a rate of –15 °C/s [4]. The coating weight was measured to be approximately 75 ± 4 g/m^2/side as determined using ASTM A90 [81].
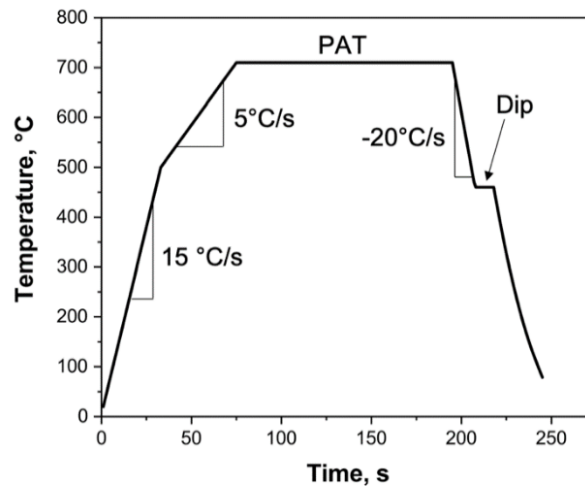
Figure 4.1: Thermal cycle for the McMaster Galvanizing Simulator [4].

The as-recived and as-galvanized microstrucutre of the 2%Mn steel are shown in Figure 4.2 (a) and 4.2 (b). In both cases, the steel has a ferrite-pearlite microstructure. The as-received steel has enlongated ferrite grains and banding, which is attributed to the segregation of Mn during casting. Cementite particles are present along grain boundaries. The as-galvanized 2% Mn steel consists of a recrystallized ferrite-pearlite microstructure, as the annealing temperature was below the austenization temperature. Figure 4.2 (c) is the as-recived microstrucutre of the 2.5%Mn steel, which is similar to that of the 2%Mn steel.
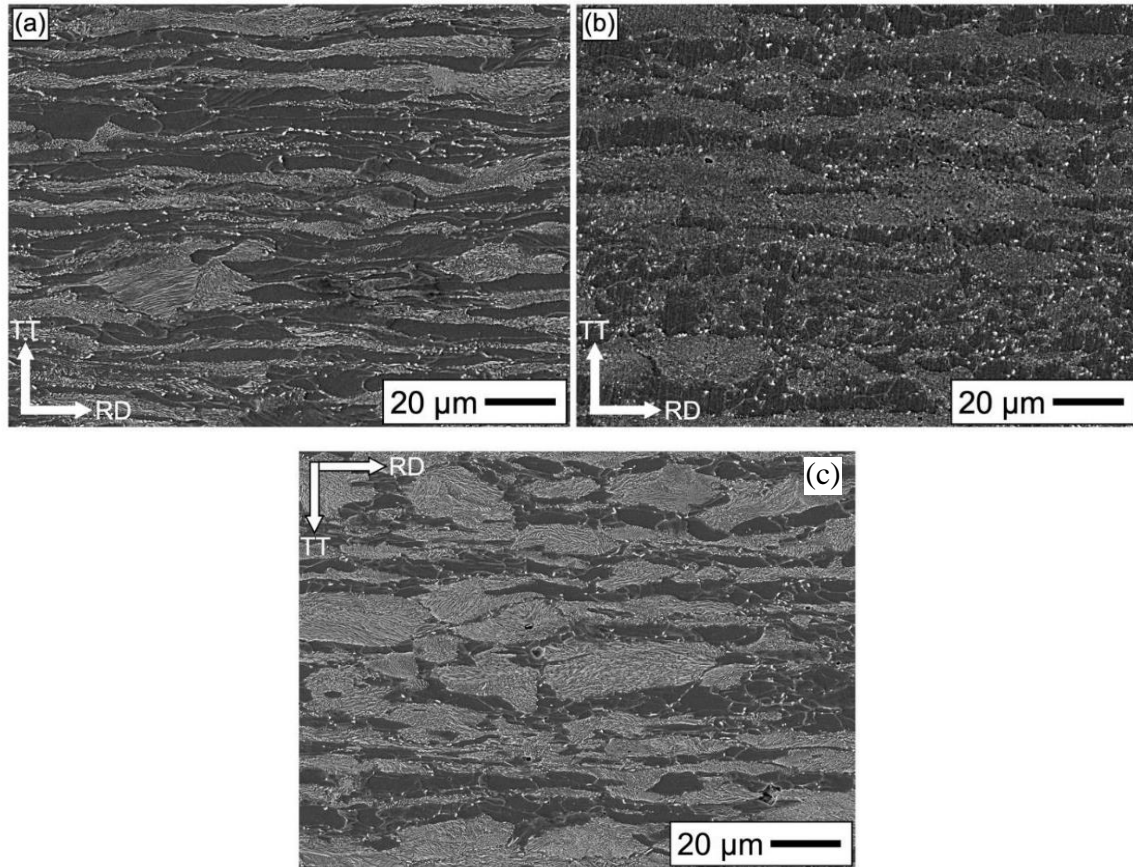
Figure 4.2: SEM micrographs of the 2%Mn (a) as-received microstructure, (b) as-galvanized microstructure and (c) 2.5%Mn as-received microstructure [4].

4.2 AUSTENIZATION AND HOT STAMPING

The galvanized panels were cut into 10 cm by 10 cm blanks for austenization and DHPF. Samples were placed in a preheated box furnace set to 890°C. The furnace was calibrated using a piece of galvanized steel with a welded K-type thermocouple to obtain heating and cooling curves (Fig. 4.3). The measured austenization time began when the samples reached a surface temperature of 890°C, which occurred approximately 160 s after being placed in the furnace. Austenization times used for this project were 30 s, 60 s, 120 s and 180 s. These times were chosen based off previous work to create a mixed phase Γ-Fe$_3$Zn$_{10}$ + α-Fe(Zn) coating that contained a sufficient amount of Γ-Fe$_3$Zn$_{10}$ to allow for robust cathodic protection [36].

(a)

(b)
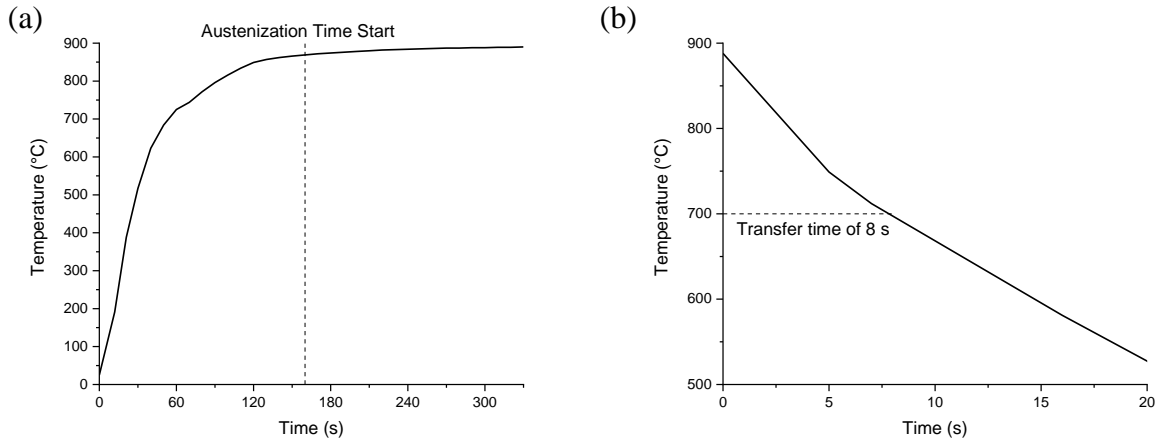
Figure 4.3: (a) Heating curve with labelled austenization start time b) cooling curve with labelled transfer time for stamping at 700°C.

Immediately after austenization, samples were then transferred to a 250 kN tensile frame (Instron) fitted with a U-shape die. The resulting part is shown in Figure 4.4 (a). The DHPF temperature was dictated by the time to transfer the workpiece between the furnace and the tensile frame (Figure 4.3). In this project a transfer time of 8 s was used to obtain a stamping temperature of 700°C.

In addition to these the U-shape DHPF parts, coatings consisting of only Γ-Fe_3Zn_{10} and α-$Fe(Zn)$ were created for baseline electrochemical experiments. One galvanized blank on each steel substrate was annealed at 700°C for 30 s to create a coating consisting of only Γ-Fe_3Zn_{10}. A second galvanized blank of each substrate was annealed at 900°C for 300 s to create a coating of only α-$Fe(Zn)$. These were flat die quenched with water cooled dies immediately after being removed from the furnace. The coating compositions were verified using 2D XRD.

(a)　　　　　　　　　　　　　　　　　　(b)
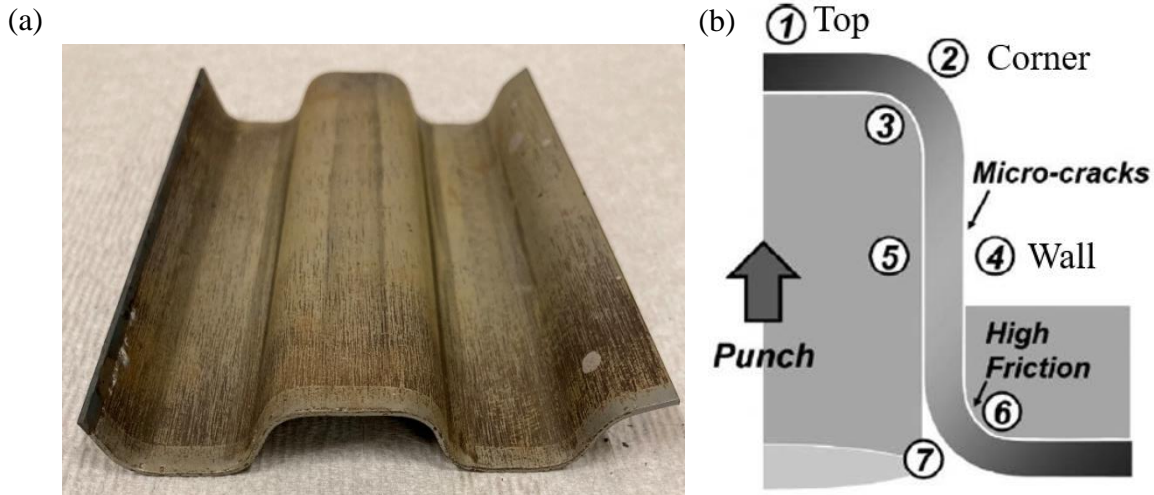
Figure 4.4: a) DHPF U-shaped part stamped at 700°C b) regions of interest on the U-shape part [57].

4.3 X-RAY DIFFRACTION

Two-dimensional X-ray diffraction (2D XRD) was used to identify the phases present in the coating at the top (Figure 4.4 (b), region 1) and wall (Figure 4.4 (b), region 4) of the U-shape part for the experimental austenization times used. Data was collected using a Bruker Mo Smart APEX2 diffractometer. The source used was Co Kα1 radiation ($\lambda = 1.79026$ Å), with a microslit and collimator, both of which were 1 mm. X-rays were generated with a voltage of 35 keV and a current of 45 mA. A coupled $2\theta/\theta$ scan was used with four steps from $11° \leq 2\theta \leq 90°$ and a scan time of 600 s/step. Diffracted X-rays were collected using an Eiger 2R detector.

Raw data was analyzed using Bruker DiffracEva v.5.2 for phase identification. Bruker TOPAS 5 was used to model the measured peaks and determine the coating phase fractions. Samples were measured in triplicate at random points, and a 95% confidence interval of the mean was determined in each case.

4.4   SCANNING ELECTRON MICROSCOPY

Secondary electron Scanning Electron Microscopy (SEM) was used to view the planar surface at the top and wall of the U-shaped part (regions 1 and 4 in Figure 4.4 (b)). Samples were cleaned with acetone and pressurised air before being attached to Al stubs with carbon tape. Imaging was done use a JEOL 6610 SEM, set to a working distance of 10 mm, an acceleration voltage of 20 keV and a spot size of 60 μm to allow for the use of Energy Dispersive X-Ray Spectroscopy (EDS). The detector was calibrated using Cu tape prior to measurement to ensure accurate results.

EDS elemental map scans were acquired to determine the elemental composition of the surface. Data was acquired with a resolution of 1024 pixels per cm for a fixed duration of 5 frames. Point analyses were taken to verify the phases present on the surface of the coating. Triplicate point measurements were taken to in each distinct surface phase seen by the map scans to determine a 95% confidence interval.

Backscatter scanning electron (BSE) microscopy was used to view the cross-sectional microstructure of the mixed Γ-Fe_3Zn_{10} + α-$Fe(Zn)$ coatings. Samples were mounted in cross section using cold mount epoxy resin. They were polished using SiC papers of 320, 600 and 800 grit, using water as a lubricant. Final polishing was done with a NAP cloth and 1 μm water-free diamond lubricant, followed by a CHEM cloth wet with a solution of 50% ethylene glycol/50% OPS. Samples were then C coated and the edges painted with a conductive Ni paint to reduce sample charging in the SEM. Images were taken using the same settings as for the planar SEM at the top, wall and outer corner of the U-shape part.

4.5 ELECTROCHEMICAL CHARACTERIZATION

Stamped U-shaped panels were cut to isolate the top, wall, and corner of the U-Shape DHPF part for electrochemical experiments (regions illustrated in Figure 4.4 (b)). For each sample, an area of approximately 1 cm^2 was marked using vinyl tape as the area of investigation. Cu wire was attached to the back of the sample using conductive Al tape. Epoxy was then used to mask the edges and cover the conductive tape as well as any exposed wire or additional exposed coating not masked off by the vinyl tape. Once the epoxy had cured, the tape was removed to expose the area of interest. This area was measured with the use of vernier calipers to an accuracy of ± 0.01 cm^2 prior to the start of the applicable electrochemical experiment to ensure that an accurate current density could be determined. The sample was cleaned with acetone to remove and oils or dust from the surface immediately before testing.

A three-electrode electrochemical cell was used for all electrochemical experiments on the U-shape part (Figure 4.4). The working electrode was the prepared sample. A saturated calomel electrode with a luggin capillary salt bridge was used as the reference electrode. Two graphite rods acted as the counter electrodes. The graphite rods were attached with a wire to allow for an even flow of electrons in two directions. 750 mL of freshly prepared electrolyte solution was poured into the electrochemical cell prior to the start of each test.

A Gamry Paracell for flat samples was used was used for electrochemical experiments on bare and as-galvanized steel. The samples for these experiments were prepared separately from the procedure discussed above, and only required cleaning with acetone. The area exposed to the electrolyte was a circle with an area of 2.54 cm^2 . This setup (Figure 4.5 (b)) consisted of the sample as the working electrode, a reference electrode with a salt bridge and a carbon rod as the counter electrode. As this cell is smaller, 400 mL of electrolyte was used for each test.

(a)
(b)
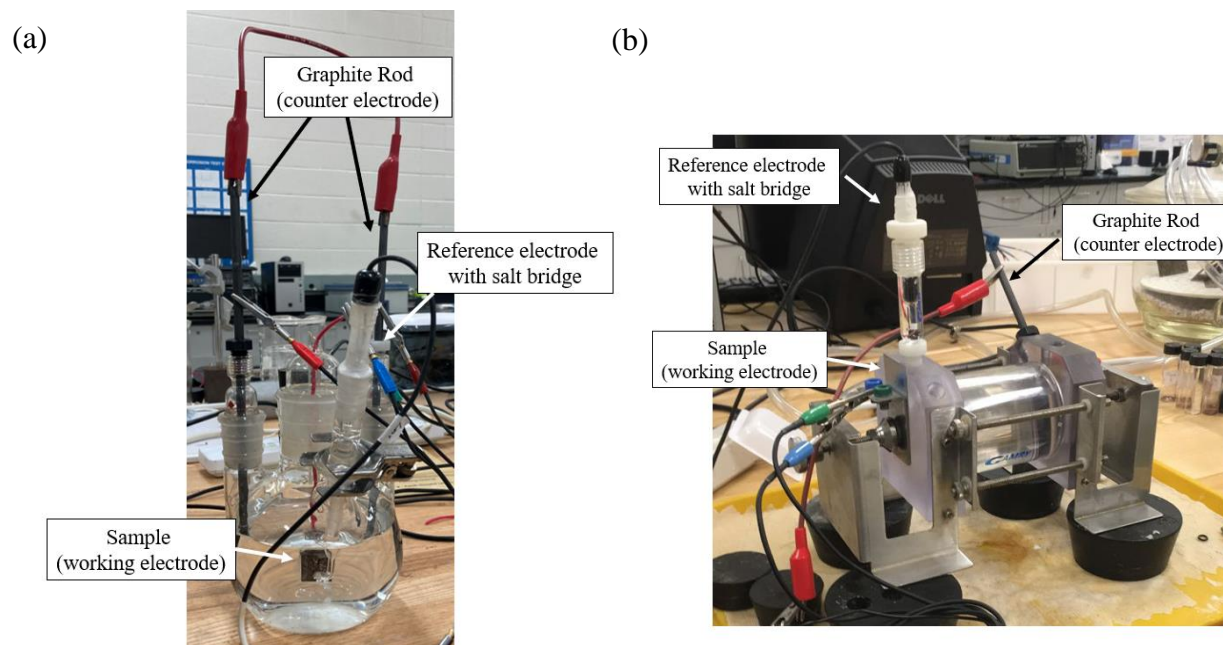
Figure 4.5: Labelled experimental setup for electrochemical experiments a) round flask used for U-shape DHPF samples b) flat cell used for bare steel.

The electrolyte used for all experiments comprised an aerated solution of 100 g $ZnSO_4 \cdot 7H_2O$, 200 g NaCl, and 1000 mL DI water. The concentration of $ZnSO_4 \cdot 7H_2O$ in the electrolyte was such that the solution was saturated with respect to Zn, thus limiting Zn dissolution during testing. The solution had a starting pH of 5.

All electrochemical experiments were conducted using a Gamry 600+ series potentiostat and Gamry Framework software (version 7.8.2). Prior to measurements samples were held at OCP for 600 s to stabilize the system.

4.5.1 Potentiodynamic Polarization Scans

Potentiodynamic polarization scans were conducted to determine the driving force for cathodic protection provided by the coating. This is defined as the difference in E_{corr} between the

phases in the coating and that of the steel substrate. Polarizations were measured continuously between a potential of –1 V to –0.25 V, with a scan rate of 0.167 mV/s. This range was chosen to allow for measurement of a E_{corr} for both of the expected intermetallic phases as well as the bare steel based on similar experiments conducted in previous work [36]. Experiments were conducted in triplicate to ensure reproducibility of the results.

4.5.2   Galvanostatic Polarization Scans

Galvanostatic polarization scans were completed to determine the dissolution kinetics of the coating as a function of austenization time, as well as a function of region in the part. The samples were held in the electrolyte under a constant current density of +10 mA/cm^2 for 8000 s, which was adequate time to allow for the complete dissolution of the coating, as seen in previous work [36, 73].

5   RESULTS

5.1   SAMPLE MAP

A map of the U-shape part, as described by Lee et al. [57], is provided in Figure 5.1. The shape shows half of the U-shape part created during DHPF. Although seven regions are shown in this diagram, this work focuses on three regions: the top (region 1), wall (region 4) and outer corner (region 2). A full literature review of the effects of DHPF on the coating microstructure and surface can be found in § 2.7.
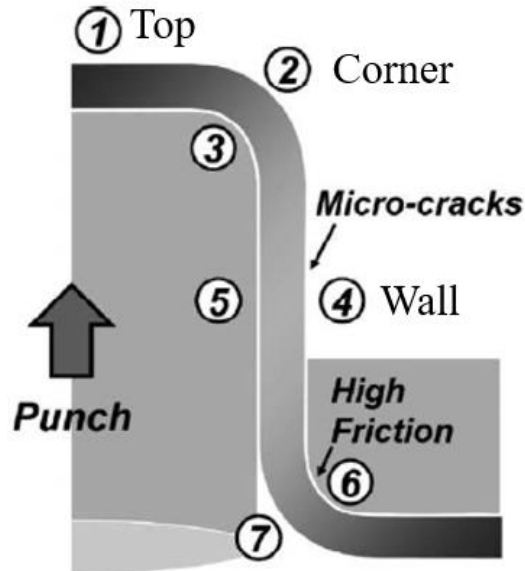
Figure 5.1: Sample map highlighting the regions on the U-shape part [57].

5.2 COATING ANALYSIS ON THE DHPF PART

5.2.1 2%Mn Substrate

Phase fractions of the three prominent coating phases (Γ-Fe$_3$Zn$_{10}$, α-Fe(Zn) and/or ZnO),

as a function of austenization time, determined using 2D XRD, are shown for the top (region 1,

Figure 5.1) in Figure 5.2 (a) and for the wall (region 4, Figure 5.1) in Figure 5.2 (b). This coating

had an initial coating weight of 75 g/m^2/side and was stamped with a U-shaped die at 700°C. At

both the top and wall, the phase fraction of Γ-Fe$_3$Zn$_{10}$ decreased with increasing austenization

time. Inversely, that of α-Fe(Zn) increased with increasing austenization time. This trade-off is

due to the transformation of Γ-Fe$_3$Zn$_{10}$ to the more thermodynamically stable α-Fe(Zn) with

longer holding time at 890°C.

Figure 5.2: Phase fractions within the coating on the 2%Mn steel plotted against austenization time at the (a) top (region 1) and (b) wall (region 4) of the U-shape part. Note that the error bars are 95% confidence intervals of the average reading.

This is consistent with previous work on both galvanized 22MnB5, as well as galvanized 2%Mn steel [4, 34]. However, the volume fraction of Γ-Fe$_3$Zn$_{10}$ was found to be significantly lower for the U-shaped part than samples that have been air quenched or flat die quenched (Figure 2.16). It is hypothesized that the difference is due to surface die wiping and die friction during the DHPF process.

In these plots, the phase fraction of Γ-Fe$_3$Zn$_{10}$ is consistently lower on the top (Figure 5.2 (a)) than on the wall of the part (Figure 5.2 (b)). During DHPF, Γ-Fe$_3$Zn$_{10}$ is spread over the surface of the part due to the punch sliding over the softer phase. This causes a thinner layer of Γ-Fe$_3$Zn$_{10}$ on the surface, and more to be detected in the 2D XRD scans, especially at lower austenization times where there is more Γ-Fe$_3$Zn$_{10}$. On the top, this does not occur, as the die only presses into the surface, rather than wiping.

In previous work, it was determined that a minimum of volume fraction of 15% Γ-Fe$_3$Zn$_{10}$ was required to provide robust cathodic protection to galvanized HPF parts [36]. These experiments were conducted on a galvanized 22MnB5 of a similar coating weight, which is a comparable substrate. However, the annealed galvanized steel was air quenched, rather than die quenched as is the case of current measurements. The minimum of 15 vol% Γ-Fe$_3$Zn$_{10}$ was met for all austenization times on both the top and wall of the part.

Furthermore, after an austenization time of 180 s, the 95% CI in Figure 5.2 yielded large error bars. This was because there was some variation in the phase ratios between two different samples measured, which both experienced the same experimental conditions. Figure 5.3 show the XRD data collected for the two samples, which had both undergone austenization for 180 s at 890°C, taken from the top of the U-shaped part. There is an obvious difference in the size of the

Γ-Fe$_3$Zn$_{10}$ peak (noted by the black triangle in Figure 5.3). Table 5.1 lists the average phase

fraction (vol%) of triplicate measurements, with a 95% confidence interval.

Table 5.1: Phase Fractions of two samples collected from the top (region 1) of the 2%Mn

galvanized part after austenization for 180 s and U-shape DHPF.

Sample	Γ-Fe$_3$Zn$_{10}$ (vol %)	α-Fe(Zn) (vol %)	ZnO (vol %)
1	41 ± 5	53 ± 4	6 ± 1
2	7 ± 2	82 ± 1	11 ± 1
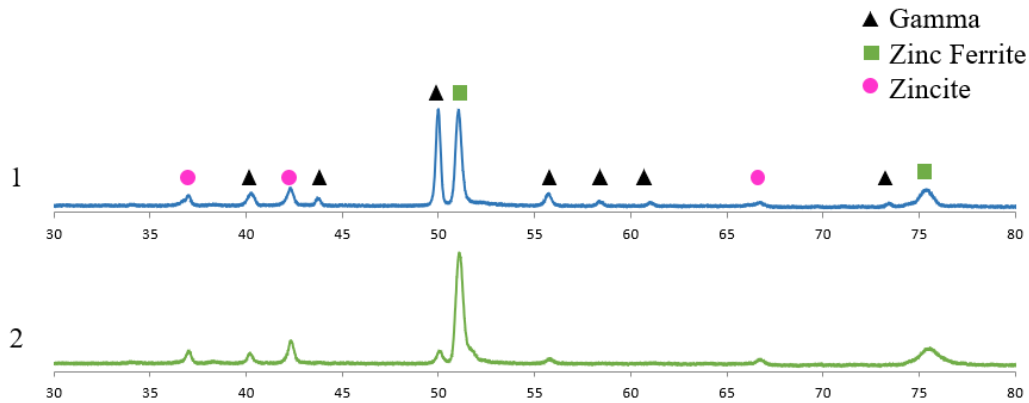
Figure 5.3: XRD data collected in triplicate from the top of the 2%Mn galvanized part after

austenization for 180 s and U-shape DHPF.

Previous XRD analysis of the galvanized 2%Mn steel, also austenitized at 890°C (Figure

2.13) has shown phase fractions that are similar to sample 1 when flat die quenched [36]. The

areas where XRD was measured were randomly chosen, so it may be a matter of selecting

triplicate areas on one part that had experienced greater friction from the die, thus a greater

removal of Γ-Fe$_3$Zn$_{10}$ from the coating surface. The galvanizing simulator, used to galvanize

these samples, may have some variability in coating thickness, which could result in variability

in the coating phases after austenization. In addition, the surface of the samples is extremely

heterogeneous, as is seen in planar SEM shown in § 5.2 of this thesis. A combination of all three factors could lead to the variation seen in these results.

5.2.2 2.5% Mn Substrate

Analysis of the coating phases on the 2.5%Mn steel, determined by XRD, are shown in Figure 5.3 (a) on the top (region 1), and Figure 5.3 (b) (region 4) the wall of the DHPF U-Shape part stamped at 700°C. Similar to the 2%Mn steel, the phase fraction of Γ-Fe_3Zn_{10} also decreased, and the phase fraction of α-Fe(Zn) increased with increasing austenization time. However, the rate of change is much greater on the 2.5%Mn substrate, indicating the formation of α-Fe(Zn) occurred more rapidly for this substrate than in the coated 2%Mn steel.

Furthermore, the volume fraction of Γ-Fe_3Zn_{10} has dipped below the minimum 15 vol% required for robust cathodic protection on both the top and wall of the part after austenization for 180 s. As this requirement has been met on flat die quenched galvanized steel [4], it is again hypothesised that the decreased amount of Γ-Fe_3Zn_{10} in the U-shape DHPF coating is due to die wiping. This is confirmed by an examination of the surface in §5.3.

Large error bars were also seen in Figure 5.4 for samples austenitized for 120 s. There was variation in the coating within one sample austenitized for 120 s sample at the top of the part. While two measurements measured approximately 30 vol% Γ-Fe_3Zn_{10}, a third measurement yielded only 4 vol% of this phase. This indicated that the coating surface is heterogenous and that phase fractions can vary across the same region of the stamped part. Since the amount of Γ-Fe_3Zn_{10} has decreased significantly, it may be more susceptible to corrosion.

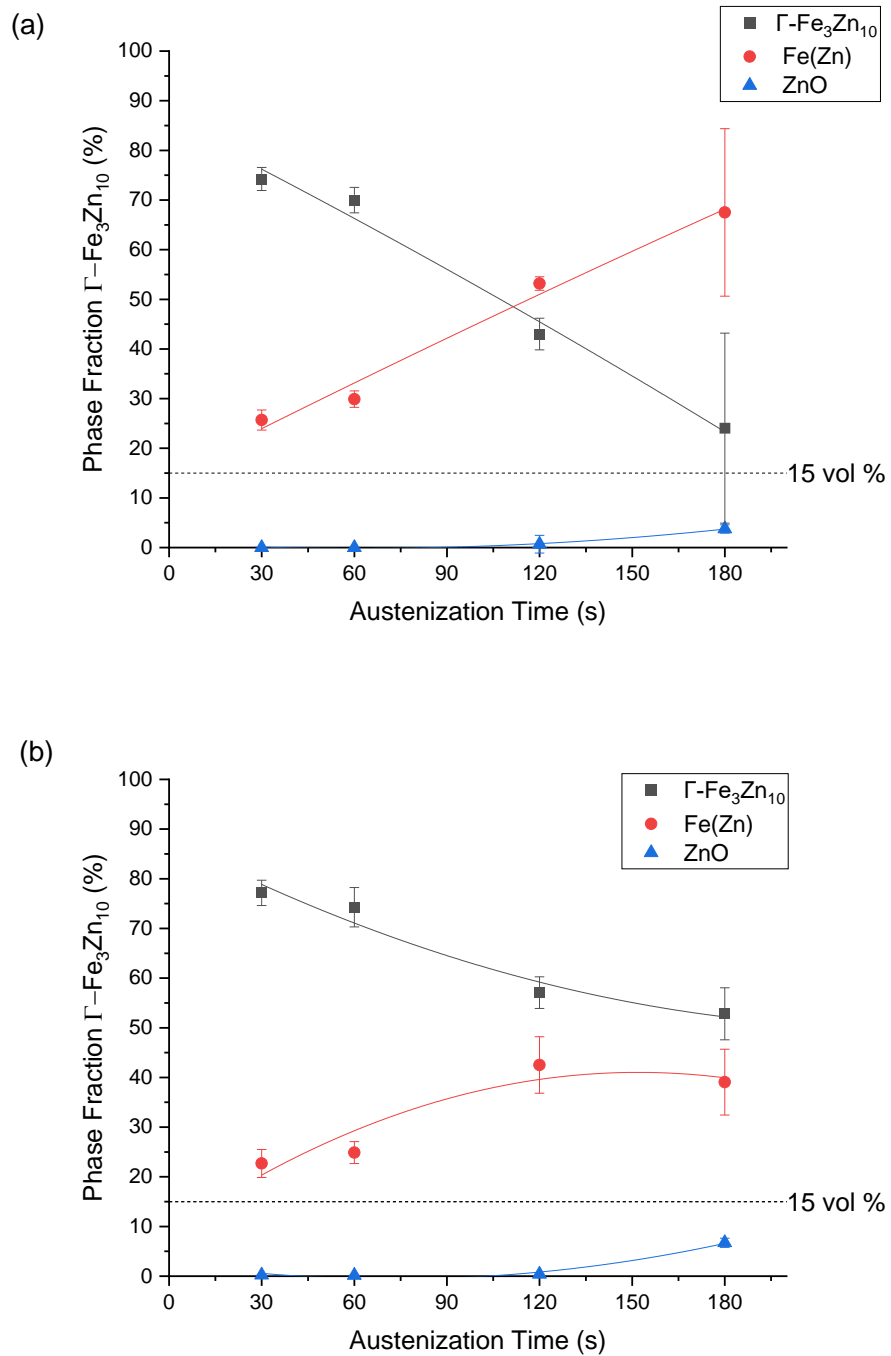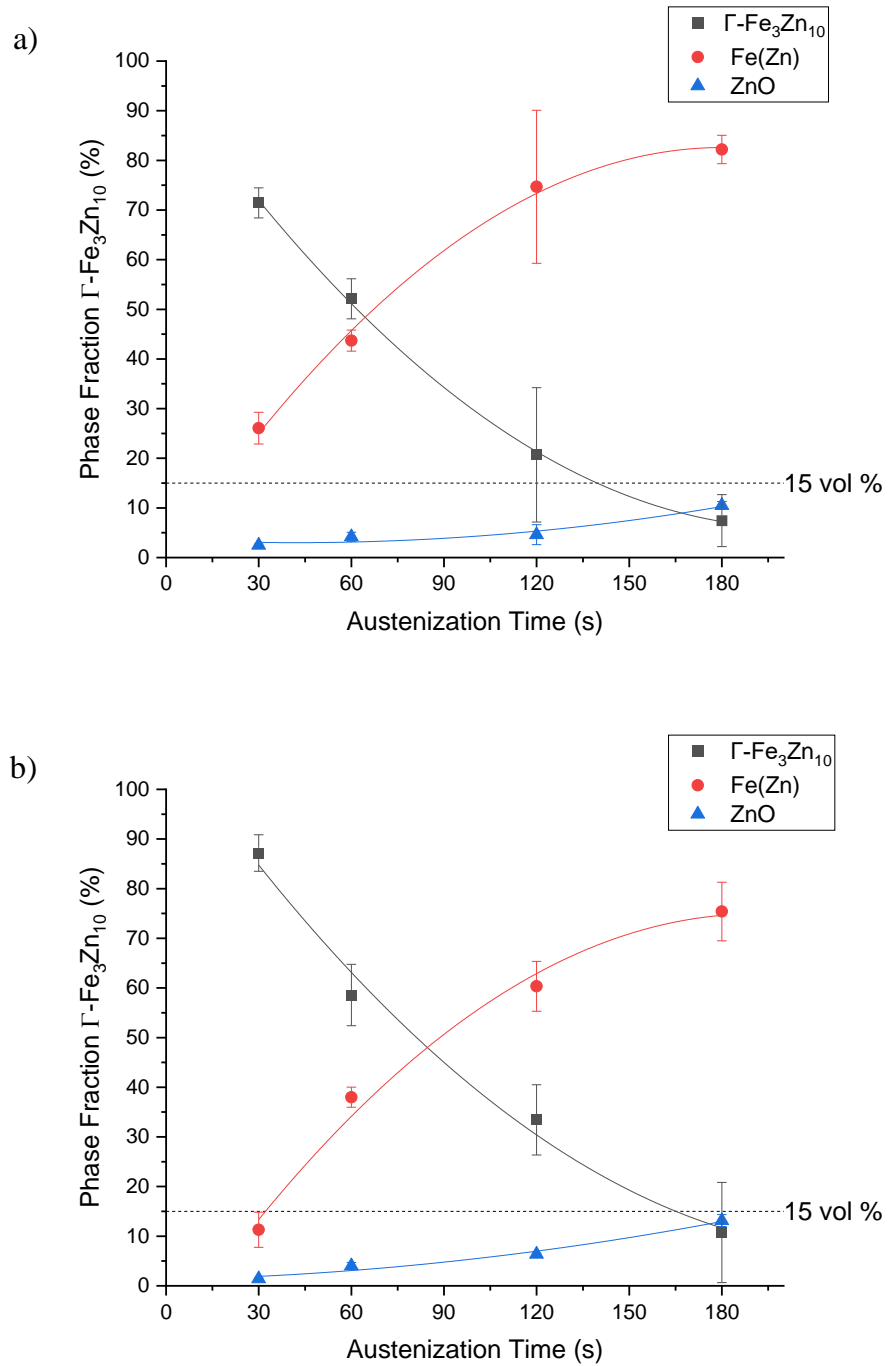Figure 5.4: Phase fractions within the coating on the 2.5%Mn steel plotted against austenization time at the (a) top and (b) wall of the U-shape part. Note that the error bars are 95% confidence intervals of the average reading.

5.3 COATING SURFACE ANALYSIS AFTER DHPF

5.3.1 2%Mn Substrate

Planar SEM images in Figure 5.5 (a) show the top of the part (region 1, Figure 5.1), which has been U-shape hot stamped at 700°C after austenization for 30 s. The coating surface in this area has a nodular morphology, as the surface is covered in a thin layer of oxides. There are small areas, around the corner of the image (Figure 5.5 (a)), where the coating is more compact, indicating that the coating has been partially compressed by the die at the top of the part.

Figure 5.5: Planar SEM images of the coating on 2%Mn steel after austenization for 30 s on the (a) top and (b) wall and after austenization for 180 s on the (c) top and (d) wall of the U-shape part stamped at 700°C.

The wall of the same part (region 4, Figure 5.1), austenitized for 30 s, is shown in Figure 5.5 (b). In this image, the coating is smudged, showing 'die wiping', an effect caused by the friction from the die. As the die slides across the coating, the surface is smoothed, spreading the Γ-Fe_3Zn_{10} phase. This was the reason why XRD had measured a greater phase fraction of Γ-Fe_3Zn_{10} on the part wall when compared to the top, which did not experience die wiping.

The DHPF part coating surface after austenization for 180 s is shown in Figure 5.5 (c) and 5.5 (d) for the top and wall, respectively. The top of the part is covered in oxides (Figure 5.5 (c)). However, they are now larger as the extended time in the furnace has allowed further oxidation. XRD analysis confirms that the amount of ZnO on the surface increased with increasing austenization time (Figure 5.2). Small coating cracks are also visible, which travel through some oxides. The formation of this crack is due to the pressure of the die on the surface, causing the brittle oxides to crack.

On the wall (Figure 5.6 (d)), there is a large area that has been wiped in the same way as the sample austenitized for 30 s. However, the wiping does not completely cover the surface of the part as it did in the former case, and the wiped area is much more compact. After the longer austenization time (Figure 5.6), there is less Γ-Fe_3Zn_{10} in the coating, and greater amount of α-Fe(Zn), which is confirmed by XRD (Figure 5.2). α-Fe(Zn) is a harder phase [68], and therefore doesn't spread to the extent that Γ-Fe_3Zn_{10} does. Creating a more compact die wiped zone on the surface of the galvanized steel austenitized for 180 s.

EDS maps of these areas are shown in Figure 5.6. On the top of the DHPF part, after 30 s of austenization, most of the oxides are Mn and Zn oxides. Mn oxides were not detected in the XRD for any sample, but can appear after long times in the furnace due to surface segregation of Mn [32, 34, 39].

On the top of the U-shape part (Figure 5.6(a)), there is an increased concentration of iron, as indicated by the red colour. The same thing is seen on the die wiped sections of the wall after austenization of 180 s (Figure 5.6 (d)). This shows that on the compact deformed areas, there is an increased amount of α-Fe(Zn) compared to the bulk of the coating. Because of this, there is a decrease in Γ-Fe$_3$Zn$_{10}$ in the same areas. The die wiped areas are small, but occur in patches over the die wiped area. They are not detected in XRD as the resolution is on the mm scale, insufficient for these patches, which are on the μm scale.

Figure 5.6: EDS maps of the coating on 2%Mn steel after austenization for 30 s on the (a) top and (b) wall and after austenization for 180 s on the (c) top and (d) wall of the U-shape part.

5.3.2   2.5% Mn Substrate

Figure 5.7 shows planar secondary electron images of the coating on the 2.5%Mn steel. At the top of the U-shape part (region 1), stamped at 700°C (Figure 5.7 (a)), tight clusters of small oxides cover the surface similar to the coating on the 2%Mn substrate. Coating cracks can be seen in the top middle of the image (highlighted by the red boxes), which likely formed due to the pressure of the die on the relatively brittle surface coating phases. The wall of the part (Figure 5.7 (b), region 4) is again smudged due to die friction wiping the surface. A few small clusters of oxides can be seen on the surface.
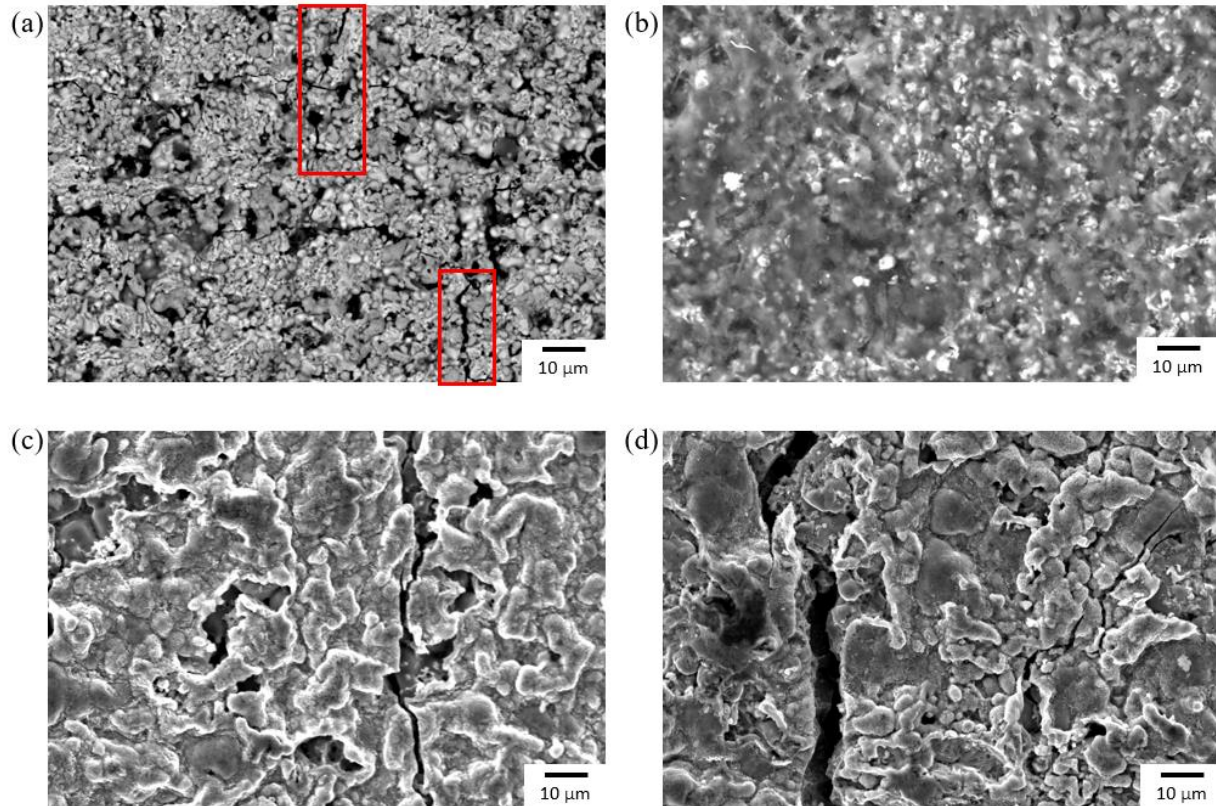
Figure 5.7: Planar SEM images of the coating on 2.5%Mn steel after austenization for 30 s on the (a) top (region 1) and (b) wall (region 4) and after austenization for 180 s on the (c) top and (d) wall of the U-shape part.

The coating surface after austenization for 180 s and U-shape DHPF at 700°C on the 2.5%Mn steel is shown in Figure 5.7 (c) at the top, and 5.7 (d) at the wall. The oxides on the surface in both regions are dense and compact. There are coating cracks present on both the top and wall of the part, with the larger cracks appearing at the wall of the part. The wall does not appear as obviously smoothed by the die friction as it did on the 2%Mn steel (Figure 5.5 (d)) . This is due to the decreased amount of Γ-Fe_3Zn_{10} in the coating of the 2.5%Mn steel compared to the coating of the 2%Mn steel (Figure 5.4 vs. Figure 5.2). As stated earlier, α-Fe(Zn) is a harder phase, and does not spread as easily as Γ-Fe_3Zn_{10}.

Figure 5.8 (c) and (d) present the EDS maps of the top and wall of the part austenitized for 180 s. On the top of the DHPF part (region 1), α-Fe(Zn) can be seen in the crack, showing that the crack passes through the surface layer of Γ-Fe_3Zn_{10} and into the coating below. The same can be seen at the wall of the part (Figure 5.8(d)). In addition, there are several areas on the coating where the surface oxides and Zn-rich phases are missing from the surface, as indicated by the red areas. EDS point analyses, whose locations are shown in Figure 5.9 and the results of which are shown in Table 5.2, indicate a composition of 56 wt% Fe, 40 wt% Zn and 3 wt% Mn when averaged between spectra 1-3 (i.e. the red areas). This is a high Zn content α-Fe(Zn) [29]. These spectra prove that the red regions in the EDS maps are α-Fe(Zn), rather than exposed substrate. Spectra 4-6 are mostly Mn-Zn oxides, which contain very little Fe. Spectra 7-9 are Zn oxides on the surface. This is interesting as Mn-Zn oxides were not seen in XRD analysis of the surface, but have been found in literature [4, 39].
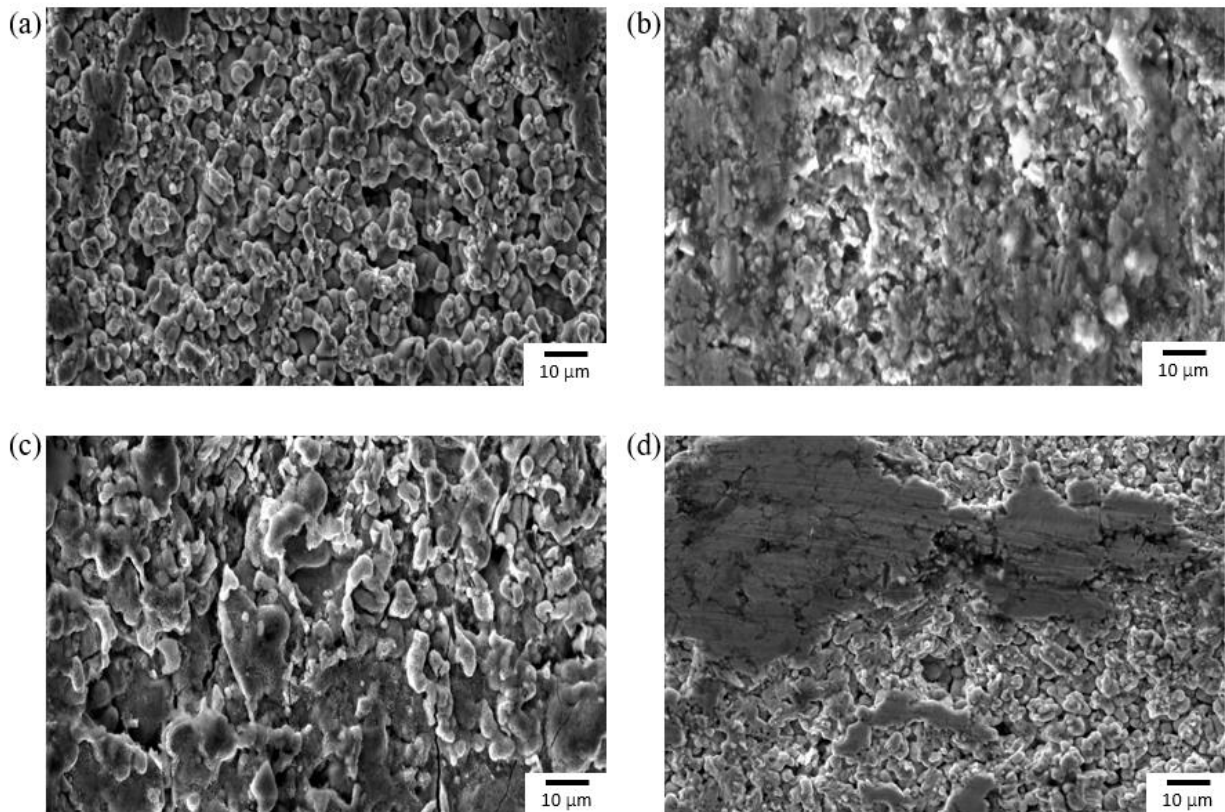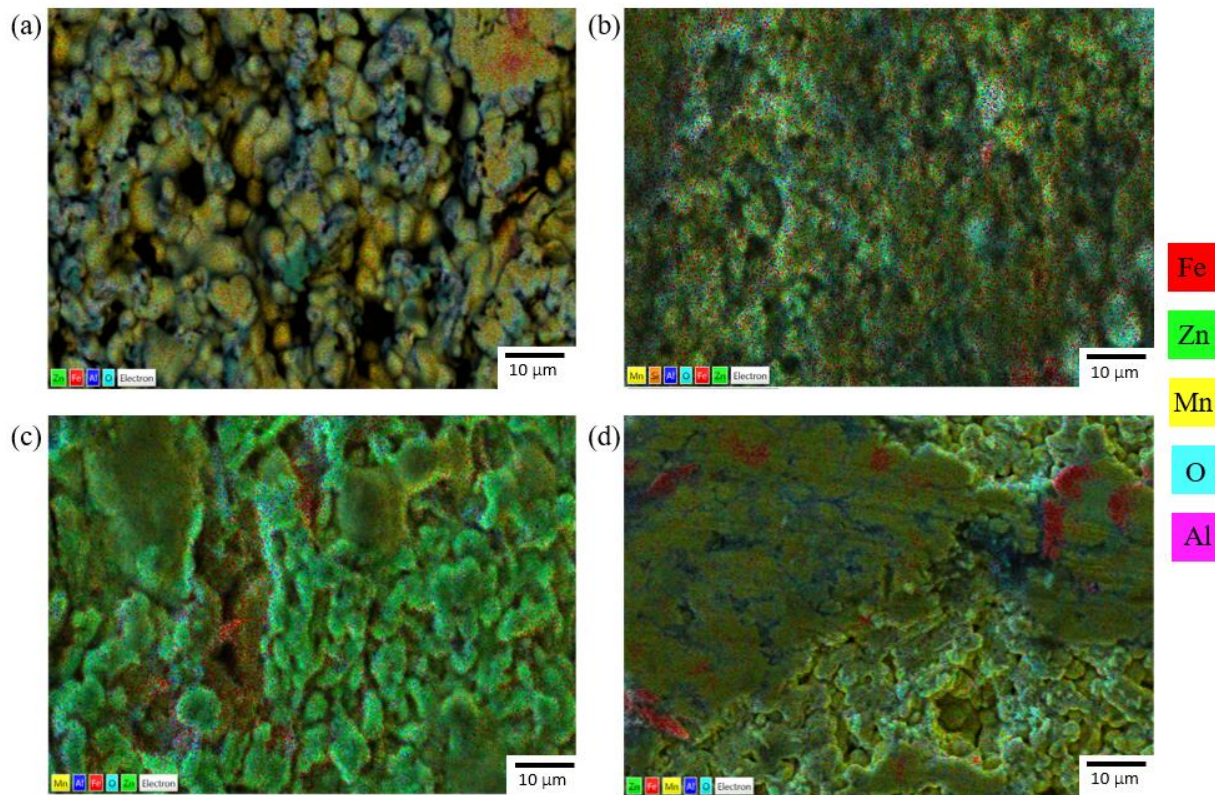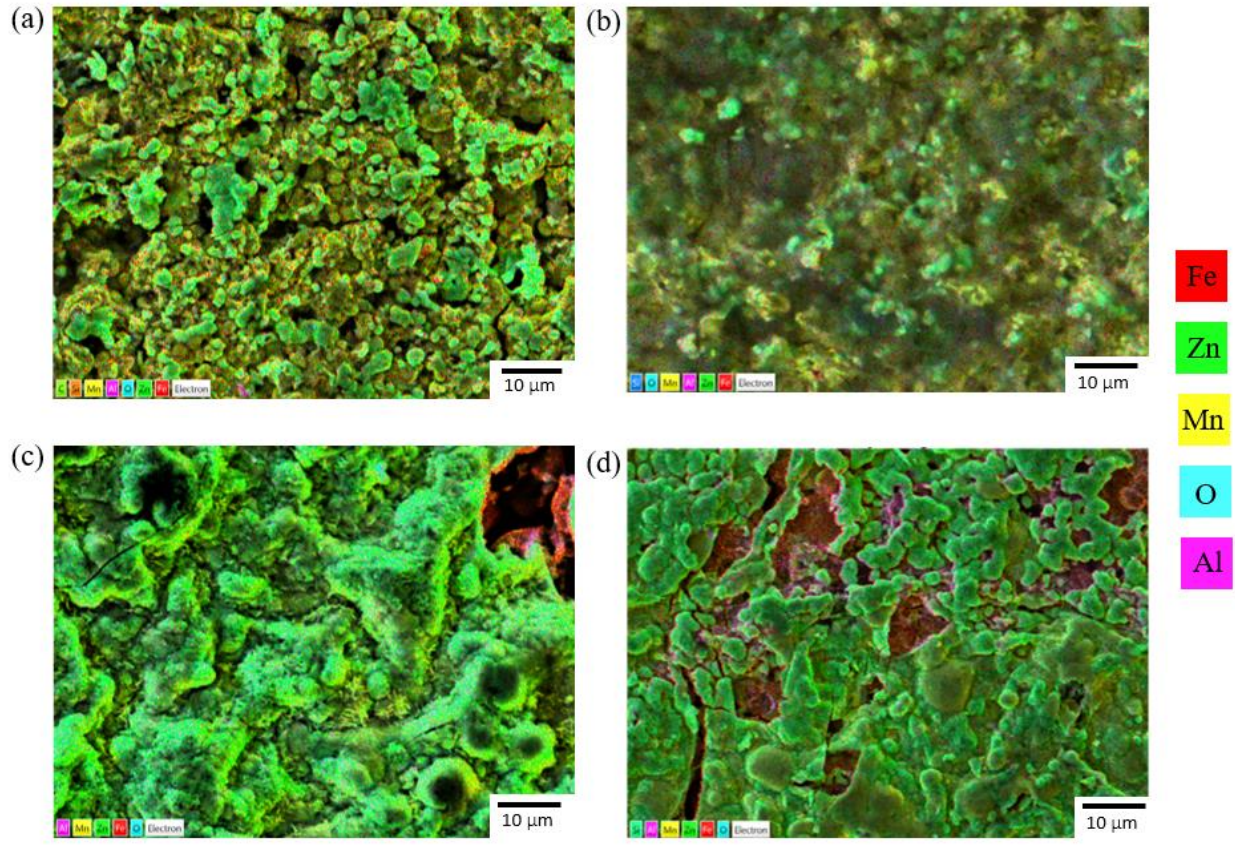
Figure 5.8: EDS maps of the coating on 2.5%Mn steel after austenization for 30 s on the (a) top and (b) wall and after austenization for 180 s on the (c) top and (d) wall of the U-shape part.

Figure 5.9: EDS map of wall of galvanized DHPF 2.5%Mn austenitized for 180 s.

Table 5.2: Table of analyses of points in Figure 5.9. Average wt% between spectra with 95% CI.

Spectrum #	Fe	Zn	Mn	O
1-3	56 ± 4	40 ± 2	3 ± 1	1 ± 1
4-6	3 ± 1	34 ± 5	49 ± 4	14 ± 10
7-9	5 ± 1	81 ± 8	3 ± 2	11 ± 7

5.4 CROSS-SECTIONAL IMAGING OF THE DHPF COATING

Figure 5.10 shows the cross-sectional microstructure of the coating on the 2%Mn substrate for all experimental austenization times, taken in BSE imaging mode. Images shown are taken from the top, wall and outer corner of a U-shape part, which has been stamped at 700°C. In BSE, elements that have a higher atomic mass appear lighter. As Γ-Fe_3Zn_{10} is a Zn-rich phase and has the highest average atomic mass versus α-Fe(Zn) and Fe, it appears as the lightest grey. The medium grey phase is α-Fe(Zn), and the darkest grey is the steel substrate.

In all regions of the part, it is evident that the amount of Γ-Fe_3Zn_{10} decreases with an increasing austenization time, consistent with the XRD results in Figure 5.2 and Figure 5.4. This phase appears predominantly at the surface of the coating, which, as previously stated, is the area in contact with the die and is more prone to die wiping. After austenization for 180 s only a very thin surface layer of Γ-Fe_3Zn_{10} can be seen (Figure 5.10). XRD analysis of the coating measured an average of 40 vol% Γ-Fe_3Zn_{10} at the part top, and 53 vol% Γ-Fe_3Zn_{10} at the wall. These two methods show significantly different coating compositions.
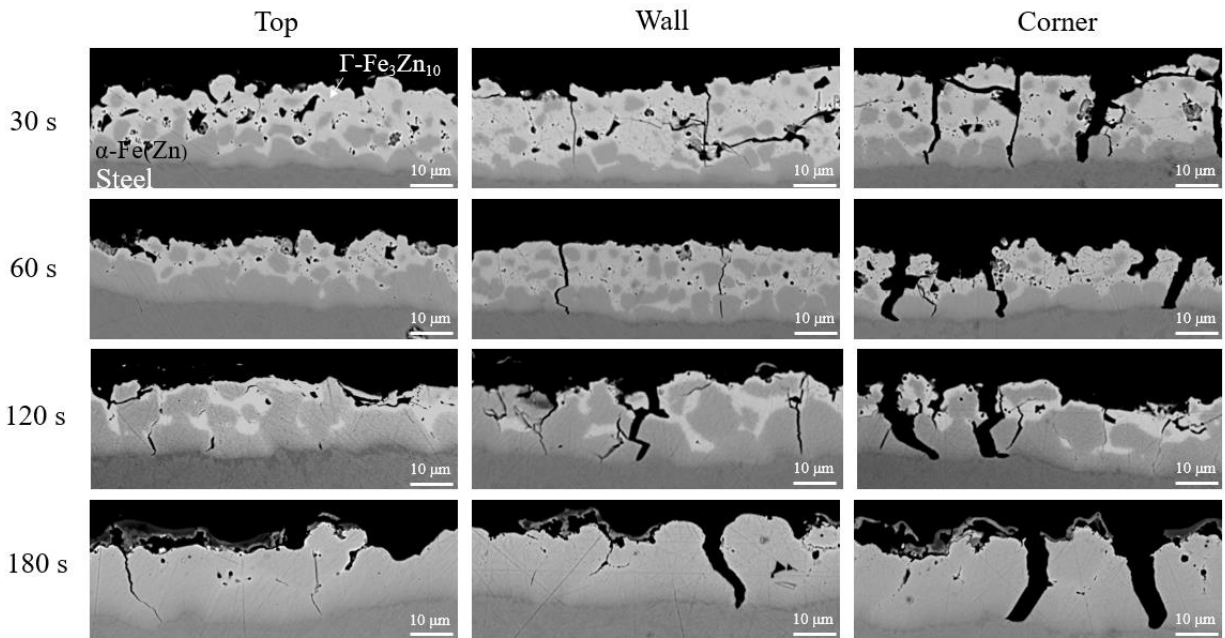
Figure 5.10: BSE coating cross-sectional images for select areas on the 2%Mn U-shape part for various austenization times.

The coating cracks that were seen in the planar images at long austenization times (Figures 5.5-5.8) also appear in the coating cross-section (Figure 5.10), particularly in the wall (region 4, Figure 5.1) and corner (region 2, Figure 5.1) of the part. At the corner, this is due to the tensile deformation of the substrate and coating to create the curve in the U-shape part. The intermetallic coating phases are more brittle than the substrate and, therefore, crack due to the

deformation. On the wall, the cracks form as the die slides over the surface of the part, friction between the die and the coating surface try to move the coating, but the steel substrate underneath does not move. Small cracks are created because of these opposing motions. They also appear at the top of the part at longer austenization times, particularly in the α-Fe(Zn).

These coating cracks have propagated through the entire coating, travelling along α-Fe(Zn) grain boundaries and arresting at the coating/substrate interface. Similar coating cracks along α-Fe(Zn) grain boundaries have been seen in numerous previous works on galvanized DHPF steel [4, 40, 57]. It is expected that the throwing power of the cathodic protection will be able to prevent corrosion in these cases. However, the cracks become larger and more numerous with an increasing austenization time. This combined with the decreasing amount of Γ-Fe_3Zn_{10} indicate that there will be less corrosion protection from the coating in these cases.

Cross-sectional images of the DHPF coating on the 2.5%Mn substrate is shown in Figure 5.11. The coating is similar to that on the 2%Mn substrate, and shares many of the same characteristics. For instance, there is a decrease in Γ-Fe_3Zn_{10} with increasing austenization time, which is consistent with the XRD results shown in Figure 5.4. In addition, the same coating cracks can be seen in the coating starting at the corner austenitized for 30 s. It is still expected that the throwing power of cathodic protection will be able to prevent substrate corrosion despite this.
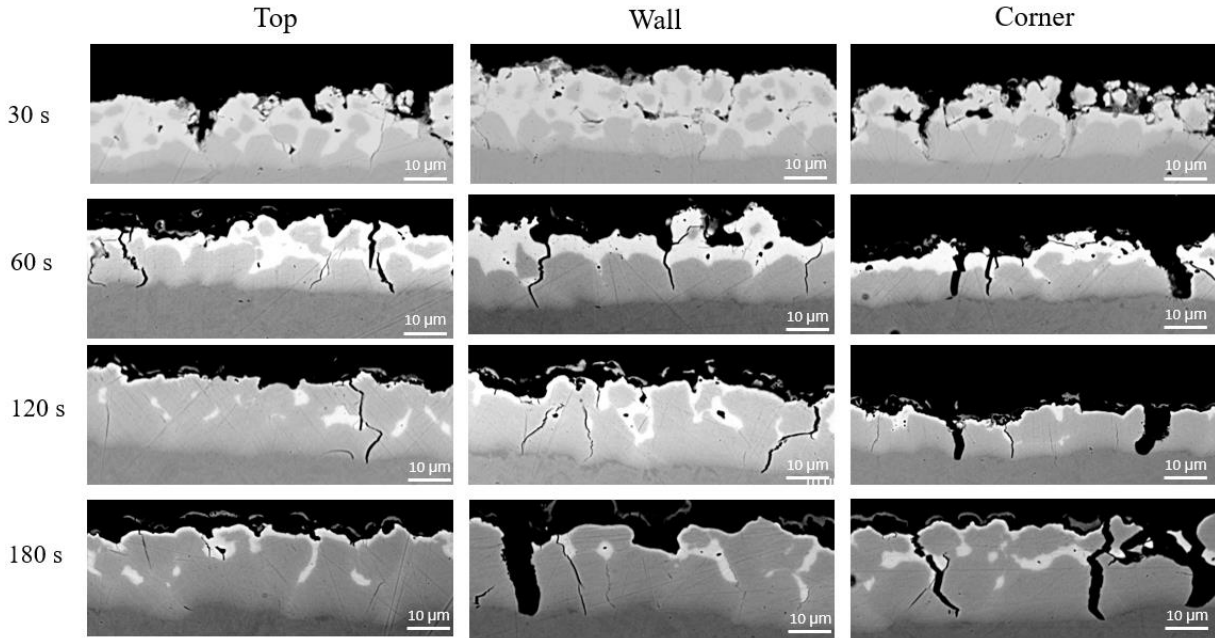
Figure 5.11: BSE coating cross-sectional images for select areas on the 2.5%Mn U-shape part for various austenization times.

5.5 EFFECT OF DHPF ON DRIVING FORCE FOR CATHODIC PROTECTION

The driving force for cathodic protection is described as the difference in E_{corr} or corrosion potential between the steel (cathode) and the Fe-Zn coating phases (anode).

$$\Delta E_{corr} = E_{steel} - E_{coating} \tag{1}$$

In the subsequent text, the E_{corr} is measured using potentiodynamic polarization curves. The results of the applicable potentiodynamic polarization scans are shown in Figure 5.12 for both the ungalvanized steel substrates, as well as for coatings that consist of only Γ-Fe$_3$Zn$_{10}$ and α-Fe(Zn) produced by flat die quenching.
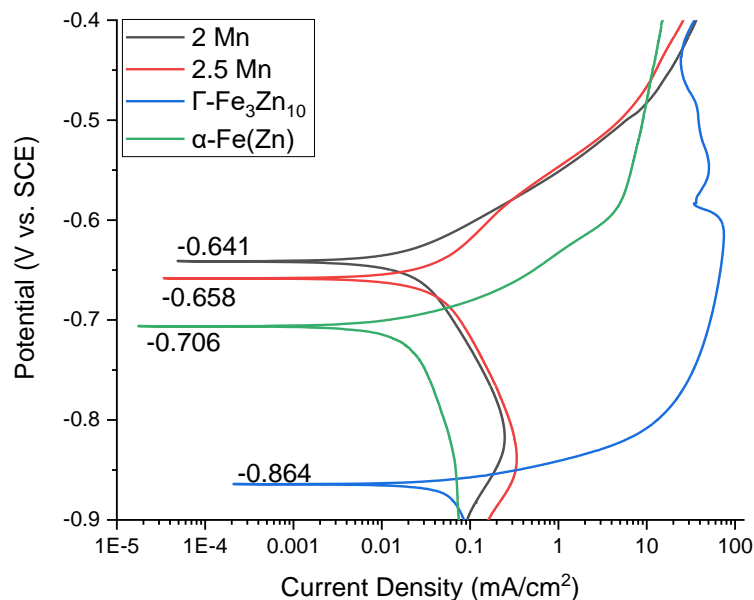
Figure 5.12: Potentiodynamic polarization for the uncoated 2%Mn and 2.5% steels, and coatings consisting of only αFe(Zn) and Γ-Fe$_3$Zn$_{10}$. Electrolyte solution: 100 g ZnSO$_4$•7H$_2$O, 200g NaCl, 1000 mL DI Water.

The E$_{corr}$ of the 2%Mn uncoated steel was found to be –641 mV vs. SCE. That of the intermetallic phases Γ-Fe$_3$Zn$_{10}$ and α-Fe(Zn) were determined to be –864 mV and –706 mV, respectively, as shown in Figure 5.12. This means that ΔE $_{2\%Mn – α\text{-}Fe(Zn)}$ = 65 mV and ΔE $_{2\%Mn\,\text{-}\,Γ\text{-}Fe3Zn10}$ = 223 mV, thus showing a significantly greater driving for cathodic protection provided by Γ-Fe$_3$Zn$_{10}$. However, a guideline for providing robust cathodic protection is a ΔE ≥ 250 mV [38]. This guideline is not met for either intermetallic phase in the coating. However, ΔE $_{2\%Mn\,\text{-}\,Γ\text{-}Fe3Zn10}$ is much closer to the guideline than ΔE $_{2\%Mn – α\text{-}Fe(Zn)}$. Therefore, in this work, only Γ-Fe$_3$Zn$_{10}$ is considered as the phase providing robust cathodic protection to the steel. The main purpose of α-Fe(Zn) is to provide barrier protection, which may prevent the corrosion of the steel, but is considered insufficient for the purpose of providing a coating that provides robust

cathodic protection to the underlying steel. However, as there is a positive difference in $\Delta E_{2\%Mn - \alpha\text{-}Fe(Zn)}$ on both steel substrates, α-Fe(Zn), will still preferentially corrode when coupled to the bare steel.

From Figure 5.12, it is also seen that the E_{corr} of the 2.5%Mn uncoated steel was found to be –658 mV vs. SCE, which is slightly lower that on the 2%Mn steel. This is due to the increased amount of Mn in the steel, which is electrochemically active and reduces the E_{corr}. From the above equation (Eq. 5.1) and the E_{corr} determined by potentiodynamic polarizations (Figure 5.12), $\Delta E_{2.5\%Mn - \alpha\text{-}Fe(Zn)} = 48$ mV and $\Delta E_{2.5\%Mn - \Gamma\text{-}Fe3Zn10} = 206$ mV. The driving force for cathodic protection provided by the Zn-based coating is lowered slightly on the 2.5%Mn substrate than on the 2%Mn substrate. However, the $\Delta E_{\Gamma\text{-}Fe3Zn10}$ is still much higher than $\Delta E_{\alpha\text{-}Fe(Zn)}$, and it is concluded that only $\Gamma\text{-}Fe_3Zn_{10}$ will be able to provide robust cathodic protection to the bare steel.

Further potentiodynamic polarization curves of the top, wall, and corner of the U-shape DHPF galvanized 2%Mn steel is shown in Figure 5.13. After austenization of 30 s (Figure 5.13 (a)), the $E_{corr} = -851$ mV for all regions is the same, indicating the driving force for cathodic protection is the same for all regions across the U-shape part. The E_{corr} remains consistent at for austenization times of 60 s and 120 s (Figure 5.13 (b) and (c)), and $E_{corr} = -853$ mV and $E_{corr} = -859$ mV, respectively. In all of these potentiodynamic polarization scans, a nose is also seen at approximately –0.7 mV (SCE), and a second broader nose at –0.5 mV (SCE). These are the dissolution of α-Fe(Zn) and the steel substrate acting as a secondary anodic region.

However, after 180 s (Figure 5.13 (d)), there is a difference in E_{corr} between the top of the part ($E_{corr} = -866$ mV), and the corner and wall ($E_{corr} = -845$ mV). This difference decreases the ΔE between the mixed potential and the bare steel, indicating that there is less cathodic

protection provided at the corner deformed in tension, and the wall of the part compared to the top. This difference is only about 20 mV, which is small and may not have a great effect on the overall corrosion rate of the bare steel when galvanically coupled to the coating at either location of the part. The way this the regions are split is in opposition to what was determined by Raja et al. who reported that increased deformation of a galvannealed part results in a decrease in E_{corr} [76].

Overall, the E_{corr} decreased slightly with increasing austenization time, which is interesting as one would expect it to increase as the phase fraction of Zn-rich phases, and the Zn content of α-Fe(Zn) is lowered. The discrepancy is because the E_{corr} is more dependant on the surface fraction of the coating phases because corrosion is a surface phenomenon. This is the reason why the areas affected most by the die (tensile cracks in the corner and die wiping in the wall) have a higher E_{corr}. However, this difference is only marginally significant, and conclusions on the cathodic protection provided by the coating cannot be drawn based solely on the potentiodynamic polarizations.

a)

b)
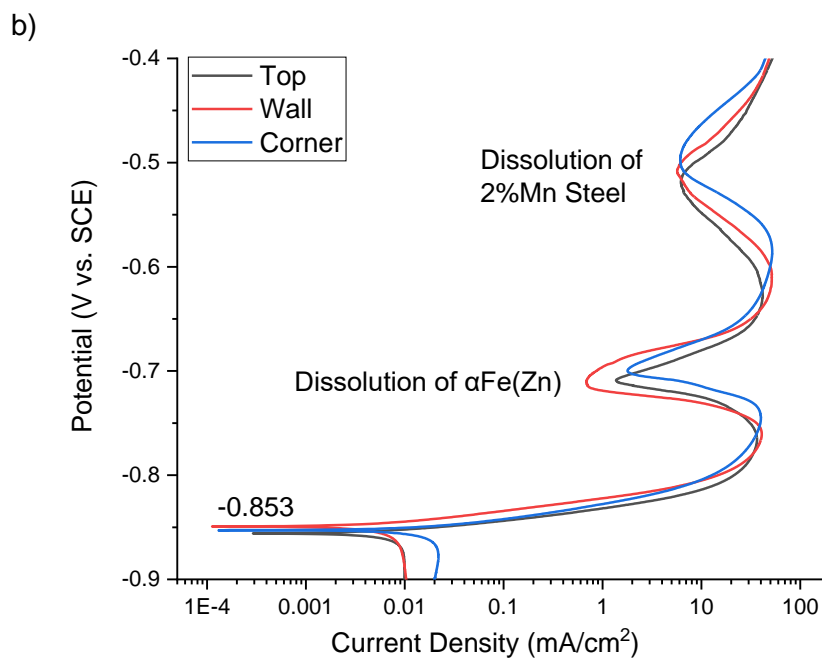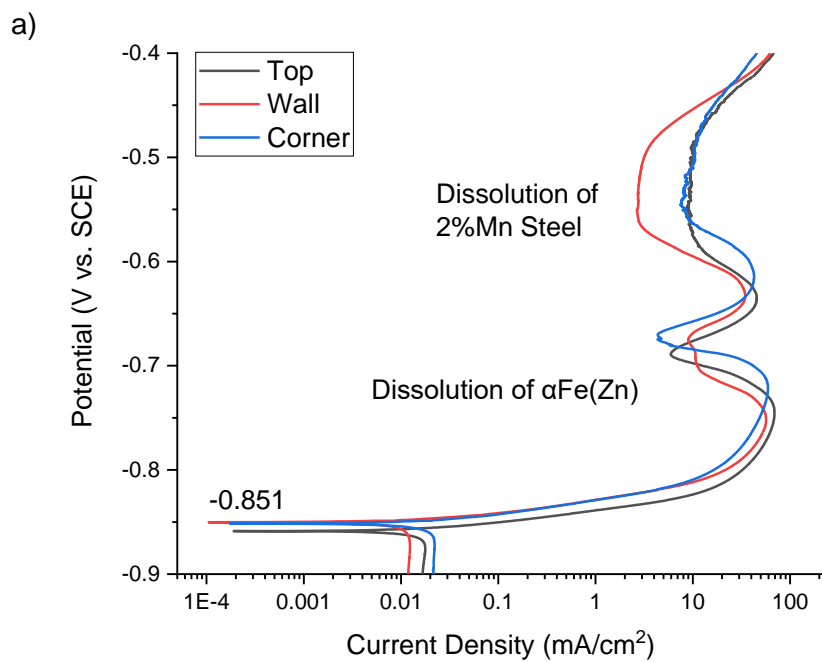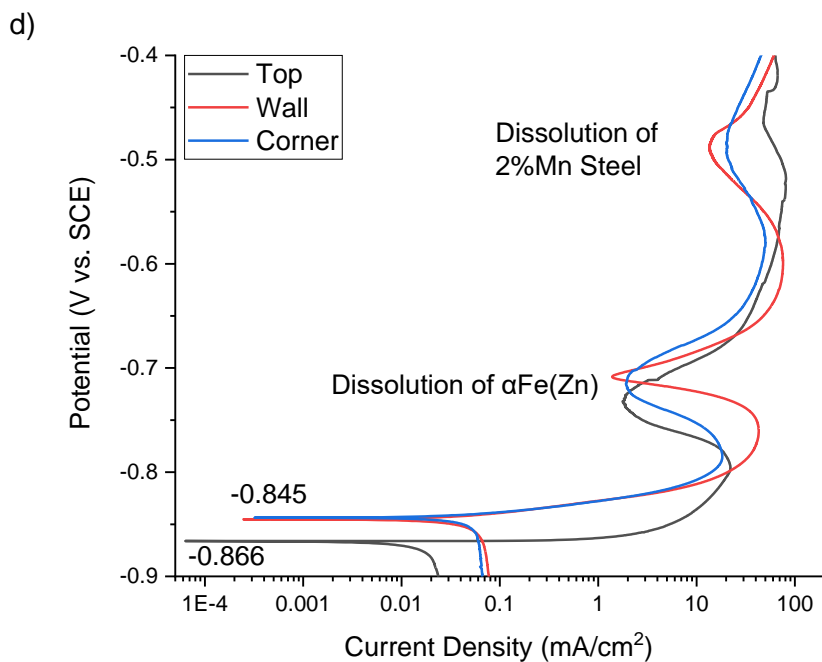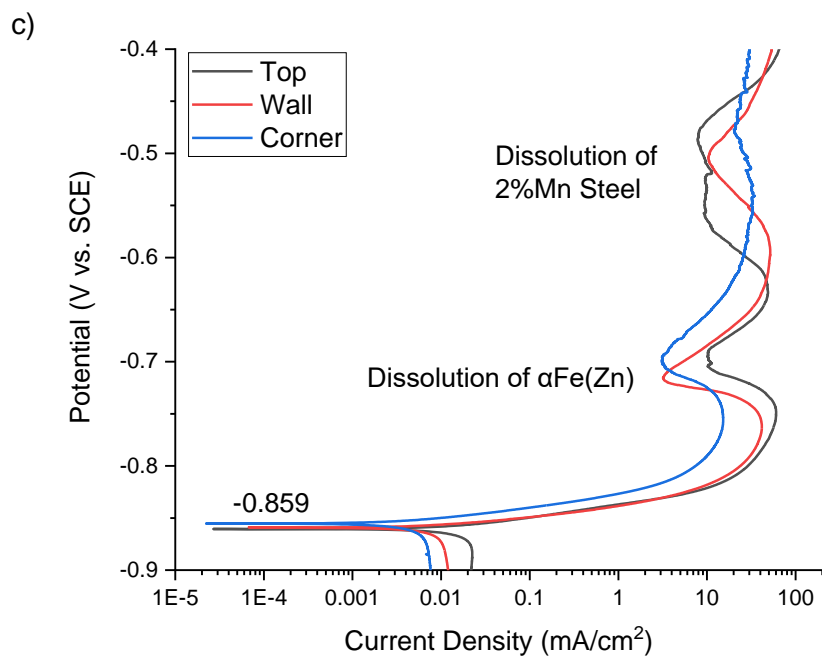
Figure 5.13: Potentiodynamic polarization curves of the coated 2%Mn steel after austenization for (a) 30 s (b) 60 s (c) 120 s (d)180 s and DHPF shown for selected areas on the U-shaped part. Electrolyte solution: 100 g ZnSO$_4$•7H$_2$O, 200g NaCl, 1000 mL DI Water.

The potentiodynamic polarization curves for the galvanized 2.5%Mn steel, which were DHPF at 700°C, are shown in Figure 5.14. After austenization for 30 s and 60 s (Figure 5.14 (a) and (b)), there is no significant difference in E_{corr} between the regions on the U-shaped part.

Similar to the 2%Mn steel, a split in E_{corr} occurs between the regions on the U-shape part, this time after austenization for 120 s. At the corner (blue curve in Figure 5.14 (c)), $E_{corr} = -844$ mV, and at the top and wall where $E_{corr} = -858$. This difference is again small, only 14 mV. After austenization for 180 s, it is now the wall (red curve in Figure 5.14 (d)) which has the higher $E_{corr} = -844$ mV compared to the wall at -863 mV.

a)

b)

c)

d)
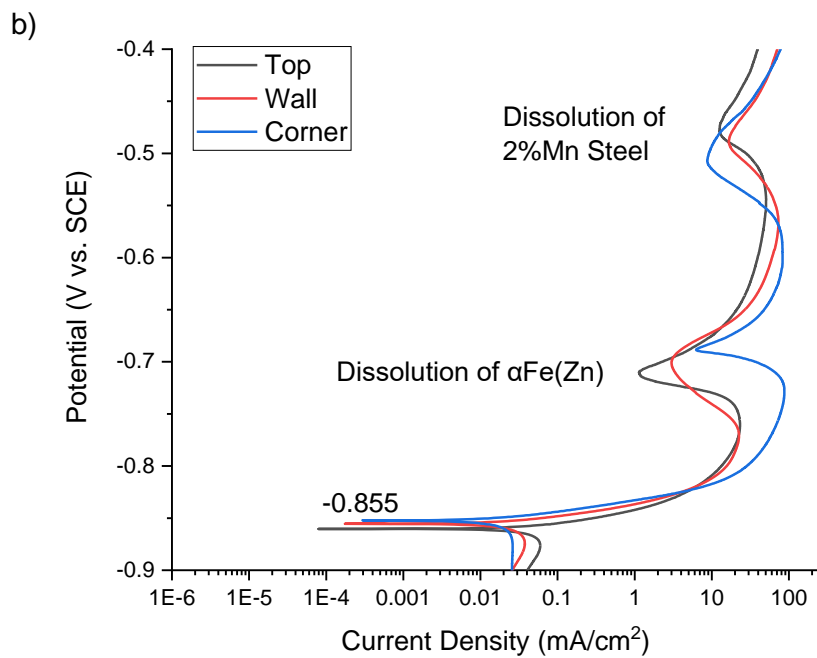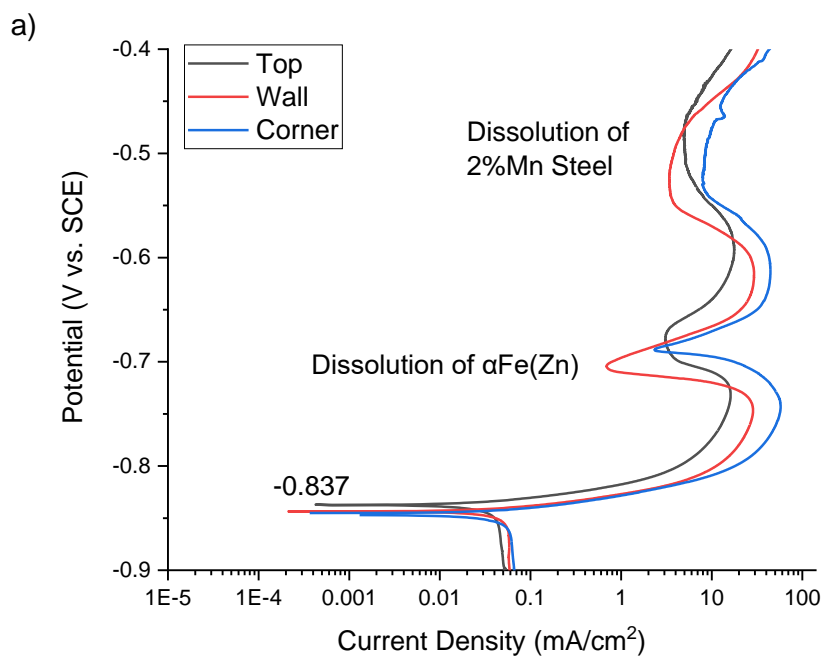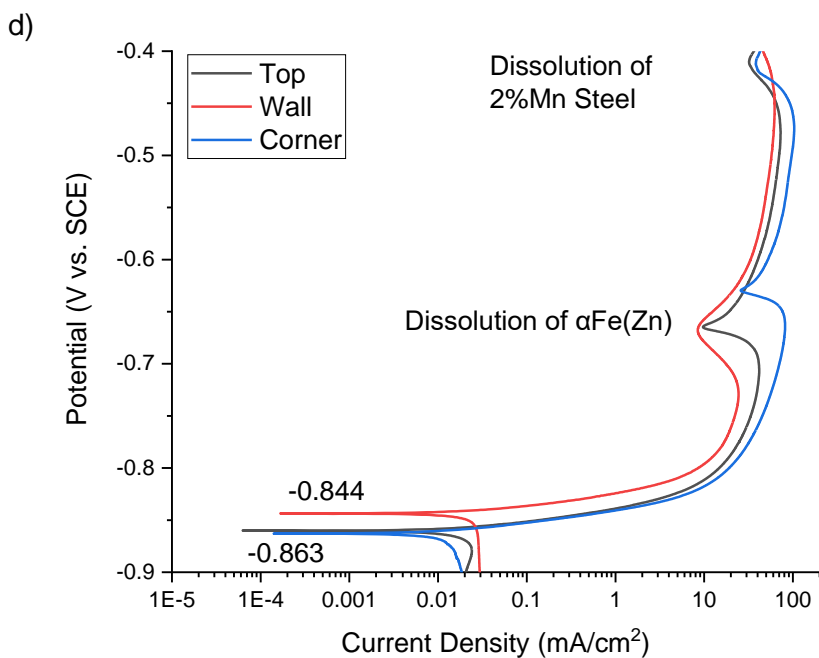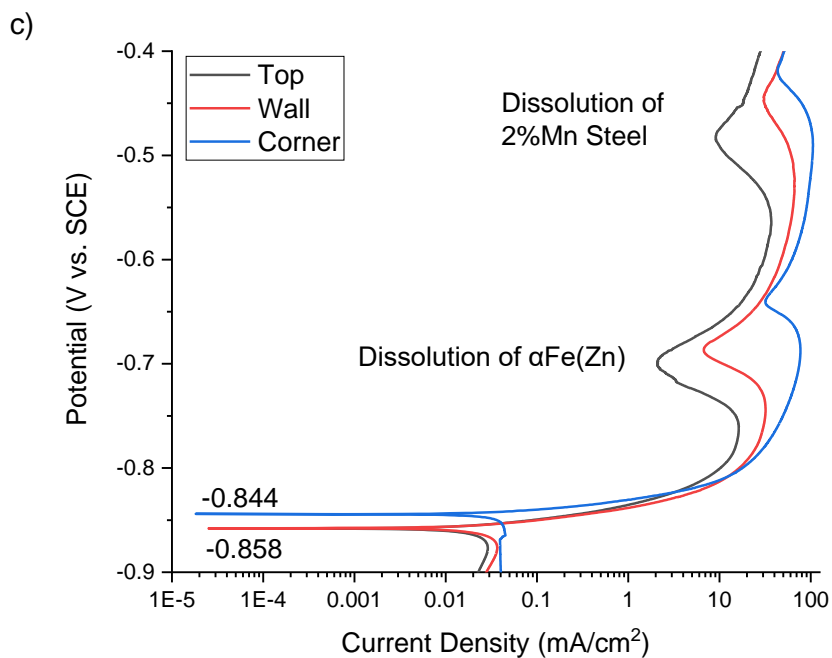
Figure 5.14: Potentiodynamic polarization curves of the coated 2.5%Mn steel after austenization

for (a) 30 s (b) 60 s (c) 120 s (d)180 s and DHPF shown for selected areas on the U-shaped part.

Electrolyte solution: 100 g $ZnSO_4 \cdot 7H_2O$, 200g NaCl, 1000 mL DI Water.

Both Zn-coated DHPF steel substrates exhibited the same general trend: a decreasing E_{corr} with increasing austenization time. In addition, at longer austenization times, there was a difference in E_{corr} of approximately 20 mV between the regions significantly affected by die wiping (wall and corner) and that which was not (top). The E_{corr} increased at the wall and corner, which can be explained as a higher mixed potential due to exposed α-FeZn, the Fe-rich intermetallic phase. Evidence of this is in the coating cracks found in cross-sectional images (Figures 5.10 and 5.11), as well as exposed α-FeZn in surface imaging (Figures 5.5 and 5.7).

5.6   EFFECT OF DHPF ON THE DISSOLUTION KINETICS OF ZN-BASED COATING

Galvanostatic polarizations were used to determine the dissolution kinetics of the intermetallic phases in the coating and the galvanized steel. A constant current density of +10 mA/cm^2 was supplied by the galvanostat to accelerate corrosion of the coating.

Figure 5.15 shows galvanostatic scans at the top, wall, and corner of the U-shape DHPF part after austenization for 30 s at 890°C. The electrochemical potential vs. time plot shows three potential arrest plateaus. The first, which occurs at approximately –800mV, is the dissolution of Γ-Fe$_3$Zn$_{10}$, which occurs preferentially compared to α-Fe(Zn) and the steel substrate, as shown by the potentiodynamic polarizations in Figure 5.12 The second plateau is around –660 mV and is the dissolution of α-Fe(Zn), where robust cathodic protection is no longer provided. However, α-Fe(Zn) will still corrode preferentially to the steel, as well as provide barrier protection preventing corrosion on the substrate. The final plateau is the dissolution of the steel substrate at –480mV. At this point, the coating is no longer able to provide any corrosion resistance.

As can be seen in Figure 5.15, the complete dissolution of Γ-Fe$_3$Zn$_{10}$ occurs sooner at the corner of the part, followed by the wall 600 s later, and finally the top 200 s after this. From these results, it can be concluded that the coating provides less robust cathodic protection to the

corner of the part under these experimental conditions. This is due to the presence of the coating cracks, which can be seen in the cross-sectional imaging (Figure 5.10). The presence of these cracks allows additional exposed surface area as the electrolyte solution is able to enter into them. As a result, the dissolution of bare steel at the corner of the part occurs first, indicating that the coating will not provide cathodic protection for as long in this area of the DHPF part, leaving the corner more susceptible to corrosion.
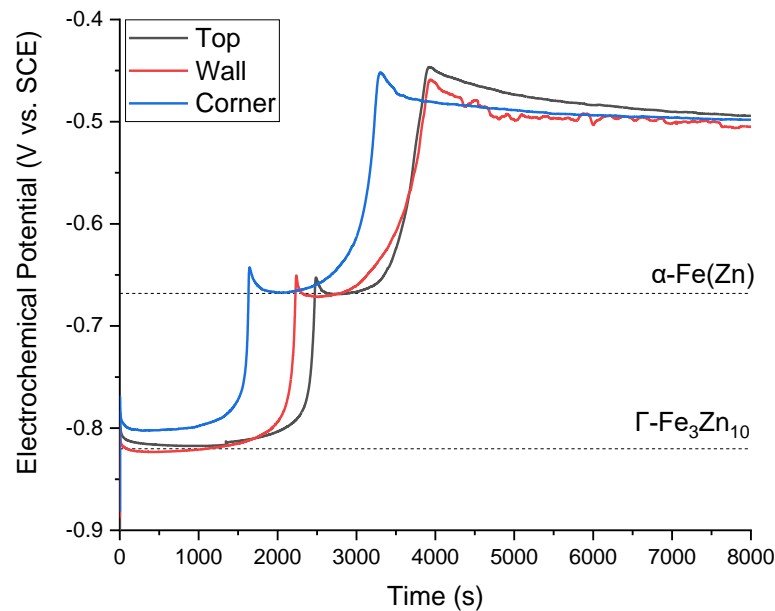
Figure 5.15: Galvanostatic scan of coated 2%Mn steel austenitized for 30 s and DHPF at 700°C.

Galvanostatic scans for the 2%Mn DHPF parts austenization for 60 s and 120 s are shown in Figures 5.16 and 5.17, respectively. The Γ-Fe$_3$Zn$_{10}$ plateau has decreased with the increased austenization time, as is expected since the XRD results (Figure 5.2) have shown a decrease in coating Γ-Fe$_3$Zn$_{10}$ for these sections of the U-channel part. It can be seen that the Γ-Fe$_3$Zn$_{10}$ plateau has decreased in size, as expected since the XRD analysis of the coating shows

less Γ-Fe$_3$Zn$_{10}$ is present. Therefore, the complete dissolution of this phase occurs sooner with the increased austenization times.

In Figure 5.16, the end of the Γ-Fe$_3$Zn$_{10}$ plateau, and the point where the coating is no longer preventing dissolution of the bare steel, occurs first at the corner and wall of the part. At the wall of the part, the increased removal of Γ-Fe$_3$Zn$_{10}$ from the coated areas (Figure 5.6), is now beginning to have a negative impact on the corrosion behaviour of the wall region, explaining why this plateau is shorter. At the corner, coating cracks appear worse after 60 s than 120 s, as seen in cross-sectional SEM in Figure 5.10, indicating that the Γ-Fe$_3$Zn$_{10}$ is unable to protect this area despite the fact there is more of this phase after the shorter austenization time (Figure 5.2).
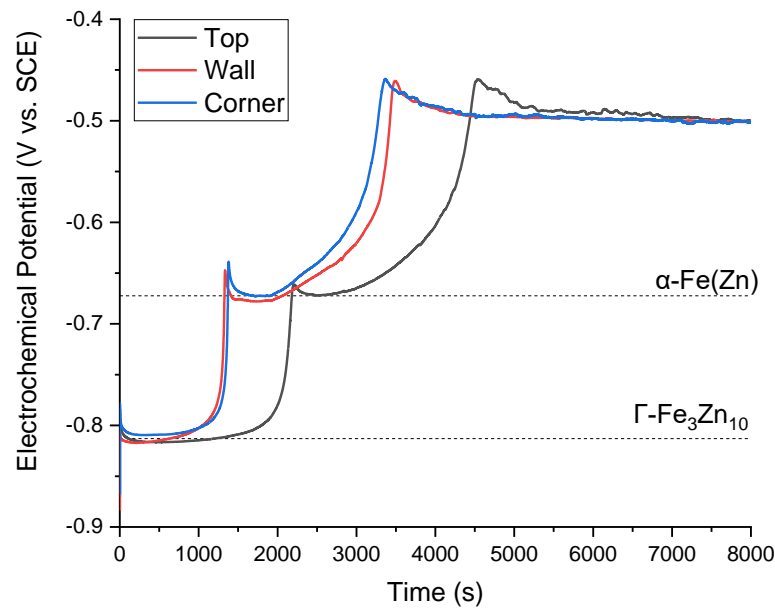
Figure 5.16: Galvanostatic scan of coated 2%Mn steel austenitized for 60 s and DHPF at 700°C.
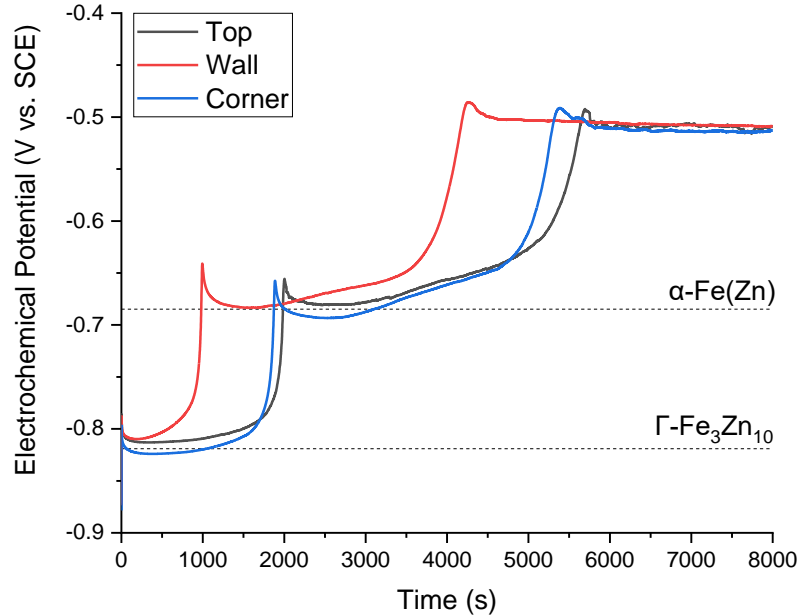
Figure 5.17: Galvanostatic scan of coated 2%Mn steel austenitized for 120 s and DHPF at 700°C.

Figure 5.18 shows the galvanostatic scans for the 2%Mn steel after austenization for 180 s and DHPF at 700°C. It is clear that there is significantly less Γ-Fe$_3$Zn$_{10}$ in the coating with the increased austenization time. This result is consistent with what is seen in the cross-sectional images (Figure 5.10), where only a very thin surface layer of this phase can be seen, as well as XRD analysis of the top and wall of the DHPF part (Figure 5.2). At the corner and wall of the part, there is no Γ-Fe$_3$Zn$_{10}$ plateau, although the open circuit potential, which was completed before this indicated that Γ-Fe$_3$Zn$_{10}$ was present. This indicates that there is not enough of this phase in the coating to provide robust cathodic protection to the steel.
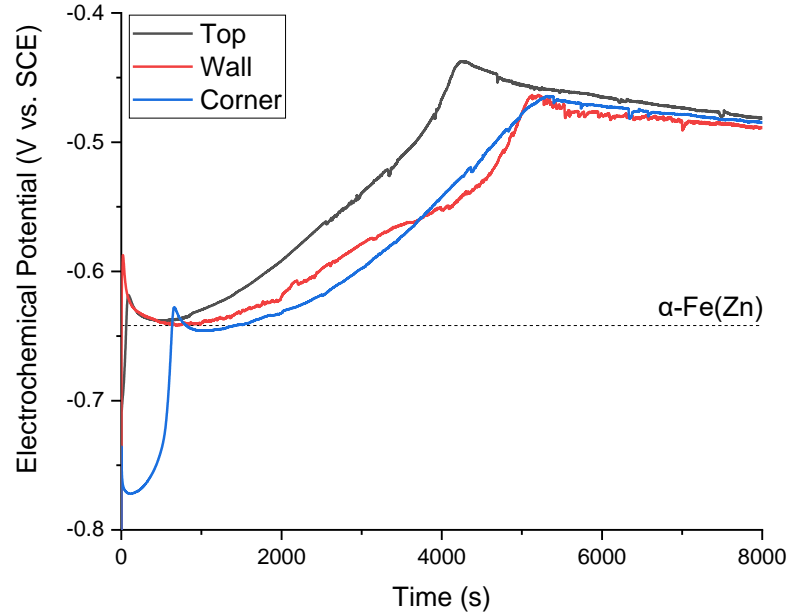
Figure 5.18:Galvanostatic scan of coated 2%Mn Steel austenitized for 180 s and DHPF at 700°C.

The galvanostatic scans on the Zn-coated 2.5%Mn DHPF parts are shown in Figures 5.19-5.22. As the austenization time increases, the length of time Γ-Fe_3Zn_{10} is present decreases due to the decrease in the amount of this phase in the coating, as can be seen in the XRD analysis (Figure 5.3), and the cross-sectional imaging (Figure 5.11), which has been discussed in previous sections. In each case, the complete dissolution of Γ-Fe_3Zn_{10} occurs in the order wall > top > corner. However, the final plateau is reached on the top before the corner.
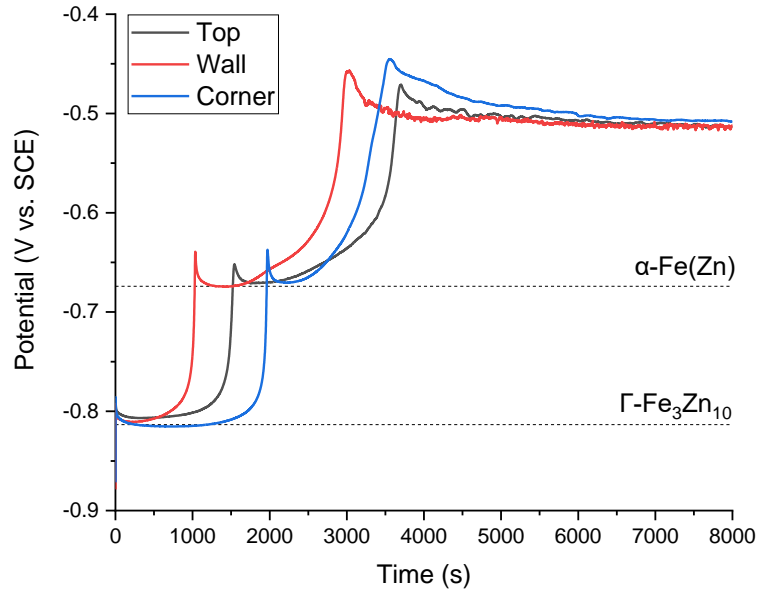
Figure 5.19: Galvanostatic scans of select regions of the Zn coated 2.5%Mn Steel austenitized for 30 s and U-Shape DHPF at 700°C.
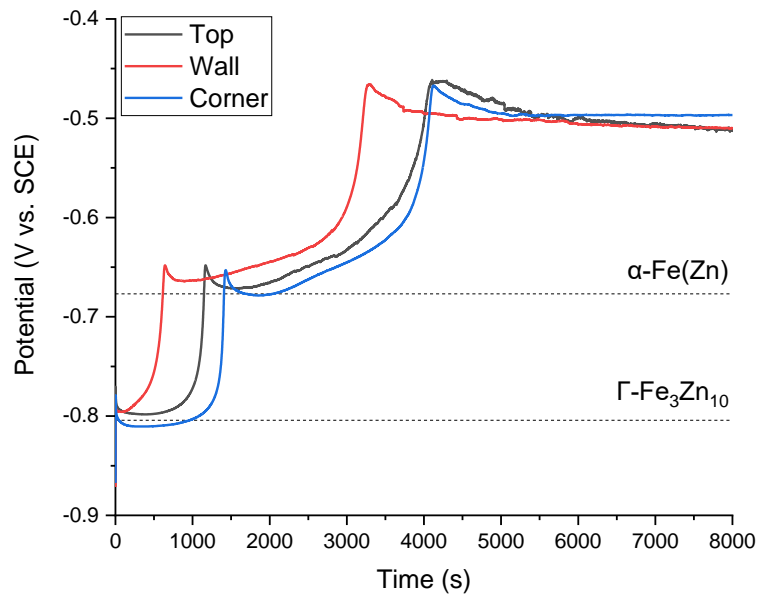
Figure 5.20: Galvanostatic scans of select regions of the Zn coated 2.5%Mn Steel austenitized for 60 s and U-Shape DHPF at 700°C.
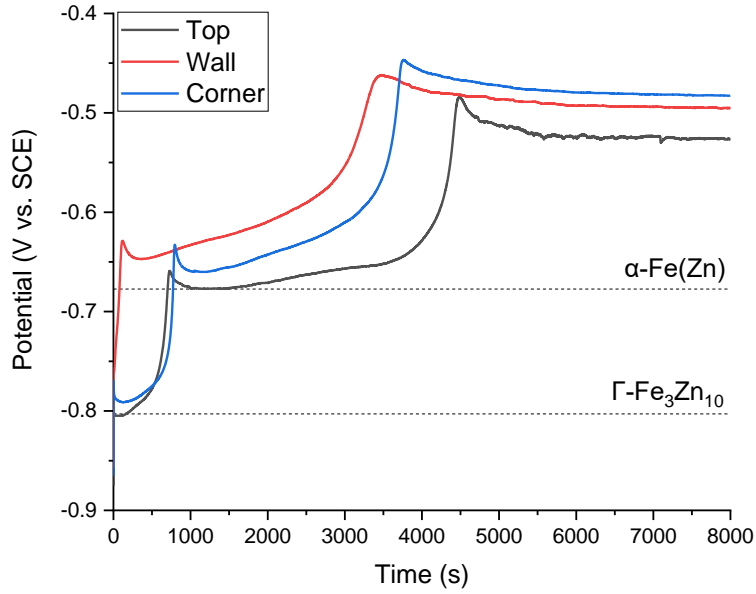
Figure 5.21: Galvanostatic scans of select regions of the Zn coated 2.5%Mn Steel austenitized

for 120 s and U-Shape DHPF at 700℃.
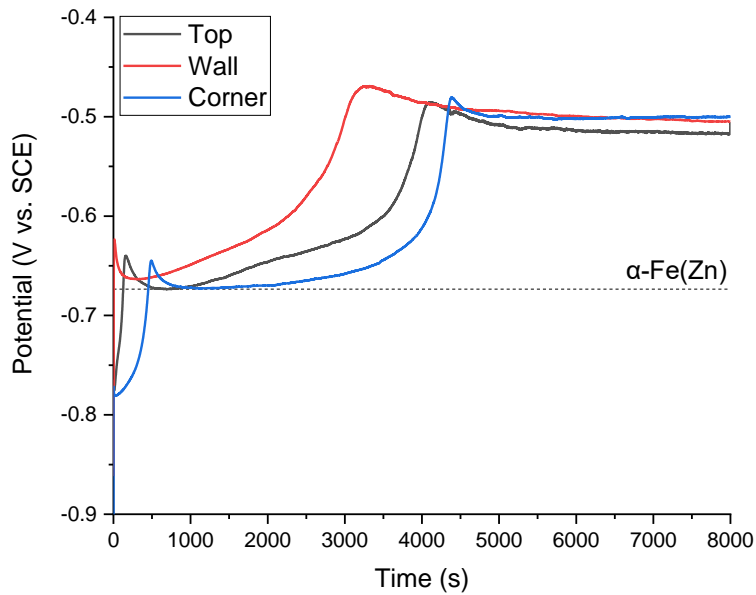
Figure 5.22: Galvanostatic scans of select regions of the Zn coated 2.5%Mn Steel austenitized

for 180 s and U-Shape DHPF at 700℃.

The galvanized coating on both steel substrates exhibited similar trends. The length of the Γ-Fe_3Zn_{10} plateau decreased with increasing austenization time. This aligns with the XRD data discussed in Figure 2.3 and Figure 2.4, where the phase fraction of Γ-Fe_3Zn_{10} followed the same trend. The length of the plateau is therefore, directly related to the amount of the phase in the coating. However, after austenization for 180 s on the 2%Mn substrate, a much greater amount of Γ-Fe_3Zn_{10} was measured by XRD (Figure 5.3) than shown in galvanostatic scans based on the lack of plateau (Figure 5.24). This could be because as the Γ-Fe_3Zn_{10} is spread thin across the surface, as seen in cross sectional images (Figure 5.10), and is completely exposed to the electrolyte. As corrosion is based on surface reactions, rather than volume, the dissolution kinetics are faster than predicted by the XRD phase fractions.

6 DISCUSSION

6.1 EFFECTS OF DHPF ON COATING SURFACE AND MICROSTRUCTURE

It is clear from the results that DHPF at 700°C of the higher Mn galvanized steels has been shown to affect all three of the regions of the U-shape part, which have been investigated in this project. Of the three regions examined, the top (region 1, Figure 5.1) is the least affected by DHPF as there is no significant deformation, and this area is placed under the least amount of strain. However, the top of the U-shaped part is compressed as the die comes down and applies an even pressure to the surface. The surface becomes compact, and this creates the coating cracks seen in Figure 5.10 in the coating of the 2%Mn steel and Figure 5.11 in that of the coated 2.5%Mn after austenization for 120 s and 180 s. This pressure is not as intense as the tensile and compressive forces that causes cracks in the wall or corner, and as such the cracks are much smaller and, in many cases, do not extend through the entire coating. EDS analysis of the crack

from the surface (Figure 5.6) show there is some additional exposed α-Fe(Zn) in this area, which is the cause of decreased electrochemical performance, discussed in §6.2 as α-Fe(Zn) is not the intermetallic phase that provides robust cathodic protection.

The outer wall of the U-shape part (region 4, Figure 5.1) is the area most affected by the DHPF process. Both the coating surface and cross-section have been damaged, as can be seen in planar imaging (Figure 5.5 and 5.7) and cross-sectional imaging (Figure 5.10 and 5.11). Friction causes the coating, particularly the Γ-Fe_3Zn_{10} phase, to adhere to the die. As the substrate is strained, the brittle coating phases fracture along α-Fe(Zn) grain boundaries, as has been seen in previous work [4, 34, 38]. This causes the coating cracks seen in Figure 5.10 and Figure 5.11, which run through the entire coating thickness at the wall. As the die is lifted, it is detached from the coating after DHPF, and two effects occur. For austenization times from 30 – 120 s, when there is more Γ-Fe_3Zn_{10} in the coating, (XRD results in Figure 5.2 and 5.4) the die wipes along the surface, causing it to be smoothed and spreading the surface Γ-Fe_3Zn_{10} (Figure 5.5 (b) and Figure 5.7 (b)). For the austenization time of 180 s when there is already a decreased amount of Γ-Fe_3Zn_{10} in the coating (as shown by XRD, Figure 5.2 and 5.4), Γ-Fe_3Zn_{10} is removed from the surface, creating patches where α-Fe(Zn) is exposed across the surface, which can be seen in EDS analysis in Figure 5.9. Variability in the coating surface morphology can also be seen, particularly in Figure 5.8 (d). The upper left side of this image has more exposed α-Fe(Zn), while the bottom right side is covered in Mn(Zn) oxides. The variability in coating surface explains the variability in diffraction patterns measured using XRD for samples of the same processing conditions (Figure 5.3).

A direct comparison of the XRD measurements completed in this work on the top (region 1, Figure 5.1) and wall (region 4, Figure 5.1) of the U-shape part can be made between those on

the coated 2%Mn steel in Figure 5.2 versus the flat hot stamped part in Figure 2.16. For

austenization times of 30 – 120 s, the vol% of Γ-Fe$_3$Zn$_{10}$ was approximately 20 vol% lower on

the top compared to the flat sample. However, after austenization for 180 s, marginally less Γ-

Fe$_3$Zn$_{10}$ was measured on the flat sample than the U-shaped sample. At the wall, the difference

was approximately 10 vol% and there was more Γ-Fe$_3$Zn$_{10}$ present after austenization for 180 s.

As both Zn-based coatings had the same weight, on the same substrate and had the same

austenization conditions, the only difference that the previous work (Figure 2.16) was flat die

quenched and the current work (Figure 5.2) was U-shape die quenched. The decrease of the

phase fraction of Γ-Fe$_3$Zn$_{10}$ is not due to the transformation of this phase into α-Fe(Zn), but the

effects of die wiping. As the die moves across the surface of the galvanized part at the wall,

surface Γ-Fe$_3$Zn$_{10}$ is removed as seen in Figure 5.6 (d) on the coated 2%Mn and Figure 5.8 (d)

on the coated 2.5%Mn. There is enough removed Γ-Fe$_3$Zn$_{10}$ to have an impact on the XRD

diffraction patterns measured (Figure 5.2 and 5.4), which causes the measured phase fractions of

Γ-Fe$_3$Zn$_{10}$ to decrease. Thus, explaining the disrepency between the phase fractions of the

coating on the flat die quenched steel and the U-shape part.

The outer corners of the U-shape part (region 2, Figure 5.1) have also been affected by

DHPF at 700°C. Evidence of this can be seen in cross-sectional images of the coating found in

Figure 5.10 for the coated 2%Mn steel and 5.11 for the coated 2.5%Mn steel. These are the areas

that have been deformed in tension. As the intermetallic coating phases are brittle, even at the

high temperature of deformation, this strain results in coating cracks. These cracks are seen in

Figure 5.10 for the 2%Mn substrate and Figure 5.11 for the 2.5%Mn substrate. The coating

cracks can be up to 10 µm wide and, at austenization times of 180 s (Figure 5.10) where there is

less Γ-Fe$_3$Zn$_{10}$ in the coating to provide cathodic protection. This increases the risk of pitting or

crevice corrosion, and subsequent substrate attack as electrolyte may be able to enter into these areas with insufficient cathodic protection [74].

6.2 EFFECT OF DHPF ON ELECTROCHEMICAL PROPERTIES

As the coating surface and microstructure is altered during DHPF, it is expected that the electrochemical properties of the galvanized steel will be affected.

A plot of E_{corr} after DHPF vs. austenization times for the 2%Mn substrate is shown in Figure 6.1. There is no significant difference in E_{corr} with respect to the location on the U-shape part or austenization time from 30 s –120 s. It can be concluded that the driving force for cathodic protection is consistent across the entire part. After austenization for 180 s, the E_{corr} has increased slightly for the wall and corner regions vs. the top (Figure 6.1), with the highest E_{corr} being observed for the corner, followed by the wall and finally the top. It should be noted that the E_{corr} for the top region austenitized for 180 s did not change significantly versus the E_{corr} observed for 120 s austenization time. As stated in the results, the increase in E_{corr} leads to a decrease in the driving force for cathodic protection provided by the coating. It has increased more for the corners due to the coating cracks, which can be seen in Figure 5.10, which allows for more exposed α-Fe(Zn). The same is true of the wall, where surface planar SEM (Figure 5.6) shows an increased amount of exposed α-Fe(Zn) on the die wiped areas compared to the bulk coating surface.
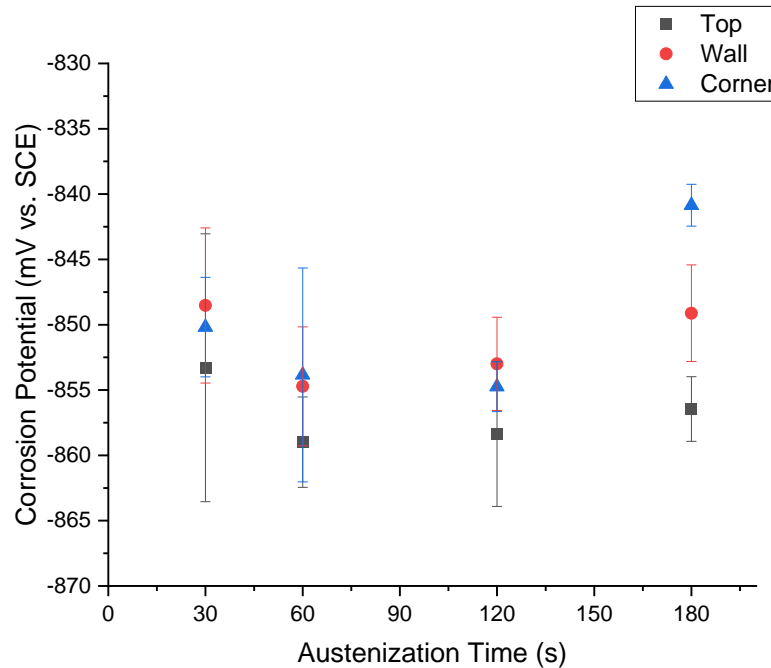
Figure 6.1: Galvanized and DHPF 2%Mn corrosion potential vs. austenization time for the top, wall, and corner of the U-shape part with 95% confidence interval.

The corrosion potential vs. austenization time for the 2.5Mn substrate is shown in Figure 6.2. After austenization for 30 s and 60 s, there is no significant change in E_{corr} between austenization times or regions on the U-shape part. The difference after austenization for 120 s is that the E_{corr} of the corner increases, while that of the top and wall stays the same. After austenization for 180 s, the wall now has a higher E_{corr} and that of the corner and top of the part are the same. The increased E_{corr} on the wall indicates that after austenization for 180 s, the die wiping causing removal of surface Γ-Fe_3Zn_{10}, as seen in Figure 5.9. The mixed potential of α-$Fe(Zn)$ causes this increased E_{corr}. At the corner, the exposed α-$Fe(Zn)$ leading to a higher E_{corr} is through coating cracks seen in Figure 5.11 and caused by the tensile deformation during DHPF. The width and number of these cracks have been observed to increase with the increasing

austenization time, but they could be variable between different DHPF panels. Further

examination may need to be conducted on the cracks formed on the corner and their ability of the

coating in this area to provide robust cathodic protection to the substrate.
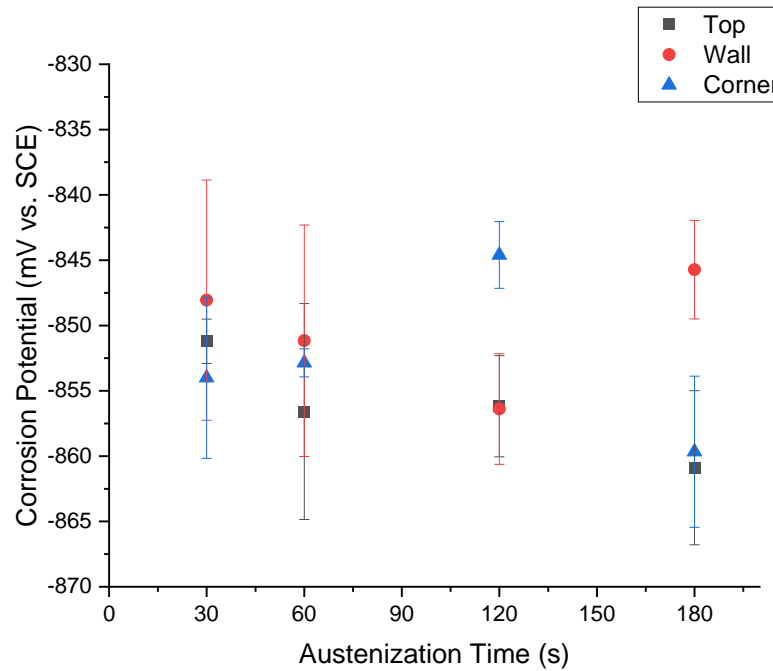
Figure 6.2: Galvanized and DHPF 2.5%Mn Corrosion Potential vs. Austenization time at the

top, wall, and corner of the U-shape part with 95% confidence interval.

The average E_{corr} measured in triplicate potentiodynamic polarizations is plotted against

the vol % Γ-Fe_3Zn_{10} in the DHPF coating in Figure 6.3 with 95% CI error bars. For both steel

substrates, it can be seen there is no significant dependence of E_{corr} with respect to the coating

phase fraction of Γ-Fe_3Zn_{10}. Dever, when conducting similar experiments on Zn-based coatings

on 22MnB5, found that the E_{corr} increases to approximately –0.67 mV vs. SCE when the phase

fraction of Γ-Fe_3Zn_{10} is less than 10 vol% [36]. A guideline was set based on this information,

where a minimum 15 vol% is required for a Zn-based coating to provide robust cathodic

protection. XRD measurements of the coating phases on both the top and the wall of the coated 2.5%Mn steel measured an average phase fraction of 7 ± 2 vol% on the top and 10 ± 6 vol% on the wall, but the E_{corr} did not increase in either case. As the E_{corr} did not increase, it can be suggested that robust cathodic protection is still provided in these areas, despite not meeting the guidelines. The error bars on the wall put the 15 vol% criterion within range, so this is still consistent with previous findings, but with consideration for error, the E_{corr} of the top should increase based on an insufficient vol% Γ-Fe_3Zn_{10}.
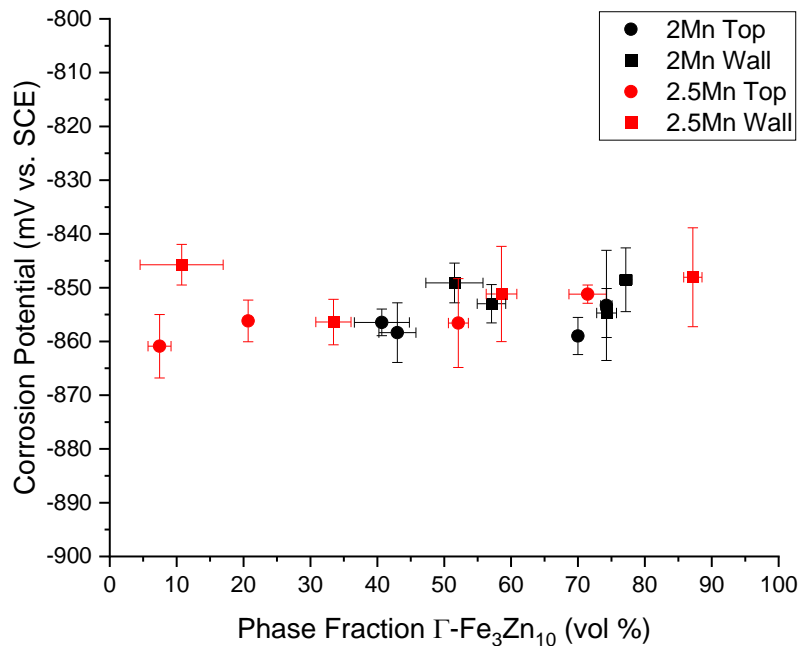
Figure 6.3: Corrosion potential vs. volume % Γ-Fe_3Zn_{10} of the top and wall of the 2%Mn (red) and 2.5%Mn (black) DHPF part with 95% confidence interval.

It is proposed that the ability of the coating to provide robust cathodic protection is not only dependant on the phase fraction of Γ-Fe_3Zn_{10} in the Zn-based coating, but also on the coating surface. It has been shown that the dissolution of α-Fe(Zn) not only occurs after the Γ-

Fe_3Zn_{10} has been exhausted, but also at a higher potential, which can be seen in the secondary peak in Figure 5.13. The mixed phase potential is what would cause the E_{corr} to rise, but this is not seen on the coated DHPF steel. But there is not enough removed Γ-Fe_3Zn_{10} to have such an effect on the E_{corr} as it does not increase due to the additional exposed α-Fe(Zn). Thus, it is concluded that the decreased driving force for cathodic protection is not based on thermodynamics, which predicts robust cathodic protection for all conditions, but instead on corrosion kinetics and surface reactions.

Galvanic coupling behaviour between the substrate steel and the coating phases is shown in the Evans diagram in Figure 6.4. From this diagram, the corrosion potential of the galvanic couple (E_{gc}) between the steel substrate and α-Fe(Zn) was found to be $E_{gc(2\%Mn - \alpha\text{-}Fe(Zn))} = -688$ mV vs. SCE and $E_{gc(2.5\%Mn - \alpha\text{-}Fe(Zn))} = -685$ mV vs. SCE. These values are not significantly different from each other, implying no effect of the addition of Mn in the substrate. The values are consistent with similar work involving a Zn-based coating of only α-Fe(Zn) on 22MnB5 steel [36]. The coupled corrosion potential of the steel substrate to Γ-Fe_3Zn_{10} is $E_{gc(2\%Mn - \Gamma\text{-}Fe3Zn10)} = -852$ mV vs. SCE and $E_{gc(2.5\%Mn - \Gamma\text{-}Fe3Zn10)} = -849$ mV vs. SCE. These values are similar to the E_{corr} measured on the mixed phase coatings on the U-shape DHPF parts.

In addition, the coupled anodic current density (i_{gc}) can be determined from this diagram. i_{gc} of the steel substrate to the α-Fe(Zn) phase is $i_{gc(2\%Mn - \alpha\text{-}Fe(Zn))} = 8.841$ μA/cm^2 and $i_{gc(2.5\%Mn - \alpha\text{-}Fe(Zn))} = 5.76$ μA/cm^2. That of the steel substrate coupled to Γ-Fe_3Zn_{10} is $i_{gc(2\%Mn - \Gamma\text{-}Fe3Zn10)} = 0.026$ μA/cm^2 and $i_{gc(2.5\%Mn - \Gamma\text{-}Fe3Zn10)} = 0.015$ μA/cm^2. The i_{gc} of the steel substrate coupled to Γ-Fe_3Zn_{10} is significantly lower than that of the steel substrate coupled to α-Fe(Zn), indicating a lower rate of dissolution for Γ-Fe_3Zn_{10} when coupled with the steel. Therefore Γ-Fe_3Zn_{10} provides a longer duration of cathodic protection than α-Fe(Zn) when comparing similar

amounts in the coating. The difference in I_{gc} between the two substrates and each coating phase is small and does not indicate any significant effect of the Mn addition to the corrosion rate of the coating phases when coupled to the substrate.
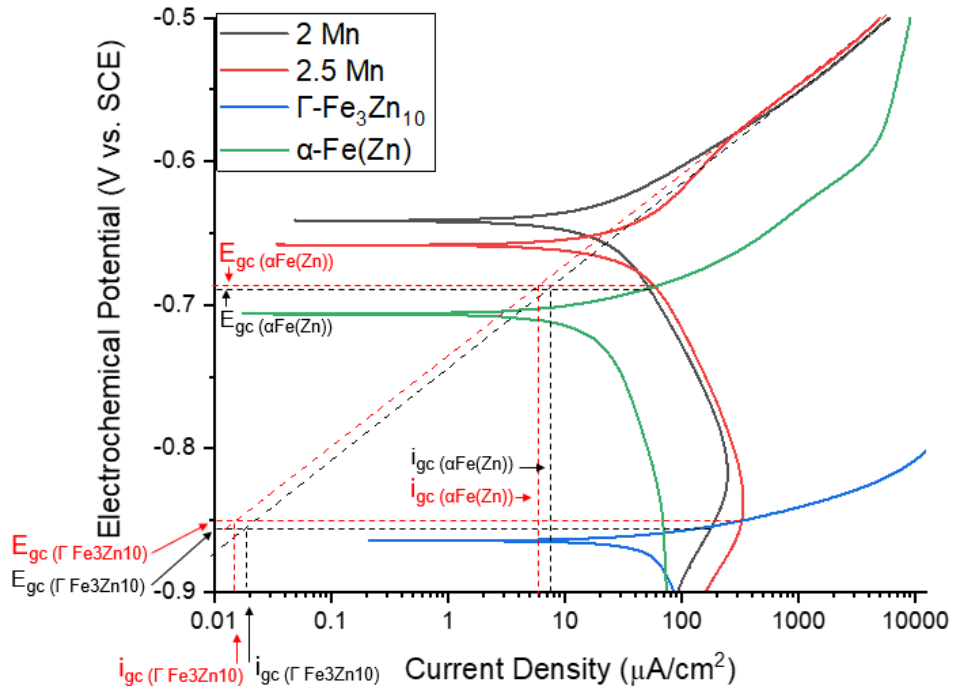
Figure 6.4: Galvanic coupling of the bare 2%Mn (black) and 2.5%Mn (red) steels isolated coating phases α-Fe(Zn) and Γ-Fe₃Zn₁₀.

However, at the top and wall of the part, the substrate is not exposed to the electrolyte. Instead, due to the removal of surface Γ-Fe₃Zn₁₀ as seen in Figure 5.6 and 5.8, a galvanic couple is formed between the coating phases α-Fe(Zn) and Γ-Fe₃Zn₁₀. The Evans diagram of this is shown in Figure 6.5. From this diagram, the $E_{gc} = -858$ mV vs. SCE, again comparable to the E_{gc} of the phase coupled to the steel substrates, as well as the E_{corr} on the U-shape parts. The $i_{gc} = 0.141$ μA/cm², which is higher than that of Γ-Fe₃Zn₁₀ when coupled to the steel substrate. The

rate of dissolution of this phase is faster when coupled to α-Fe(Zn), such is the case in the die wiped regions of the U-shape part. This is the reason the complete dissolution of Γ-Fe$_3$Zn$_{10}$, as measured by galvanostatic scans in Figures 5.15 – 5.22 occurs sooner at the top and wall of the part where Γ-Fe$_3$Zn$_{10}$ is galvanically coupled to α-Fe(Zn).
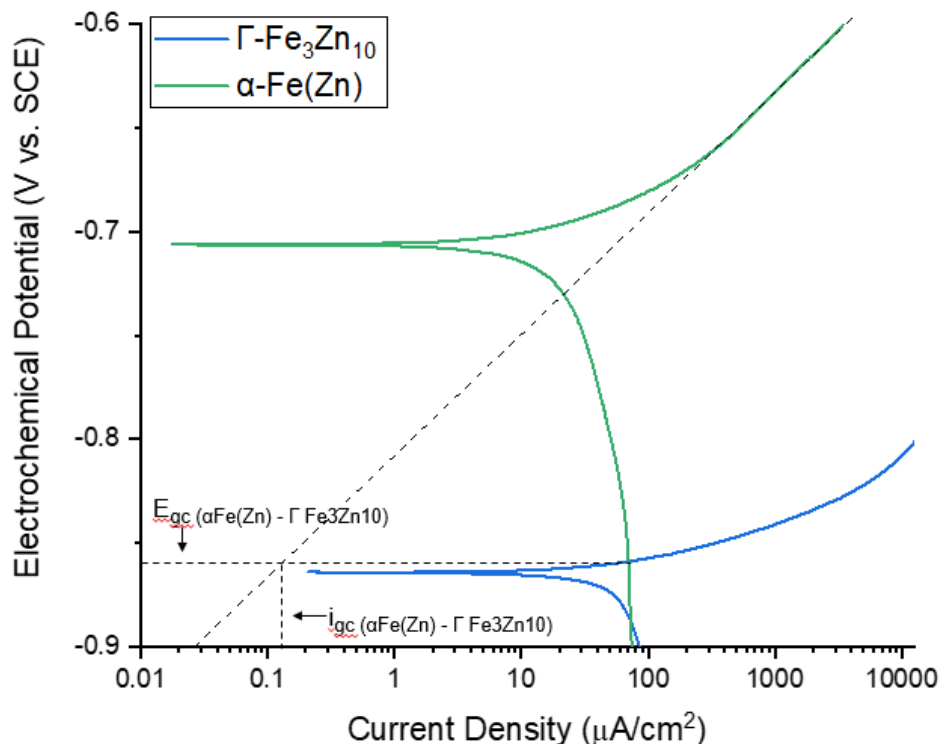
Figure 6.5: Galvanic coupling of flat die quenched Zn-based coatings of isolated α-Fe(Zn) and Γ-Fe$_3$Zn$_{10}$.

As discussed in §5.6, Γ-Fe$_3$Zn$_{10}$ is the only phase in the coating, which is able to provide robust cathodic protection. Therefore, robust cathodic protection is no longer available after the complete dissolution of Γ-Fe$_3$Zn$_{10}$, as the phase is no longer present in the coating. Galvanostatic scans, presented in §5.7, were used to determine the dissolution kinetics of the coating. The first plateau, at approximately –800 mV vs. SCE is indicative of the dissolution of Γ-Fe$_3$Zn$_{10}$. The

end of this plateau implies the complete dissolution of Γ-Fe_3Zn_{10}. The end of the average Γ-Fe_3Zn_{10} plateau length in seconds is plotted against austenization time in Figure 6.6. The grey envelope is a 95% confidence interval for the consolidated data from the coated 2%Mn steel, and the red envelope is a 95% confidence interval for the consolidated data from the coated 2.5%Mn steel.
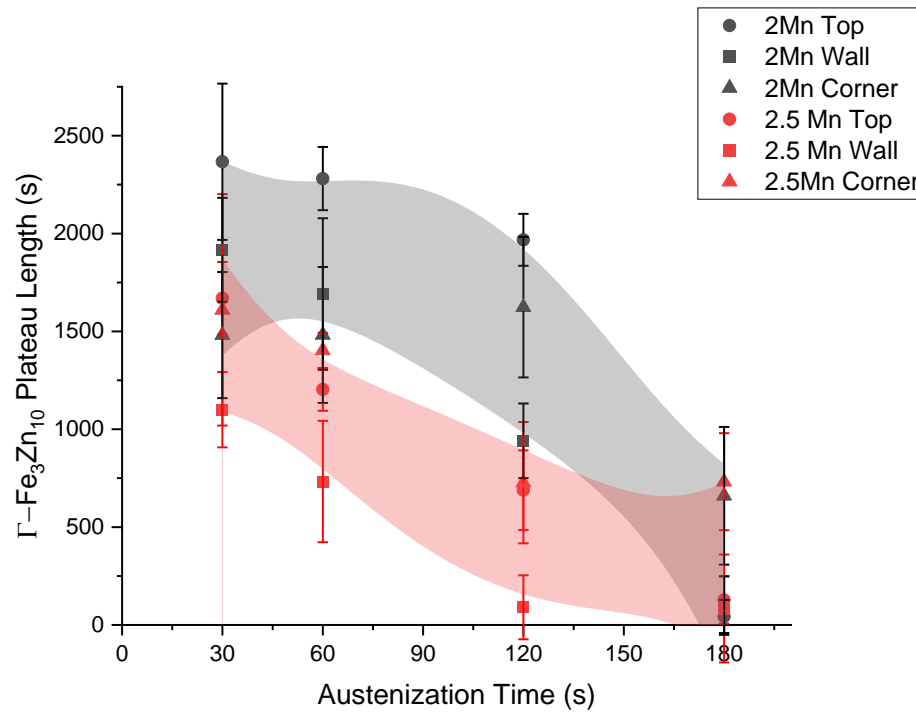
Figure 6.6: Γ-Fe_3Zn_{10} plateau length vs. austenization time for the Zn-coated 2%Mn (black) and 2.5%Mn (red) substrate after DHPF at 700°C with respective 95% confidence intervals.

Overall, the length of the Γ-Fe_3Zn_{10} plateau decreases with the increasing austenization time. It was found in XRD measurements (Figure 5.2 and 5.4) that the phase fraction of coating

Γ-Fe_3Zn_{10} decreases with the increasing austenization time, which accounts for the decreasing plateau length. This is further discussed later in this section.

Figure 6.6 shows the Γ-Fe_3Zn_{10} plateau is generally longer for the coated 2%Mn steel than the coated 2.5%Mn steel. For both substrates, the area that has the longest plateau for austenization from 30 s – 120 s, is the top of the 2%Mn part (region 1, Figure 5.1), the area least affected by DHPF. It can be concluded the part top is where cathodic protection is provided for the longest duration. But after austenization for 180 s, the average length of the Γ-Fe_3Zn_{10} plateau at the top is close to 0 s, where the plateau does not appear for any significant duration in the galvanostatic scan. It was concluded that robust cathodic protection is not provided on the top or wall of the U-shape part after 180 s.

The wall (region 4, Figure 5.1), as discussed in §6.1, was the area of the U-shaped part most impacted by DHPF. This is reflected in the length of the Γ-Fe_3Zn_{10} plateau, indicated by the black squares for the 2%Mn substrate and the red squares for the 2.5%Mn substrate in Figure 6.6. For all the measured samples, the wall of the coated DHPF U-shape part on the 2.5%Mn steel had the shortest Γ-Fe_3Zn_{10} plateau. The additional exposed α-Fe(Zn) from the die wiped regions, as well as the coating cracks left a significant portion of the surface defects that require cathodic protection. The cathodic protection of Γ-Fe_3Zn_{10} is provided by the coating for the least amount of time in this region, leaving it susceptible to corrosion. Especially after austenization times of 120 s and 180 s when there is less Γ-Fe_3Zn_{10} to provide cathodic protection (Figure 5.2 and 5.6). Therefore, the dissolution occurs faster at the wall compared to the top and corners. There is an insufficient amount of Γ-Fe_3Zn_{10} to form a plateau after austenization for 120 s,

indicating that robust cathodic protection does not occur in this region, again leaving this an area which is suspectable to corrosion.

A plot of the length of the Γ-Fe$_3$Zn$_{10}$ plateau, determined by galvanostatic scans where the sample was held at a current density of +10 mA/cm^2, against the phase fraction of Γ-Fe$_3$Zn$_{10}$, measured by XRD is shown in Figure 6.7. Overall, as the phase fraction of Γ-Fe$_3$Zn$_{10}$ decreases, the length of the plateau decreases as there is less of the phase in the coating for dissolution.
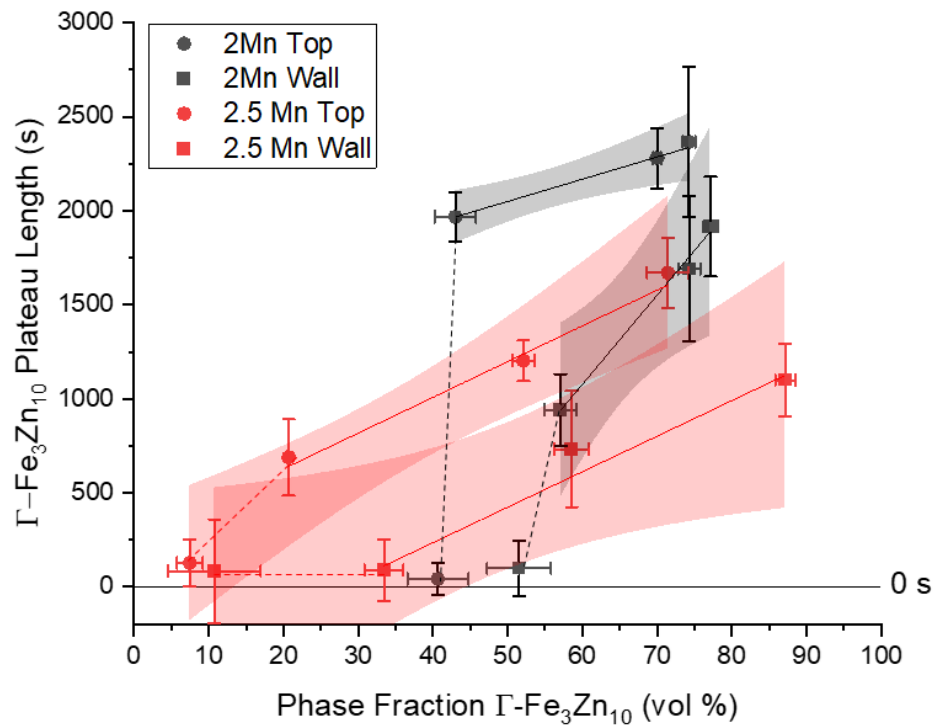
Figure 6.7: Γ-Fe$_3$Zn$_{10}$ plateau length vs. phase fraction Γ-Fe$_3$Zn$_{10}$ on DHPF galvanized 2%Mn (black) and 2.5%Mn (red) with 95% confidence intervals.

The length of the Γ-Fe$_3$Zn$_{10}$ plateau is linear with respect to the phase fraction of Γ-Fe$_3$Zn$_{10}$ for the three highest phase fraction measurements in each region on the steel. This

indicated a direct relationship between length of the Γ-Fe_3Zn_{10} plateau and phase fraction measured by XRD (Figure 5.2 and 5.4).

However, there is a sudden decrease in Γ-Fe_3Zn_{10} plateau length at the lowest phase fraction measured in each Zn-based coating. The sudden drop occurs at different phase fractions for each sample, but all when the phase fraction of Γ-Fe_3Zn_{10} is less than 52 vol%. This is not a consistent trend, however, because at the top of both the coated steel parts, it can be seen that an average plateau length of 1968 s and 689 s is measured on the top of the DHPF 2%Mn and 2.5%Mn steels respectively below the first drop. The sudden drop off in Γ-Fe_3Zn_{10} indicates that this is not because of the decrease in phase fraction of Γ-Fe_3Zn_{10}, which decreases due to additional austenization time. This is corroborated by Figure 6.3, where the phase ratio does not have a specific effect on the E_{corr}. Therefore, this sudden dissolution of the Γ-Fe_3Zn_{10} plateau in galvanostatic scans is decreased by surface and coating defects with regards to die wiping and coating cracks (Figures 5.5, 5.7, 5.10 and 5.11). In these areas, α-Fe(Zn), which does not provide robust cathodic protection, is exposed to the electrolyte. The dissolution kinetics are faster than predicted by the XRD phase fractions in these areas, resulting in an insufficient amount of coating Γ-Fe_3Zn_{10} to be measured by galvanostatic scans. These factors need to be taken into consideration when evaluating whether corrosion resistance is provided to DHPF parts.

The dissolution of bare steel occurs after both coating phases have been exhausted. This point can be determined in galvanostatic scans as the time when the third and final plateau at a potential of approximately –660 mV vs. SCE. The time to dissolution of bare steel vs. austenization time for both substrates is shown in Figure 6.8.

The time to dissolution of bare steel in galvanostatic scans increases with increasing austenization time up until 120 s. This is because the phase fraction of α-Fe(Zn) provides barrier

protection against corrosion with a weak cathodic protection. With longer times in the furnace, the Zn from the coating diffuses into the substrate steel, which makes the coating thicker (seen in Figure 5.10 and 5.11). This further increases the barrier protection, thus delaying the time to the dissolution of the substrate steel.
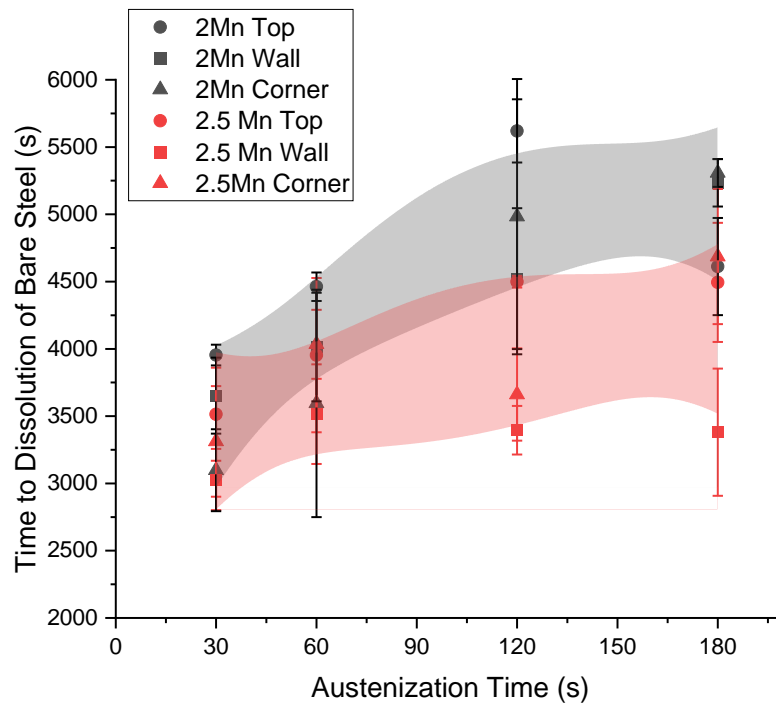
Figure 6.8: Time to the dissolution of bare steel on galvanized DHPF steel vs. austenization time with 95% confidence intervals.

However, on the wall of the U-shape part with the 2.5%Mn substrate, the dissolution of bare steel does not follow this trend. This is also due to the cracks in the area. Robust cathodic protection is not provided at this austenization time in this location. As such, the electrolyte solution is able to enter into the cracks. This creates for surface area for corrosion, thus

accelerating the process. This is the same reason that for most regions, the time to the dissolution of bare steel does not increase after austenization for 180 s.

6.3 DHPF OF GALVANIZED 2%MN VS. 2.5%MN STEEL

The effects of DHPF on the galvanized coating such as die wiping at the part wall and the formation of coating cracks was not significantly different between the galvanized 2%Mn and 2.5%Mn steel. The coating cross-sectional microstructure (Figure 5.10 and 5.11), as well as the coating surface appearance after austenization for 30 s (Figure 5.5 (a) and 5.7 (a)) do not show any significant differences between the two grades of steel. However, after austenization for 180 s, the surface of the coated 2.5%Mn had a more compact layer of oxides than the coated 2%Mn (Figure 5.5 (c) vs. Figure 5.7 (c)). In addition, the surface of the coated 2.5%Mn steel had a greater amount of exposed α-Fe(Zn), which does not provide significant cathodic protection and negatively impacts the corrosion resistance over cracks or other defects (Figure 5.10 and 5.11). There are also larger Mn oxides on the surface of the 2.5%Mn steel due to the surface segregation of Mn (Figure 5.7 and 5.9).

Overall, the coated 2.5%Mn steel DHPF at 700°C provided a lower driving force for cathodic protection that did not last for the same duration as the coated 2%Mn steel under the same processing conditions, as could be seen in the potentiodynamic polarizations and galvanostatic scans. This difference is most apparent austenization times of 120 s and 180 s. As can be seen in Figure 6.3, the 2.5%Mn steel coating had a lower phase fraction of Γ-Fe$_3$Zn$_{10}$ than the 2%Mn steel for equivalent processing conditions. As this is the primary phase that is responsible for robust cathodic protection, the decrease in coating Γ-Fe$_3$Zn$_{10}$ would be the explanation for why the length of the Γ-Fe$_3$Zn$_{10}$ plateau is shorter than that on the coated 2%Mn steel. In addition, the driving force for cathodic protection, calculated using ΔE$_{corr}$ in § 5.5 (based

off potentiodynamic polarizations in Figure 5.12), determined that ΔE between the intermetallic phases was greater on the 2%Mn substrate than the 2.5%Mn substrate. The $E^{°}_{Mn} = -1.22$ V vs. SHE, which is much more active than that of Fe ($E^{°}_{Fe} = -0.44$ V vs. SHE) or even Zn ($E^{°}_{Zn} = -0.76$ V vs. SHE) [82]. Mn is significantly more active than Fe based on their electrochemical potentials, which is why the E_{corr} on the 2.5%Mn substrate is less than that of the 2%Mn substrate. This is supported by Fajardo et al., who determined that an addition of Mn to a steel would be detrimental to the corrosion resistance of ungalvanized steel It was also found that more Mn leads to greater dissolution current densities [83]. Conversely, Townsend found the addition of Mn to be insignificant to the corrosion behaviour, but only used a maximum amount of 1.5 wt% Mn in the steel [84]. The addition of Mn to the steel, as well as the tendency of Mn to segregate to the surface can account for why the coated 2.5%Mn steel provided less cathodic protection time than the 2%Mn substrate.

7   CONCLUSIONS AND RECOMMENDATIONS

7.1   CONCLUSIONS

In this work, a thorough investigation of the effects of DHPF on two prototype Zn-coated Mn-containing press hardening steels was conducted to determine the ability of a Zn-based coating to provide robust cathodic protection. The coating surface of the galvanized U-shape part after DHPF at 700°C observed surface morphology changes between the top and wall of the part due to die wiping. XRD analysis also showed differences between these two regions of the U-shape part. Coating cracks appear at the wall and corners, which can act as corrosion initiation sites of the steel substrate if there is insufficient robust cathodic protection to these areas. Electrochemical experiments have determined that the lower duration of robust cathodic

protection exhibited by the DHPF parts is due to coating damage during stamping, and that the phase fraction of Γ-Fe_3Zn_{10} is an insufficient criterion for determining if robust cathodic protection is provided.

The following conclusions can be drawn:

- DHPF galvanized steel at 700°C causes damage to the coating through two mechanisms:
  - Friction from the die causes "die wiping" as surface Γ-Fe_3Zn_{10} adheres to the die and is removed from the coating. This smooths the coating surface when there is a significant amount of Γ-Fe_3Zn_{10} in the coating, or results in exposed α-Fe(Zn) when there is not.
  - Coating cracks form along α-Fe(Zn) grain boundaries when the part has been substantially deformed (at the outer corner) or when the coating has been wiped (at the wall). After austenization for 180 s, coating cracks can also form at the top of the part due to surface compression
- The ability of the galvanized coating to provide robust cathodic protection to both substrates is less effective for austenization times of 120 s – 180 s.
- The wall of the U-shape part stamped at 700°C provided robust cathodic protection for a shorter duration than the corner and the top of the same part.
  - This indicates that die wiping is more harmful to the ability to provide corrosion resistance than coating cracks.
- The galvanized coating is able to provide robust cathodic protection on:
  - 2%Mn steel for austenization times from 30 s – 120 s.
  - 2.5%Mn steel for austenization times of 30 s – 60 s.

7.2 RECOMMENDATIONS

To ensure robust cathodic protection is provided by the Zn-based coating, the integrity of the coating must be maintained during DHPF. As die wiping, particularly on the wall of the DHPF part (region 4, Figure 5.1), has been most detrimental to the ability of the coating to provide robust cathodic protection, this should be avoided. Stamping at a lower temperature may help mitigate this effect. XRD results on flat die quenched steel in Figure 2.16 show that stamping at $600 - 650°C$ has resulted in a slightly greater amount of Γ-Fe_3Zn_{10} in the coating after austenization for 180 s, which may improve the duration of robust cathodic protection provided by this phase. In addition, by reducing die friction during DHPF, the adhesion of the coating to the die can be lessened, which may reduce both die wiping and surface cracks on the wall. Lee et al. has suggested that increasing the heating rate would create a smoother surface, thus decreasing friction [71]. Ghiotti et al. have suggested that increasing the speed at which the die moves would reduce friction and coating cracks in DHPF parts when stamping at $600°C$ and $800°C$. Finally, an oil lubricant may also be applied to the die, which reduces deformation at the steel/coating interface [9, 10]. Any of these methods may be applied to reduce die wiping and coating cracking during DHPF, therefore improving the ability of the coating to provide robust cathodic corrosion resistance.

Further experimental recommendations include:

- Quantify the loss of Γ-Fe_3Zn_{10} at the part wall and top due to die wiping.
- Determine a new criterion for the ability of a Zn-based coating to provide robust cathodic protection to the steel substrate that accounts for the effects of die wiping and coating cracks that form during DHPF on the electrochemical properties.

- Further examination of the galvanic coupling between the coating phases (α-Fe(Zn) and Γ-Fe_3Zn_{10}) in die wiped regions.

- Isolate Mn in coating phases to further determine the effect of this alloying element on the corrosion behaviour of the coating.

- SAE J2334 salt spray tests on U-shape parts of both Zn-coated 2%Mn and 2.5%Mn steels to further determine corrosion behaviour on the part as a whole.

8   REFERENCES

[1]   K. Bachman, "Hot-stamped parts in 2019 vehicles," *Stamping Journal*, pp. 22–28, 2018.

[2]   A. R. Marder, "The metallurgy of zinc-coated steel A.R.," *Prog. Mater. Sci.*, vol. 45, pp. 191–271, 2000.

[3]   W. D. J. Callister and D. G. Rethwisch, *Materials Science and Engineering: An Introduction*, 9th Editio. Hoboken, NJ: Wiley, 2014.

[4]   C. Thomsen, "Development of New Grades of Zinc Coated Direct Press-Hardenable Steel With Robust Cathodic Protection," McMaster University, 2020.

[5]   H. Karbasian and A. E. Tekkaya, "A review on hot stamping," *J. Mater. Process. Technol.*, vol. 210, no. 15, pp. 2103–2118, 2010.

[6]   M. Naderi, "Hot Stamping of Ultra High Strength Steels," Rheinisch-Westfälischen Technischen Hochschule Aachen,Teheran, Iran, 2007.

[7]   D. W. Fan and B. C. De Cooman, "State-of-the-knowledge on coating systems for hot stamped parts," *Steel Res. Int.*, vol. 83, no. 5, pp. 412–433, 2012.

[8]   M. Naderi, M. Ketabchi, M. Abbasi, and W. Bleck, "Analysis of microstructure and mechanical properties of different boron and non-boron alloyed steels after being hot stamped," *Procedia Eng.*, vol. 10, pp. 460–465, 2011.

[9]   H. Mohrbacher, "Martensitic Automotive Steel Sheet - Fundamentals and Metallurgical Optimization Strategies," *Adv. Mater. Res.*, vol. 1063, pp. 130–142, 2014.

[10] B. Çetin and H. Meço, "Hot Stamping of Ultra High-Strength Steels," in *Hot Stamping of Ultra High-Strength Steels*, 2019, pp. 19–29.

[11] D. W. Fan, H. S. Kim, and B. C. De Cooman, "A Review of the Physical Metallurgy related to the Hot Press Forming of Advanced High Strength Steel," *Steel Res. Int.*, vol. 80, no. 3, pp. 241–248, 2009.

[12] L. Vaissiere, J. P. Laurent, and A. Reinhardt, "Development of pre-coated boron steel for applications on PSA peugeot citroën and RENAULT bodies in white," *SAE Tech. Pap.*, no. 724, 2002.

[13] R. Neugebauer, F. Schieck, S. Polster, A. Mosel, A. Rautenstrauch, and J. Scho, "Press hardening — An innovative and challenging technology," *Arch. Civ. Mech. Eng.*, vol. 12, pp. 113–118, 2012.

[14] R. Grigorieva, P. Drillet, J.-M. Mataigne, and P. Carges, "Study of the Phase Transformation in Al-Si Coating During the Austenization Step," in *Galvatech*, 2011.

[15] M. Windmann, A. Röttger, and W. Theisen, "Formation of intermetallic phases in Al-coated hot-stamped 22MnB5 sheets in terms of coating thickness and Si content," *Surf. Coat. Technol.*, vol. 246, pp. 17–25, 2014.

[16] D. W. Fan, H. S. Kim, J.-K. Oh, K.-G. Chin, and B. C. De Cooman, "Coating Degradation in Hot Press Forming," *ISIJ Int.*, vol. 50, no. 4, pp. 561–568, 2010.

[17] L. Dosdat, J. Petitjean, T. Vietoris, and O. Clauzeau, "Corrosion resistance of different metallic coatings on press-hardened steels for automotive," *Steel Res. Int.*, vol. 82, no. 6, pp. 726–733, 2011.

[18] C. Pucci *et al.*, "Electrochemical behaviour of 22MnB5 steel coated with hot-dip Al-Si before and after hot-stamping process investigated by means of scanning Kelvin probe microscopy," *Corros. Sci.*, vol. 174, p. 108811, 2020.

[19] M. Tisza, "Hot Forming of Boron Alloyed Manganese Steels," *Mater. Sci. Forum*, vol. 885, pp. 25–30, 2017.

[20] E. Billur, "Hot formed steels," in *Metallurgy of Steels and Blank Materials. In: Hot Stamping of Ultra High-Strength Steels, From a Technological and Business Perspective*, Elsevier Ltd, 2017, pp. 385–410.

[21] C. W. Lee, D. W. Fan, I. R. Sohn, S. J. Lee, and B. C. De Cooman, "Liquid-metal-induced embrittlement of Zn-coated hot stamping steel," *Metall. Mater. Trans. A Phys. Metall. Mater. Sci.*, vol. 43, no. 13, pp. 5122–5127, 2012.

[22] M. Nikravesh, M. Naderi, G. H. Akbari, and W. Bleck, "Phase transformations in a simulated hot stamping process of the boron bearing steel," *Mater. Des.*, vol. 84, pp. 18–24, 2015.

[23] Y. Chang, Z. Meng, L. Ying, X. Li, N. Ma, and P. Hu, "Influence of Hot Press Forming Techniques on Properties of Vehicle High Strength Steels," *J. Iron Steel Res. Int.*, vol. 18, no. 5, pp. 59–63, 2011.

[24] Y. H. Kweon and H. D. Kim, "Study on the wiping gas jet in continuous galvanizing line," *J. Therm. Sci.*, vol. 20, no. 3, pp. 242–247, 2011.

[25] J. R. McDermid, M. H. Kaye, and W. T. Thompson, "Fe Solubility in the Zn-Rich Corner of the Zn-Al-Fe System for Use in Continuous Galvanizing and Galvannealing," *Metall. Mater. Trans. B*, vol. 38B, no. April, pp. 215–230, 2007.

[26] E. A. Silva, private communication, date unknown.

[27] L. Chen, R. Fourmentin, and J. R. McDermid, "Morphology and Kinetics of Interfacial Layer Formation during Continuous Hot-Dip Galvanizing and Galvannealing," *Metall. Mater. Trans. A*, vol. 39A, pp. 2128–2142, 2008.

[28] N. Y. Tang, "Characteristics of continuous-galvanizing baths," *Metall. Mater. Trans. B Process Metall. Mater. Process. Sci.*, vol. 30, no. 1, pp. 144–148, 1999.

[29] P. Pokorny, J. Kolisko, L. Balik, and P. Novak, "Description of structure of Fe-Zn intermetalic compounds present in hot-dip galvanized coatings on steel," *Metalurgija*, vol. 54, no. 4, pp. 707–710, 2015.

[30] T. B. Massalski, *Binary Alloy Phase Diagrams*. ASM Int.3, 1992.

[31] D. Pallisco, private communication, 2021.

[32]   R. Autengruber, G. Luckeneder, S. Kolnberger, J. Faderl, and A. W. Hassel, "Surface and coating analysis of press-hardened hot-dip galvanized steel sheet," *Steel Res. Int.*, vol. 83, no. 11, pp. 1005–1011, 2012.

[33]   H. Peng, W. Peng, R. Lu, G. Wu, and J. Zhang, "Diffusion and cracking behavior involved in hot press forming of Zn coated 22MnB5," *J. Alloys Compd.*, vol. 806, pp. 195–205, 2019.

[34]   K. Wang *et al.*, "Successive phase and morphology evolution of galvannealed coating in hot stamping and diffusion modeling of α-Fe(Zn)/steel system considering the effect of Zn concentration," *Surf. Coatings Technol.*, vol. 380, no. August, p. 125036, 2019.

[35]   C. W. Lee, D. W. Fan, S. J. Lee, I. R. Sohn, and B. C. De Cooman, "Galvanized Coating Evolution During Hot Stamping," in *Galvatech*, 2011.

[36]   C. Dever, "Effect of Coating Microstructure on the Electrochemical Properties of Continuous Galvanized Coatings on Press Hardened Steels," McMaster University, 2018.

[37]   V. Janik, Y. Lan, P. Beentjes, D. Norman, G. Hensen, and S. Sridhar, "Zn Diffusion and Fe(Zn) Layer Growth during Annealing of Zn-Coated B Steel," *Metall. Mater. Trans. A*, vol. 47, pp. 400–411, 2016.

[38]   C. Dever, J. Kish, and J. R. McDermid, "Corrosion Properties of Hot Dip Zinc Galvanized Coatings on 22MnB5 Press Hardened Steels," in *Galvatech*, 2017, pp. 385–392.

[39]   W. Gaderbauer *et al.*, "Effects of alloying elements on surface oxides of hot – dip galvanized press hardened steel," *Surf. Coat. Technol.*, vol. 404, p. 126466, 2020.

[40]   K. Maleki, "On the Origin of Micro-Cracking in Zn-Coated Press Hardened Steels," McMaster University, 2019.

[41]   Y. Yoshikawa *et al.*, "United States Patent," 2008.

[42]   S. P. Murugan *et al.*, "Role of liquid Zn and α-Fe(Zn) on liquid metal embrittlement of medium Mn steel: An ex-situ microstructural analysis of galvannealed coating during high temperature tensile test," *Surf. Coatings Technol.*, vol. 398, no. June, p. 126069, 2020.

[43]   M. H. Razmpoosh, C. DiGiovanni, Y. Zhou, and E. Biro, "Pathway to understand liquid metal embrittlement (LME) in Fe-Zn couple: From fundamentals toward application," *Prog. Mater. Sci.*, no. March, p. 100798, 2021.

[44]   B. Joseph, M. Picat, and F. Barbier, "Liquid metal embrittlement: A state-of-the-art appraisal," *EPJ Appl. Phys.*, vol. 5, no. 1, pp. 19–31, 1999.

[45]   A. R. C. Westwood and M. H. Kamdar, "Concerning liquid metal embrittlement, particularly of zinc monocrystals by mercury," *Philos. Mag.*, vol. 8, no. 89, pp. 787–804, 1963.

[46]   S. P. Lynch, "Mechanisms and kinetics of environmentally assisted cracking: Current status, issues, and suggestions for further work," *Metall. Mater. Trans. A Phys. Metall. Mater. Sci.*, vol. 44, no. 3, pp. 1209–1229, 2013.

[47]   N. S. Stoloff and T. L. Johnston, "Crack propagation in a liquid metal environment," *Acta Metall.*, vol. 11, no. 4, pp. 251–256, 1963.

[48]   M. H. Razmpoosh, A. Macwan, F. Goodwin, E. Biro, and Y. Zhou, "Role of Random and Coincidence Site Lattice Grain Boundaries in Liquid Metal Embrittlement of Iron (FCC)-Zn Couple," *Metall. Mater. Trans. A Phys. Metall. Mater. Sci.*, vol. 51, no. 8, pp. 3938–3944, 2020.

[49]   E. E. Glickman, "On the Role of Stress, Strain and Diffusion in Dissolution – Condensation Mechanism of Liquid Metal Embrittlement," *Defect Diffus. Forum*, vol. 264, pp. 141–149, 2007.

[50]   E. E. Glickman, "Grain Boundary Grooving Accelerated by Local Plasticity as a Possible Mechanism of Liquid Metal Embrittlement," *Interface Sci.*, vol. 11, no. 4, pp. 451–459, 2003.

[51]   S. P. Lynch, "Environmentally assisted cracking: Overview of evidence for an adsorption-induced localised-slip process," *Acta Metall.*, vol. 36, no. 10, pp. 2639–2661, 1988.

[52]   P. Gordon and H. H. An, "The mechanisms of crack initiation and crack propagation in metal-induced embrittlement of metals," *Metall. Trans. A*, vol. 13, no. 3, pp. 457–472, 1982.

[53]   L. Cho, L. Golem, E. J. Seo, D. Bhattacharya, J. G. Speer, and K. O. Findley, "Microstructural characteristics and mechanical properties of the Al–Si coating on press hardened 22MnB5 steel," *J. Alloys Compd.*, vol. 846, p. 156349, 2020.

[54]   D. Bhattacharya *et al.*, "Influence of the starting microstructure of an advanced high strength steel on the characteristics of Zn-Assisted liquid metal embrittlement," *Mater. Sci. Eng. A*, vol. 804, no. October 2020, p. 140391, 2021.

[55]   C. Beal, X. Kleber, D. Fabregue, and M. Bouzekri, "Embrittlement of a zinc coated high manganese TWIP steel," *Mater. Sci. Eng. A*, vol. 543, pp. 76–83, 2012.

[56]   L. Cho, H. Kang, C. W. Lee, and B. C. De Cooman, "Microstructure of liquid metal embrittlement cracks on Zn-coated 22MnB5 press-hardened steel," *Scr. Mater.*, vol. 90, no. 1, pp. 25–28, 2014.

[57]   C. W. Lee, W. S. Choi, L. Cho, Y. R. Cho, and B. C. De Cooman, "Liquid-metal-induced embrittlement related microcrack propagation on Zn-coated press hardening steel," *ISIJ Int.*, vol. 55, no. 1, pp. 264–271, 2015.

[58]   M. Takahashi, M. Nakata, K. Imai, N. Kojima, and N. Otsuka, "Liquid metal embrittlement of hot stamped galvannealed boron steel sheet - Effect of heating time on crack formation," *ISIJ Int.*, vol. 57, no. 6, pp. 1094–1101, 2017.

[59]   A. Chakraborty, A. Mondal, A. K. Halder, M. Dutta, and S. B. Singh, "Evolution of microstructure of zinc-nickel alloy coating during hot stamping of boron added steels," *J. Alloys Compd.*, vol. 794, pp. 672–682, 2019.

[60]   T. Kurz, G. Luckeneder, T. Manzenreiter, H. Schwinghammer, and A. Sommer, "Zinc Coated Press-Hardening Steel - Challenges and Solutions," in *SAE 2015 World Congress & Exhibition*, 2015, p. https://doi.org/10.4271/2015-01-0565.

[61]   M. C. Somani, L. P. Karjalainen, M. Eriksson, and M. Oldenburg, "Dimensional Changes and Microstructural Evolution in a B-bearing Steel in the Simulated Forming and," vol. 41, no. 4, pp. 361–367, 2001.

[62]   J. R. McDermid, private communication, 2021.

[63]   J. H. Kang, D. Kim, D. H. Kim, and S. J. Kim, "Fe-Zn reaction and its influence on microcracks during hot tensile deformation of galvanized 22MnB5 steel," *Surf. Coatings Technol.*, vol. 357, pp. 1069–1075, 2019.

[64]   C. M. Wichern, B. C. De Cooman, and C. J. Van Tyne, "Surface roughness of a hot-dipped galvanized sheet steel as a function of deformation mode," *J. Mater. Process. Technol.*, vol. 160, no. 3, pp. 278–288, 2005.

[65]   P. Drillet, "Coatings Dedicated to Press Hardened Steels for Automotive Applications," in *Galvatech*, 2017, pp. 401–408.

[66]   A. Ghiotti, S. Bruschi, F. Sgarabotto, and P. F. Bariani, "Tribological performances of Zn-based coating in direct hot stamping," *Tribol. Int.*, vol. 78, pp. 142–151, 2014.

[67]   H. Park, Y. J. Jeong, K. Lee, B. J. Goo, and H. J. Koh, "Effect of galvannealing temperature on coating microstructure evolution correlated to flaking degradation on galvannealed interstitial-free steel," *Surf. Coatings Technol.*, vol. 404, no. February, p. 126446, 2020.

[68]   N. L. Okamoto, D. Kashioka, M. Inomoto, H. Inui, H. Takebayashi, and S. Yamaguchi, "Compression deformability of Γ and ζ Fe-Zn intermetallics to mitigate detachment of brittle intermetallic coating of galvannealed steels," *Scr. Mater.*, vol. 69, no. 4, pp. 307–310, 2013.

[69]   M. H. Hong and H. Saka, "Plasticity and grain boundary structure of δ1k and δ1p intermetallic phases in the Fe-Zn system," *Acta Mater.*, vol. 45, no. 10, pp. 4225–4230, 1997.

[70]   A. Chakraborty, M. Dutta, and R. K. Ray, "Effect of Galvannealing Temperature on Texture and Powdering Behaviour of Galvannealed Coating on Different Grades of Steel," in *Galvatech*, 2011.

[71]   C. W. Lee, W. S. Choi, Y. R. Cho, and B. C. De Cooman, "Surface oxide formation during rapid heating of Zn-coated press hardening steel," *ISIJ Int.*, vol. 54, no. 10, pp. 2364–2368, 2014.

[72]   J. Faderl, S. Kolnberger, T. Kurz, G. Luckeneder, T. Manzenreiter, and M. Rosner, "phs-ultraform® – Continuous galvanizing meets press-hardening," in *Press-Hardening, 2nd International Conference on Hot Sheet Metal Forming of High Performance Steel*, 2009, pp. 283–292.

[73]   R. Autengruber, G. Luckeneder, and A. W. Hassel, "Corrosion of press-hardened galvanized steel," *Corros. Sci.*, vol. 63, pp. 12–19, 2012.

[74]   A. W. Hassel, "Fundamental Aspects of Corrosion of Press Hardened Galvanized Steel," in *Galvatech*, 2017.

[75]   E. A. Sacco, N. B. Alvarez, J. D. Culcasi, C. I. Elsner, and A. R. Di Sarli, "Effect of the plastic deformation on the electrochemical behavior of metal coated steel sheets," *Surf. Coatings Technol.*, vol. 168, pp. 115–122, 2003.

[76]   V. S. Raja, C. K. Panday, V. S. Saji, S. T. Vagge, and K. Narasimhan, "An electrochemical study on deformed galvanneal steel sheets," *Surf. Coatings Technol.*, vol. 201, no. 6, pp. 2296–2302, 2006.

[77]   H. H. Lee and D. Hiam, "Corrosion resistance of galvannealed steel," *Corrosion*, vol. 45, no. 10, pp. 852–856, 1989.

[78]   D. A. Jones, "Principles and prevention of corrosion." Prentice-Hall International, New Jersey, 1996.

[79]   S. T. Vagge, V. S. Raja, and R. Ganesh Narayanan, "Effect of deformation on the electrochemical behavior of hot-dip galvanized steel sheets," *Appl. Surf. Sci.*, vol. 253, pp. 8415–8421, 2007.

[80]   E. Kornienko, R. Ossenbrink, and V. Michailov, "Corrosion resistance of zinc-coated structured sheet metals," *Corros. Sci.*, vol. 69, pp. 270–280, 2013.

[81]   "Standard Test Method for Weight [Mass] of Coating on Iron and Steel Articles with Zinc or Zinc-Alloy Coatings." ASTM A90/A90M, 2018.

[82]   A. J. Bard, R. Parsons, and J. Jordan, "Standard Potentials in Aqueous Solution," *Stand. Potentials Aqueous Solut.*, 2017.

[83]   S. Fajardo, I. Llorente, J. A. Jiménez, J. M. Bastidas, and D. M. Bastidas, "Effect of Mn additions on the corrosion behaviour of TWIP Fe-Mn-Al-Si austenitic steel in chloride solution," *Corros. Sci.*, vol. 154, no. March, pp. 246–253, 2019.

[84]   H. E. Townsend, "Effects of Alloying Elements on the Corrosion of Steel in Industrial Atmospheres," *Corrosion*, vol. 57, no. 6, pp. 497–501, 2001.

[85]   P. Drillet, R. Grigorieva, G. Leuillier, and T. Vietoris, "Study of cracks propagation inside the steel on press hardened steel zinc based coatings," in *Galvatech*, 2011.